Numerical Study of Single-Chamber Solid Oxide Fuel Cells

Thesis by

Yong Hao

In Partial Fulfillment of the Requirements

for the Degree of

Doctor of Philosophy

California Institute of Technology

Pasadena, California

2007

(Defended May 2, 2007)

Acknowledgments

I’d like to express my gratitude to my advisor, Professor David G. Goodwin for his support, encouragement, understanding and seasoned guidance over the years I spent at Caltech for my research and study. This will be one of the most memorable experiences in my life and career.

I am very grateful to Professor Sossina M. Haile and Professor Zongping Shao for sharing their shining thoughts and being wonderful teachers and collaborators during the process of my Ph.D. research. Their diligent work and unique perspectives laid the solid experimental basis for the theoretical work in this thesis.

I’d also like to thank Dr. Carlos Pantano for his suggestions and encouragement. The theoretical work in this thesis benefited tremendously from the discussion with him.

I’m also indebted to my parents for their continuous support and love.

I have been enjoying working with my lab mates David Boyd, Francesco Ciucci, Moh El-Naggar, Jeff Hanna, Eugene Mahmoud, and Vaughan Thomas. It was a lot of fun working with them. Also, thanks are directed to Wei Lai, Calum Chisholm, Kenji Sasaki, Justin Ho, Jennifer Mederos, and Dane Boysen for their discussion. My friends James Endrizzi, Steve Rappel and David Silvey are also the people I’m very thankful to. Their sharing adds so much to my Caltech life and makes it a lot more colorful and enjoyable.

Lastly, I’d like to thank my committee members Professor David Goodwin, Sossina Haile, Melany Hunt and Paul Ronney for their comments and encouragement.

This work was supported by the Defense Advanced Research Projects Agency (DARPA) and the Office of Naval Research (ONR).

Abstract

Single-chamber solid oxide fuel cells (SCFC) are ones in which the fuel and oxidizer are premixed, and selective electrode catalysts are used to generate the oxygen partial pressure gradient that in a conventional dual-chamber design is produced by physical separation of the fuel and oxidizer streams. The SCFC concept is a novel simplification of a conventional solid oxide fuel cell (SOFC), and SCFCs have been shown capable of generating power densities high enough to make them potentially useful in many applications where the simplicity of a single gas chamber and absence of seals offsets the expected lower efficiency of SCFCs compared to dual-chamber SOFCs.

SCFC performance is found to depend sensitively on cell microstructure, geometry, and flow conditions, and optimization of SCFC stacks requires considering complex, coupled chemical and transport processes. However, research activity in this area is far from sufficient and insights about SCFC systems are very limited. The understanding of many fundamental physical and chemical processes required for improving SCFC designs is often beyond the capability of modern experimental techniques, and efficient experimental studies are often held back by the lack of guidance from theoretical models due to the fact that modeling study about SCFC is very rare to date, and existing models about conventional SOFCs are not suitable for simulating SCFCs because of the inherent differences of single-chamber SOFCs from conventional ones. In order to systematically investigate these problems and optimize the electrical performance of SCFC systems, a 2D numerical model of a single-chamber solid oxide fuel cell (SCFC) operating on hydrocarbon fuels is developed and presented in this work.

The model accounts for the coupled effects of gas channel fluid flow, heat transfer, porous media transport, catalytic reforming/shifting chemistry, electrochemistry, and mixed ionic-electronic conductivity. It solves for the velocity, temperature, and species distributions in the gas, profiles of gaseous species and coverages of surface species within the porous electrodes, and the current density profile in an SCFC stack for a specified electrical bias. The model is general, and can be used to simulate any electrode processes for which kinetics are known or may be estimated. A detailed elementary mechanism is used to describe the reactions over the anode catalyst surface. Different design alternatives including flow rates, flow geometry, temperature, optimal fuel to air ratio, anode thickness, YSZ vs. SDC electrolytes, and fuel cell efficiency and fuel utilization are explored. The reaction zones in the anode of an SOFC with hydrocarbon fuel and oxygen addition is also investigated and much deeper insights are obtained compared to the existing literature. Numerical techniques needed for such investigations are also introduced.

The model is also expanded to simulate fuel cells in the commonly seen dual chamber configuration, including ones with either oxygen-ion conducting electrolytes (SOFCs) or proton conducting electrolytes (solid acid fuel cells). Good agreement with literature results and experimental measurements is obtained.

Contents

List of Figures

List of Tables

Nomenclature

Latin Letters

A_{e}	Specific surface area of a porous medium
c_p	Specific heat at constant pressure
d_p	Particle diameter
$D_{k,m}$	Mass diffusion coefficient of gas species k in a gas mixture
D_k^T	Thermal diffusion coefficient of gas species k
E_0	Nernst potential
E	Load potential
F	Faraday's constant
h_k	Enthalpy of species k
i_{i}	Ionic current
i_{e}	Electronic current
i_{tot}	Total current
j	Current density
j_0	Exchange current density
$\underline{j_k}$	Mass flux of gas species k
L_{e}	Electrolyte thickness
$\dot{m}$	Mass flow rate
N_{sp}	Total number of gas phase species
N_{surf}	Total number of surface phase species
p	Pressure
Pr	Prandtl number
q''	Heat flux

R , R_g	Universal gas constant
Re	Reynolds number
Sc	Schmidt number
$\dot{s}_k$	Molar production rate of species k over the catalyst surface
T	Temperature
$\underline{u}$	Velocity vector
u	x-component of the velocity field
v	y-component of the velocity field
W	Molecular weight
$\overline{W}$	Mean molecular weight
X_k	Molar fraction of species k in a gas mixture
Y_k	Mass fraction of species k in a gas mixture

Greek Letters

α_{a}	Anodic asymmetry factor of the Butler-Volmer equation
α_{c}	Cathodic asymmetry factor of the Butler-Volmer equation
ε	Emissivity
ε_U	Fuel utilization
ϕ	Porosity of a porous medium or a general scalar
η	Overpotential or fuel cell efficiency
λ	Thermal conductivity
μ	Dynamic viscosity
θ	Dimensionless temperature or coverage percentage of surface species
ρ	Density of gas or solid

σ_e	Electronic conductivity
σ_i	Ionic conductivity
τ	Tortuosity of a porous medium
$\dot{\omega}_k$	Molar production rate of species k

Operators

∇	Nabla operator
Δ	Difference operator

Acronyms

ASR	Area-specific resistance
BET	Brunauer-Emmett-Teller (method)
BSCF	$Ba_{0.5}Sr_{0.5}Co_{0.8}Fe_{0.2}O_{3-\delta}$
CFL	Courant-Friedrichs-Lewy (condition)
LSGM	$La_{0.9}Sr_{0.1}Ga_{0.8}Mg_{0.2}O_3$
MEA	Membrane electrode assembly
OCV	Open circuit voltage
SDC	$Ce_{0.8}Sm_{0.2}O_{1.9}$
SSA	Specific surface area
YSZ	Yttria-doped Ceria

Chapter 1
Introduction

1.1 Overview of Solid Oxide Fuel Cells

Fuel cells are a type of highly efficient energy conversion device that directly produces electricity from external supplies of fuel and oxidant. They produce power without combustion or rotating machinery, and work continuously as long as the fuel supply is maintained. Fuel cells offer the prospect of silent electrical power generation at high efficiency with near-zero emission of pollutants. Fuel cells are not subject to the Carnot limitation and their theoretical maximum efficiency based on the chemical exergy of the fuel is close to 100%. The efficiencies of currently operating systems are in the range of 40–60% but they have the potential to achieve higher values, particularly with hybrid configurations where a high-temperature fuel cell replaces the

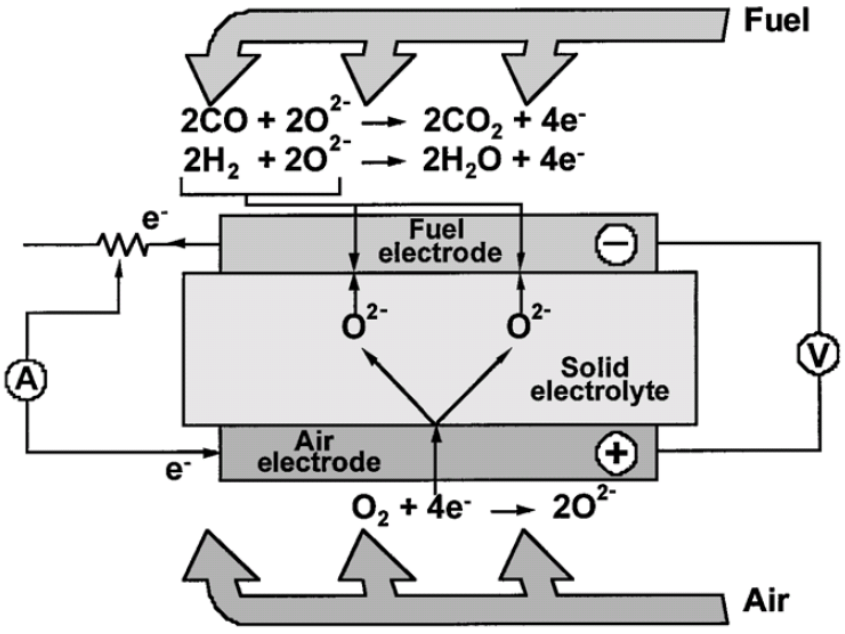

Figure 1-1. Illustration of a working solid oxide fuel cell [2]

combustor of a gas turbine [1].

Fuel cells are often classified by electrolyte. Among them, solid oxide fuel cells (SOFC) utilize ceramic materials that conduct oxygen ions (e.g., yittria-stabilized zirconia, YSZ) as the electrolyte layer and usually operate at high temperature (600-1000^{o}C) for the electrolyte to have sufficient ionic conductivity. Fig. 1-1 shows the working principle of an SOFC, in which oxygen is reduced on the cathode side and hydrogen and carbon monoxide are oxidized on the anode side simultaneously by electrochemistry.

Compared with other types of fuel cells, solid oxide fuel cells have many advantages. The high temperature increases the potential for high system efficiency. Conversion efficiencies of SOFC can be considerably greater than those of heat engines, with hybrid cycles in combination with heat engines and co-generation promising conversion efficiencies greater than 70% [3]. Solid oxide fuel cells can operate on hydrocarbon or hydrocarbon-derived fuels directly [3] and have the widest range of fuels. Furthermore, because SOFCs operate at such high temperatures, direct internal reforming of hydrocarbon fuels becomes particularly attractive, because the heat released by the electrochemical reaction is partially used to supply the endothermic reforming process. Therefore, the fuel processing can be integrated with the fuel cell stack, and catalyst particles in the anodes reform the fuel into H_2 and CO for direct electrochemical conversion [1]. Meanwhile, SOFCs are tolerant to gas contaminants normally considered “poisons” (e.g., CO) for lower temperature fuel cells. Studies show that CO can be utilized directly [4] or indirectly by

electrochemistry in SOFCs. The indirect route is by way of the water-gas shift reaction to convert CO to H_2, and it generally exceeds the direct utilization of CO by electrochemistry [1]. The tolerance to CO eliminates the need for noble metal for electrodes (e.g., Pt) and lowers fabrication cost.

On the other hand, the high operating temperature also leads to drawbacks such as long startup time, small number of thermal cycling (i.e., heating up and cooling down) and stringent requirement on both materials and manufacturing processes. In addition, the mechanical shock resistance is low, particularly for the conventional dual-chamber configuration. Moreover, the application of SOFCs for propulsion (for transportation purposes) and portable power generation are still very limited. All these drawbacks require additional research.

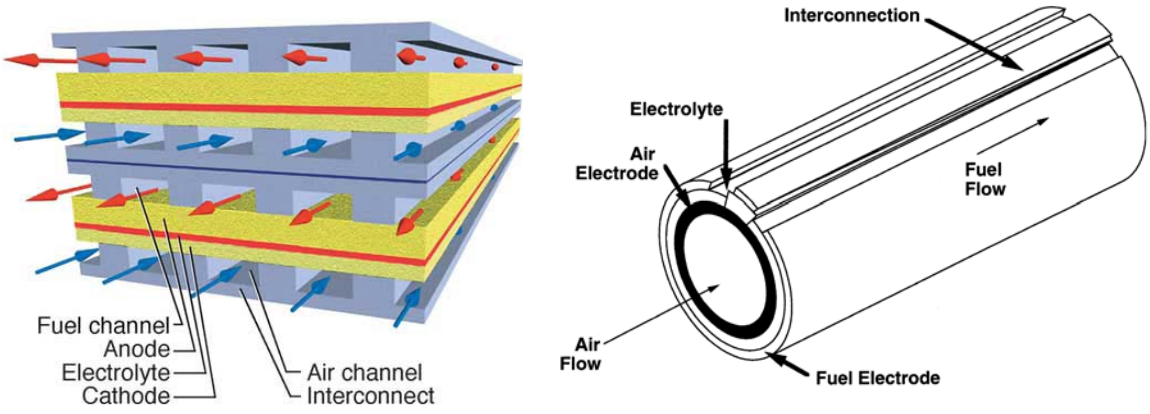

Figure 1-2. Solid oxide fuel cell configuration (a) Planar design with fuel and air in counterflow [3]; (b) Siemens-Westinghouse tubular design [5]

Based on design geometries, solid oxide fuel cells are categorized as planar and tubular. Fig. 1-2a shows a typical planar SOFC design with fuel and air in counter-flow. Co-flow and cross-flow designs are also possible in order to supply the fuel and oxidant in the most efficient manner, and also to minimize temperature gradients

within the stack [1]. The major problem with planar SOFCs (both single cell and stacks) is the cracking of the sealing material due to thermal cycling.

The tubular design (Fig. 1-2b) was first developed by the Westinghouse company and does not have the sealing problem. One end of the fuel cell is closed, providing an integral return for the air introduced from the other end through a concentric tube. The tubular design is the most advanced and applies in large commercial and industrial cogeneration areas. The technical challenge with tubular SOFC stacks mainly lies in the flow management.

1.2 Overview of Single-Chamber Solid Oxide Fuel Cells (SCFC)

Most of the SCFCs being studied belong to the planar SOFC category. It is a novel type of SOFC in which the anode and cathode are both exposed to the same premixed fuel/air stream, and selective electro-catalysts are used to preferentially oxidize the fuel at the anode and reduce oxygen at the cathode [6]. It operates in a mixture of hydrocarbon fuel and oxygen in which the amount of oxygen is less than that required for complete combustion of the fuel. This is called the fuel-rich condition and is required to produce hydrogen and CO (i.e., syngas) without producing significant amounts of CO_2 and H_2O. At the anode, selective catalysts result in *in-situ* catalytic reactions (e.g., partial oxidation and reforming) of the fuel to produce the syngas, which are then electrochemically oxidized by reaction with oxygen ions at the anode-electrolyte interface. At the cathode, gaseous oxygen is

reduced to replenish the oxygen ions in the electrolyte lost on the anode side, with a net flow of current through the electrolyte and in the external circuit.

In an SCFC, the chemical (or electrical) potential gradient across the cell, i.e., the driving force for the electrical current, is generated by the oxygen partial pressure gradient due to the selectivity of the electrode catalysts for different catalytic reactions, rather than by physically separating the fuel and oxygen as in the conventional dual-chamber design. As a consequence, the need to maintain gas-tight anode and cathode chambers is eliminated and the fuel cell design is greatly simplified. In fact, the SCFC not only gets rid of the sealing, but even allows for a porous electrolyte [7]. Recent studies showed that SCFC with porous electrolytes could also deliver high performances [8]. This allows relatively low processing temperature of the electrolyte and thus reduces the manufacturing cost [9].

The need for selective electro-catalysts has several implications for the design of an SCFC. First of all, an SCFC must operate at a temperature low enough that the catalysts maintain some degree of selectivity; this typically limits the temperature to below 700^{o}C, which is significantly lower than that of conventional SOFCs with a YSZ electrolyte. For this reason, SCFCs demonstrated to date have used ceria-based electrolytes, rather than YSZ [6]. The relatively low temperatures (400-600°C) at which the most advanced SCFCs function also help to ease complications with on-off cycling. The reduced temperatures of operation provide additional benefits including expanding the choices of materials for fabrication of peripheral components and inhibiting carbon deposition via hydrocarbon cracking at the anode catalyst [10].

Meanwhile, the low temperature also reduces the possibility of explosion of the fuel-air mixture. For example, the ignition temperature of methane is higher than 1000^{o}C, especially over Ni and Pt surfaces [11], and therefore SCFCs with methane fuel can avoid this problem when operated in the reduced temperature range.

Another implication of the need for selective electro-catalysts is that an SCFC is unlikely to run well, if at all, on hydrogen. Any catalyst that promotes electrochemical oxidation of hydrogen, or electrochemical reduction of oxygen, would very likely promote direct catalytic combustion if exposed to a hydrogen/air mixture. This problem can be dealt with by using a hydrocarbon fuel instead of hydrogen, as has been done in all successful demonstrations of SCFC operation. With a hydrocarbon fuel, catalytic partial oxidation and reforming chemistry can be used within the anode to deplete incoming oxygen, creating a reducing environment deep within the anode near the electrochemically active layer, and to generate hydrogen needed for the electrochemistry *in situ*, very near where it is consumed in the electrochemical oxidation reaction. Similarly, at the cathode, if hydrogen generation via hydrocarbon cracking can be suppressed, parasitic combustion at the cathode may be minimized [6].

1.3 Literature Review

Before starting the discussion about the modeling work on SCFC, it is important to review the research status in both experiment and modeling in this area. The objective of this section is to review the technical background of this thesis, including

both the advances in SCFC studies (mostly experimental) and the existing modeling research on SOFC systems in general. Existing challenges are listed at the end of this section.

1.3.1 Research Status in the Single Chamber SOFC Area

The SCFC was conceptually proposed by researchers in 1965 [12], and the first application of this concept to SOFCs was made by Hibino et al. in 1993 [13]. So far, research in this area has been mostly experimental, with most advances in the fuel cell performance resulting from improvement with the materials of both electrodes and the electrolyte, especially in early studies.

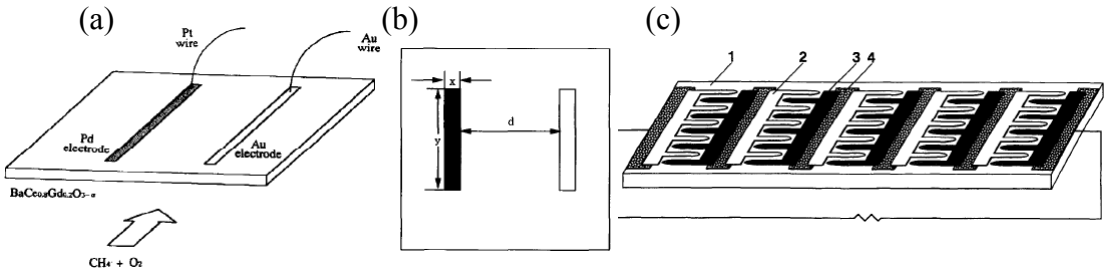

Figure 1-3. Hibino's strip configuration SCFC [14]. (a)&(b) unit cell, (c) stack; 1=solid electrolyte, 2=gold electrode, 3=palladium electrode, 4=gold film as an interconnector

Hibino first proposed the strip configuration (later called the B-type, Fig. 1-3) fuel cell operated in a mixture of methane and air. In this configuration, the two electrodes (gold cathode and palladium anode in this case) are fabricated on the same face of the ceramic electrolyte ($BaCe_{0.8}Gd_{0.2}O_{3-\sigma}$ in this case), and the distance (Fig. 1-2b) between them varies. The discharge characteristics generally improve as the distance decreases [14]. For this reason, Hibino et al. proposed that the most suitable design

for this type of SCFC is an inter-digitated comb-shape array in which the two electrodes face each other in close proximity [14].

Despite the advantage of being compact, the design of this type of SCFC also puts some inherent limitations on its performance. First of all, although the distance between the two electrodes plays an important role in the overall ohmic resistance between them, the resistance also goes up with the width of the electrodes [14], limiting the width itself and thus the total catalyst surface area for both the production of syngas (i.e., H_2 and CO) and reduction of oxygen. Secondly, the electrical performance is hindered by the gas-phase diffusion of syngas from the anode to the cathode and the combustion of the syngas over the cathode catalyst surface. This not only requires a careful control of the flow direction, but also requires the two electrodes not be too close to each other, keeping the ohmic resistance from further reduction. Lastly, the electrodes are sputtered onto the electrolyte plate so as to maximize the electrode area and to minimize the conduction path of the charge carrier [15], thus limiting their thickness and thus the production of the syngas. More importantly, the thickness is unlikely to be increased significantly due to considerations in both fabrication and the gas-diffusion of syngas given the closeness of the electrodes.

For reasons stated above, the majority of recent studies about SCFC focus on the stacked configuration (also called type-A SCFC by Hibino et al.) instead (Fig. 1-4), in which the electrodes are on different sides of the electrolyte. Although the cell could be mechanically supported by either the electrolyte or one of the electrodes, the

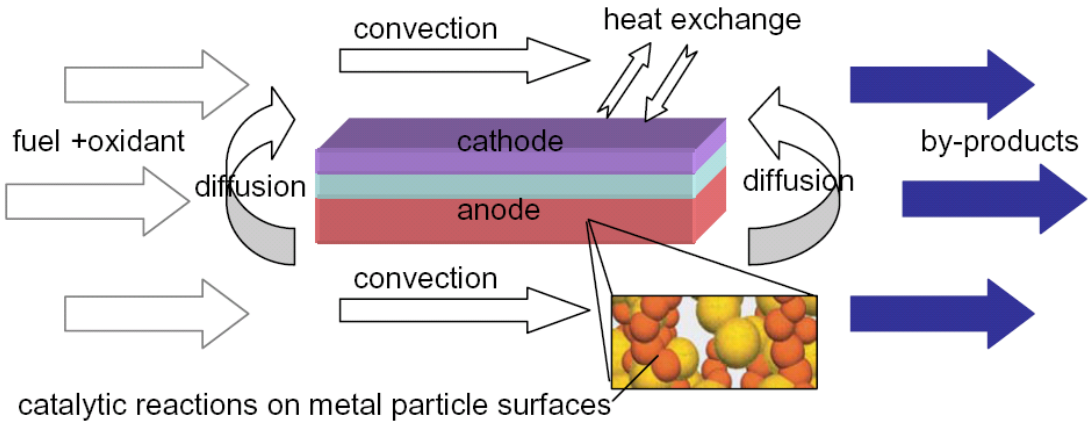

Figure 1-4. The operation of a stacked SCFC [6]

anode-supported cell is of particular interest due to its high performance. The latest design of such cells typically involves a thick nickel-based anode (of the order 1 mm), a ceria-based electrolyte with high ionic conductivity, and a perovskite cathode (e.g., $Sm_{0.5}Sr_{0.5}CoO_3$, SSC) with high oxygen-reduction capability. The thick anode not only provides enough surface sites for the reforming and partial oxidation of the hydrocarbon fuel for the production of syngas for electrochemistry, but also brings the additional advantage of a significant temperature increase due to the catalytic oxidation of the fuel (discussed later in the thesis). In addition, the separation of the electrodes benefits the performance in two ways. First, it makes it more difficult for the syngas to diffuse from the anode to the cathode, thus reducing the parasitic combustion at the cathode. Second, the ohmic resistance of the electrolyte can be significantly reduced by using very thin layers, which is only limited by its own mechanical properties. For these reasons, the anode-supported SCFC in the stacked configuration delivers much higher power density compared with the cells in the strip configuration. Peak power densities of ~ 650, ~ 400 and ~ 440 mW/cm^2 have been reported in the literature using methane, ethane, and propane fuels, respectively [10].

The stacked configuration of SCFC has some characteristics that make it particularly suitable for micro-scale power generation. The Integrated Micro-Power Generator Project is one example. The readers are referred to Appendix A for more details. The anode-supported SCFC in stacked configuration is the topic of this thesis.

It needs to be pointed out that the efficiency of the SCFC is typically much lower than the dual-chamber SOFCs (see Chapter 3). However, the goal of the SCFC study is to compete with lithium batteries in terms of total power output, and the low efficiency can be compensated by the high energy density of hydrocarbon fuels mentioned in Appendix A.

The development of SCFC generally proceeds with innovations in materials for cell components with gradually-expanding scope of other parameters, leading to a general trend of lower temperature, higher power density, and more comprehensive consideration in design. Before 2002, major advances were made by Hibino's group with the stacked configuration, focusing on the materials side. Their investigations were usually performed with fixed operating conditions including temperature, gas flow rates, and flow field geometry. Hibino's earliest SCFCs used Pt as the anode and Au as the cathode [16]. The performance was poor partly because Pt is a well-known combustion catalyst for methane and thus the selectivity for generating hydrogen is low, partly because the electrolyte resistance is high, and partly because both electrodes are relatively dense. The first significant improvement was made by adding MnO_2 to both electrodes and the electrolyte, which lead to remarkable increase in electrode porosity and the contact area between the electrodes and the electrolyte,

reducing electrode reaction resistances. The next breakthrough came with the adoption of Ni anode and $La_{0.8}Sr_{0.2}MnO_3$ (LSM) cathode [12], which are much better than the Pt-Au electrode pair. Both open circuit voltage (OCV) and maximum power were greatly improved.

This was succeeded by a dramatic reduction of operating temperature from 950^{o}C to 500^{o}C, achieved through the employment of electrolyte materials with high ionic conductivity and reduction of electrolyte thickness [17]. Samaria-doped ceria (SDC), a mixed ionic-electronic conducting material, was used instead of YSZ, and the minimum thickness was reduced from 0.5 mm to 0.15 mm, significantly reducing the total ohmic resistance. The ceria electrolyte also resulted in a much smaller electrode reaction resistance, explained by the promotion of the rate of the rate-limiting charge transfer reaction at the triple-phase (gas-electrode-electrolyte) boundary through the increase of ionic conductivity. In this study, the ethane fuel also contributed to the lower temperature since it is less stable than methane used in previous studies. The reported maximum power density of 403 mW/cm^2 (at 500^{o}C) was much higher than the 121 mW/cm^2 (at 950^{o}C) previously reported with YSZ electrolyte.

The fuel cell performance was further improved in terms of lower temperature and higher power density by doping Pd in the Ni-SDC anode, with the same thinking of SDC electrolyte and higher hydrocarbon fuel inherited. With the Pd-doped Ni anode and $Sm_{0.5}Sr_{0.5}O_3$ (SSC), the SCFC could operate at temperatures as low as 450^{o}C, and the maximum power reported at 550^{o}C was 644mW/cm^2 [18]. On the other hand, the lowest operating temperature of 300^{o}C with butane fuel [19] was also reported.

Since 2004, many researchers have started to expand the parameter set for study, along with the materials. Shao et al. studied SCFC from perspectives including material, temperature, flow geometry, fuel type, and fuel/air ratio. They first reported $Ba_{0.5}Sr_{0.5}Co_{0.8}Fe_{0.2}O_{3-\delta}$ (BSCF) as a new cathode material for both single- and dual-chamber SOFCs at reduced temperatures, and the BSCF cathode with a 30wt% SDC was in the best favor for SCFC at reduced temperatures due to its inactivity towards the oxidation of hydrocarbon fuels and the extraordinary oxygen vacancy diffusion rate compared with previous cathode materials [9, 20]. They also reported operating a two-cell stack without external heating in a propane-oxygen-helium mixture. The anode-facing-anode geometry that they proposed resulted in a combined power density more than twice as much as that of a single cell, and the total power output was 0.35 W at the cell temperature of 580^{o}C. They also demonstrated that fuel cell power improves with flow rates. The fuel cell was tested in the temperature range of 400 to 700^{o}C, with the ideal oxygen/propane ratio measured to be about 2.5 to 3.0 [9, 21]. They recently reported the power density of an SCFC running with methane to be as high as 786 mW/cm^2 [22], which is the highest in literature so far.

Other important results were reported by Stefan et al. about flow geometry [23], Suzuki et al. about both materials [8, 24–26] and flow rate [8], and Napporn et al. about flow rate [27] and actual fuel cell temperature [28]. Specifically, Stefan et al. reported that the fuel cell geometry that exposes the cathode to the incoming gas feed delivers a better performance than the case when the cell is flipped by 180 degrees. This effect will be discussed later in the thesis.

1.3.2 Solid Oxide Fuel Cell Modeling

Another important background of this work is the numerical modeling of SOFCs. For the convenience of discussion, the model classification will be discussed first. Depending on the type of questions they address and the type of assumptions they make, the existing models in literature can be classified according to different criteria. Based on the number of dimensions that they simulate, the models can be classified as one-, two-, and three-dimensional [29–33]; based on the necessity to resolve temporal evolution, they can be classified as transient [33, 34] and steady-state models [35, 36]; based on length scale, they can be classified as system-level [33], cell-level [37–39], and component-level models [32, 40, 41]; based on geometry, they can be categorized as planar [33, 42] and tubular [35, 43].

The discussion in this section will be based on the length-scale categorization since it best described the work presented in this thesis. However, a review about different ways to classify the models will be informative and could provide useful insights. So other classification methods will also be discussed here based on their application on different length scales.

First of all, the geometric classification is mostly useful on the system level, describing the macroscopic flow and heat transfer management and their influence on the fuel cell performance, and thus it largely falls in the category of system-level modeling. Since the general forms of underlying governing equations for flow and heat transfer are the same, the difference in geometries is not important to this work,

and the geometric classification can be combined into the discussion on system-level modeling.

Secondly, as for the temporal classification, the majority of the existing models are steady state, especially (but not only) those for system-level fuel cell performances including voltage and power. The transient models are mostly impedance spectrum models (e.g., [34]) on the MEA (membrane-electrode assembly) level and the component level, plus a very few system-level models with the need to simulate time-response of the system [33]. Although the steady-state models can be formulated in a transient form, in most cases the time evolution is not of interest, and the computation with time being a true variable can lead to various numerical issues (e.g., stiffness of partial differential equations) and reduce the computation efficiency. So for the work in this thesis, the temporal classification is not truly necessary, and the steady-state models are of interest. They can be combined with the discussion about models at different length scales.

Lastly, the number of dimensions that a model takes really depends on the focus and the requirement to resolve the questions under consideration, and is not necessarily connected with the length scale that the model is designed for. Although many system-level models are 2D or 3D, a lot of useful insights (e.g., fuel cell efficiency) can still be obtained by 1D system models [29] when the multi-dimensional effects are not important; on the other hand, although many MEA models are formulated in a 1D form [37], the number of dimensions do need to be increased even at micron meter scale when there are needs to resolve the multi-dimensional

structures and effects [32, 44]. Furthermore, a multi-scale model can employ different number of dimensions at different length scales based on the needs mentioned above and on the consideration of computation efficiency. For example, it's not an unusual practice to assume 1D electrochemistry in many 3D system-level models [35]. Bove et al. [45] give a brief review on SOFC modeling approaches with different dimensions.

Phenomena in fuel cells relate to many disciplines from materials science through electrochemistry, catalytic chemistry, and heat and mass transfer, to fluid mechanics [1]. A fuel cell model should, depending on needs, involve one or more of these areas in a coupled way. On the system level, many models have modules to simulate the fluid flow and/or heat and mass transfer because the distribution of gas reactants, temperature, and flow geometry can often significantly affect the fuel cell performance. For example, the 3D model by Achenbach [33] showed the importance of heat transfer in an SOFC stack; comparatively small temperature variations can have significant effects on the reaction kinetics, ionic conductivity, and Nernst potential [1]. In the simulation of the multi-component flow, the governing equations for the conservation of mass, momentum, and energy gas are usually solved together [33, 46] by some implicit numerical scheme. This is called "thermofluid modeling" by some researchers [1]. Some groups make simplifications by simulating the system at presumed (e.g., uniform) flow field [47, 48] or at uniform temperatures, while most of the recent large-scale flow calculations fully resolve the flow with commercial CFD software such as FLUENT [35, 49, 50], FEMLAB [51], or STAR-CD [42, 52] that

allows the user to incorporate his own model via "user-defined functions" [1]. Ma et al. [53] give a review of the use of CFD in fuel cell applications.

Despite the different approaches for thermofluid modeling on the system level, a few points need to be stressed. First, modeling of flow and heat transfer is eased by the fact that flow in SOFCs is usually laminar [1]. Second, gas-phase chemistry is typically neglected since most SOFCs run on hydrogen (for dual-chamber only) or methane (both single- and dual-chamber), and for the hydrogen case it doesn't exist because in dual-chamber SOFCs, hydrogen and oxygen are physically separated, while for the methane case the operating temperature of SOFCs (below 1000^{o}C) is typically too low for the gas-phase reaction of methane to be significant [1, 54]. However, for SOFCs running on higher hydrocarbons (e.g., propane), gas-phase chemistry may be important and needs to be simulated by some readily-developed reaction mechanisms. Third, many models assume constant gas properties such as density and diffusion coefficient, which is an oversimplification since the variation of component and temperature can be very large, and accurate representation of the properties of high-temperature gas mixture is not straightforward [1]. Fourth, if the effect of temperature variation is ever going to be considered in a model, radiation heat transfer should not be neglected, since at the operating temperature of most SOFCs, radiation accounts for a significant portion of the heat transferred and thus sensitively influences the temperature.

Models at the MEA level typically involve modules describing the diffusion and reaction in the porous electrodes, with electrochemistry usually being treated as a

boundary condition. Although it is well known that the electrochemically active region extends at least 10 μm into the porous electrode [55], and there are existing models at the component level about the detailed structure and processes about the electrodes [44] and the electrode-electrolyte interface [32], the approximate treatment of the electrochemistry often leads to satisfactory prediction of overall performance. Most models represent the electrochemistry by the Butler-Volmer equation, although some study shows that for charge-transfer processes that include more than one step, the values of the asymmetry factors can be greater than 1 [56]. The objective of the diffusion model is to supply the anode with hydrogen and cathode with oxygen, and to remove the reaction product water, while minimizing the concentration difference across the porous electrodes [1]. Accurate ways to simulate the multi-component diffusion process include the dusty gas model (DGM) [37, 57] and the mean pore transport model (MPTM) [58]. Young [1] gives a detailed comparison between these two approaches. The work in this thesis uses the dusty gas model. As for the reaction modeling with hydrocarbon fuels, especially methane, many papers [47, 52] use a global description of the reforming and water-gas shift reactions with constant-rate constants, and some even use pre-reformed fuel [59]. Needless to say, such treatment of the reaction is very rough and does not provide a sound basis for quantitative prediction. Recently, Deutschmann et al. developed a multi-step, elementary reaction mechanism to describe steam-assisted catalytic partial oxidation of methane in small-channel monolith reactors using Ni supported on alumina [60]. The reliability of the mechanism has been validated by the work of Hecht et al. for dual-chamber SOFC

[61] and used in several models demonstrating with good quantitative agreement with experiments [50, 56]. The work in this thesis employs the same reaction mechanism to study the heterogeneous reactions in the porous Ni anode of an SOFC.

Lastly it's worth pointing out that all SOFC models have to be validated by careful experimentation. Otherwise, a prediction is only as good as the underlying physical modeling [1].

1.3.3 Modeling of Single Chamber SOFC

The modeling of single-chamber SOFC is similar to the modeling of dual-chamber SOFCs in many ways. However, there are still a few major differences based on the review of SCFC above. First of all, the flow model needs to be at least two-dimensional, since experimental research has shown the importance of flow management by way of geometric design. Secondly, the anode reaction is more complicated than the dual-chamber case, due to the mixing of fuel and oxygen. This requires that a detailed reaction mechanism be used. Thirdly, due to the mixing of fuel and air as well as the gas-phase diffusion from anode to cathode, an experimental oxidation reaction mechanism of the hydrocarbon fuel and the syngas (i.e., hydrogen and CO) is needed on the cathode side. Lastly, since the temperature increase of the fuel cell is much more significant than dual-chamber SOFCs, radiation must be an integral part of the model.

Besides the work presented in this thesis and published papers [6, 10], the only other single-chamber SOFC model reported in literature was developed by Chung et

al. [51, 62] in parallel with the experimental research by Ahn et al. [63, 64] about the strip configuration, which is different from the focus of this work. That model is able to calculate the polarization curves of the fuel cell and make some qualitative conclusions for improvement of the experimental design. The strength of Chung's work is that it resolves the three-dimensional flow field around the fuel cell with the commercial finite element package FEMLAB. The simulation of the 3D flow field is necessary for the understanding the flow and mass transport problems in such a fuel cell system.

However, Chung's model is still far from enough to make any prediction of the fuel cell on a reliable basis due to the limitation imposed by the capability of the CFD software, oversimplifications in the model development, and lack of experimental validation. Compared with other CFD packages particularly designed for fluid dynamics and heat transfer, the FEMLAB software is quite primitive. Constant gas properties including density, viscosity, and diffusivity have to be assumed. Another significant drawback with the model is that it lacks the critical capability to simulate the diffusion and reaction of methane in the porous anode. This results in a mixture of hydrogen and air, which is never possible for SCFCs. Besides, although the model claims to have the capability to simulate "ceria"-based SCFCs [51], it does not actually involve the simulation of mixed electronic-ionic conduction.

Based on the literature review above, it can be seen that although the current status of SOFC modeling provides enough capability to model most aspects of SCFCs, there is very little modeling work in this area, possibly due to the differences between

SCFC and the dual-chamber SOFCs. Currently the experimental research in the SCFC area needs much more guidance from modeling, which is the motivation of this work and will be discussed below.

1.4 Scope of This Thesis

The motivation section describes the current challenges in the stacked SCFC development and objectives for this work, followed by a section showing the accomplishments that the model has achieved so far.

1.4.1 Motivation

SCFC development has proceeded primarily via experimental optimization of the multiple parameters relevant to the power output, and important ones such as the selectivity of the electrodes, have received considerable attention in research. However, although very respectable power densities have been demonstrated experimentally, it is not at all clear that present designs are close to optimal, or that the measured performance for a single cell translates to performance in a stack.

Besides the selectivity of the electro-catalysts, there are many other factors that influence SCFC performance for both unit cells and cell stacks. For example, at the atomistic level, the performance of a unit cell is dictated by the interplay of a variety of physical or chemical processes, including surface chemistry on the anode and cathode, heat transfer, transport of the gaseous reactants and products within the porous electrodes, and transport of mobile ions through the solid electrolyte. At the

mesoscale, the cell performance is found to sensitively depend on the system fluid mechanics (e.g., cell orientation relative to the flow), species transport, and competition between various modes of heat transfer. On the cell-stack level, hydrogen generated within one anode might diffuse to the cathode of an adjacent cell where it burns, or, if some cells are placed downstream of others, depletion of fuel or oxygen may strongly affect performance. Assessing the potential performance of a SCFC stack design requires considering all these complex effects for both unit cells and the stack.

Despite the obvious importance of these design issues, current experimental research is limited by the lack of effective research tools, particularly diagnostic tools for micro-scale physical and chemical processes, which are crucial for the cell functionalities. Most experimental groups have to take the relatively inefficient trial-and-error loop to improve their cell design, which makes the systematic study and optimization of design parameters tedious and cost-prohibitive.

The design needs of SCFC thus require a comprehensive numerical model that can simulate all the important processes in the fuel cell and can provide fundamental insights into the design tradeoffs. Due to the reasons stated above, the model should not only be able to treat each individual process, but should also handle the coupling among the important ones, including channel flow transport, catalytic surface chemistry, electrochemistry, heat transfer, ionic conduction, and porous media transport within the electrodes of each cell. The simulation of the single-chamber configuration is more complex than encountered when simulating dual channel

configurations, where the flow in the gas channels may be treated as a plug flow. In the absence of defined gas channels, the flow and transport processes must be treated using a multidimensional formulation and a model of at least two-dimension is needed.

This work presents a two-dimensional numerical model about the anode-supported SCFC in the stack configuration. Besides a large design parameter space and the popularity of this type of cell in experimental research, the relatively simple representation of the cell and external flow compared with the strip configuration is also an important motivation of this work. In the stacked configuration, due to the high aspect ratio of the cell, the transport processes in the electrodes and the electrolyte can be well modeled locally as one-dimensional; the relatively weak lateral diffusion compared with the dominant channel flow means that the flow around the cell can be well simulated with a two-dimensional model. Therefore, a model of 2D is considered sufficient for describing this type of SCFC. Also, due to considerations of computation cost and efficiency, a lower-dimensional model is preferred as long as the fundamental principles can be captured.

In addition, many other fuel cell designs, such as the tubular SOFC and the planar, dual-chamber SOFC in the button-cell configuration can be sufficiently described by a 2D model. These add to the motivation for this work to develop the model into a general framework that can simulate such fuel cell systems.

The major purpose of this work is to answer important design questions for SCFC systems such as optimization of design parameters especially in the realm that experimental research is unable to explore, through systematic simulation of SCFC

performances for both unit cell and cell stacks. Through the combined effort of experiment and simulation, the design process of SCFC systems can be greatly accelerated and the development cycle can be significantly reduced. In addition, important issues for the design of planar dual-chamber SOFC and tubular SOFC are also discussed.

1.4.2 Accomplishments

This work is the first numerical model of the stacked SCFC systems based on first principles and calibrated on a physical basis. Deep insights in catalytic chemistry, electrochemistry, flow convection, heat transfer, and mixed conducting are obtained. The simulated electrical performance shows good agreement with experimental results.

The model has been applied to optimization design of both single SCFC and SCFC stacks, and reasonable results have been obtained. It is very difficult to accurately explore these optimization issues experimentally, but the model prediction provides reliable theoretical basis for further improvement in experiment without the trial-and-error design cycles.

The model is able to simulate the planar SOFC in the single- and dual-chamber configurations, and can also be adapted to simulate the tubular SOFC after minor changes. It allows a great flexibility in defining the two-dimensional flow geometry for the planar SOFCs.

The model can simulate the SCFC performance with a much wider range of design parameters than allowed in actual experiment. This leaves enough room for design optimization of the SCFC system.

Although methane is the major fuel under investigation in this work, the model can actually simulate SCFC running on any hydrocarbon fuel provided that the partial/full oxidation mechanism in the electrodes is available.

1.5 Organization of This Thesis

In Chapter 2, the numerical model is discussed in detail, including the governing equations, boundary conditions, and the numerical schemes to solve the problems in both the flow channel and the MEA.

In Chapter 3, the calibration of the model based on experimental measurements is presented; followed by the prediction of the model for SCFC performances compared with experimental results; and the exploration of many important design parameters such as the optimum fuel-to-oxygen ratio in the SCFC design.

In Chapter 4, the application of the model to planar dual-chamber fuel cells with either oxygen ion conductor or proton conductor electrolyte is discussed.

Chapter 5 discusses some advanced topics, such as the three-layer structure of reaction zones in an SOFC anode and the design of a multi-layer anode for SOFC with oxygen addition in general. The automatic refinement of a computational grid for the fuel cell is also discussed.

Chapter 6 makes conclusions and discusses future work for the study.

1.6 Format Convention

Texts in each chapter are usually divided into subheadings of different levels. The first-level subheadings have the format of “1.1” and the second level is formatted “1.1.1.” Third and fourth level subheadings are also used in some chapters, with the third level using italic fonts and the fourth level using underlined italic fonts.

As for the bibliography, the title of references (including papers and books) is shown in italic fonts. The volume that each technical paper belongs is emphasized with bold font, followed by the number of the starting page and the year of publication.

Chapter 2
The 2D Model for Single-Chamber SOFC

2.1 Background

The numerical model was developed in collaboration with the experimental research in Haile's group at Caltech into the stacked anode-supported SCFC. The model is based on first principles that govern the operation of the fuel cell, and is tailored to the requirements of the experimental design. Important parameters of the model are calibrated by the experimental measurement of the fuel cell performance, and comparison between the model prediction and independent experimental measurement is used to examine the validity of the model. The theoretical part of the model development is discussed in this chapter, and the model calibration and prediction are discussed in the next chapter.

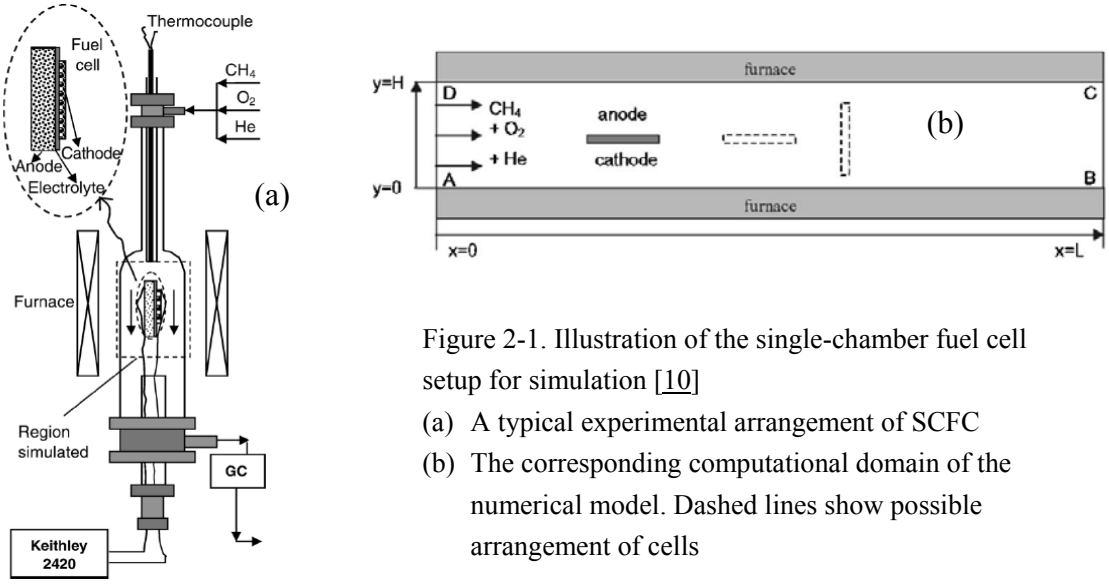

Figure 2-1. Illustration of the single-chamber fuel cell setup for simulation [10]
(a) A typical experimental arrangement of SCFC
(b) The corresponding computational domain of the numerical model. Dashed lines show possible arrangement of cells

The experimental setup of a typical single-chamber fuel cell is shown in Fig. 2-1a. The premixed gas stream (oxygen + methane + helium) is supplied through the top of the reactor and the cells are placed either parallel or perpendicular to the streamwise direction. The reactor is surrounded and heated by a tube furnace. Within the porous anode, H_2 is generated through the direct and indirect reactions of methane with oxygen and water (due to electrochemistry) and oxidized electrochemically over a reaction zone, which extends from the anode-electrolyte interface into the anode. On the cathode side, oxygen is electrochemically reduced to oxygen, and the ions are transported across the electrolyte to react with hydrogen on the anode side. The current-voltage (I-V) characteristics are monitored and recorded real-time, and the exhaust is analyzed by gas chromatograph.

The part of the reactor that contains the fuel cell is the focus of the work presented here. Corresponding to the experimental setup, the computational domain is defined as the rectangular region of length L and height H that contains one or more cells in Fig. 2-1b. The height of the domain is the same as the diameter of the reactor, and the dimension of the fuel cell is the same as in the experiment. Reasonable lengths are allowed upstream and downstream of the cell to let the channel flow fully develop. The top and bottom walls of the channel are assumed to have a constant temperature to simulate the furnace in actual experiments. The mixture of methane, oxygen, and a carrier gas (usually helium) comes into the domain from the left side at a specified speed, converted from the experimental flow rate (discussed later). Compared with the experimental device, the computational domain is horizontal because it has been

verified both experimentally and numerically that the influence of gravity on fuel cell performance is negligible.

2.2 The Numerical Model

The complexity of the situation illustrated in Fig. 2-1 requires that several submodels, each developed on the basis of first principles and experimental input, be utilized and appropriately coupled to describe the complete fuel cell system. Based on the discussion in the first chapter, the objective of this model is to simulate the steady state performance of multiple planar-stacked single-chamber SOFCs though two-dimensional modeling at different length scales corresponding to different components of the fuel cell. The individual submodels should describe:

1. Gas flow characteristics surrounding the fuel cell,
2. Chemical reaction and transport within the porous electrodes,
3. Heat generation and transfer,
4. Electrochemical reaction at the electrode-electrolyte interfaces, and
5. Pure ionic or mixed ionic and electronic conductivity of the ceria electrolyte.

In particular, the electrical performance of each cell and interaction among the cells at steady state are simulated by solving the coupled partial differential equations described below.

The model structure is illustrated in Fig. 2-2. The numerical model includes six modules (or submodels) that simulate different processes of the SCFC cell and stack operation. The channel flow submodel is designed to simulate the flow field

surrounding the fuel cell; the conduction and radiation model simulates the heat conduction within the fuel cell and radiation heat exchange between the fuel cell and the furnace. All other submodels belong to the chemistry solver, which simulates the diffusion and reaction processes in the MEA of the fuel cell.

The model currently only simulates the stacked SCFC. The striped SCFC, which attaches two electrodes on the same side of the electrolyte, requires more complicated calculation of the flow field and current, and so cannot be treated in the framework of this model.

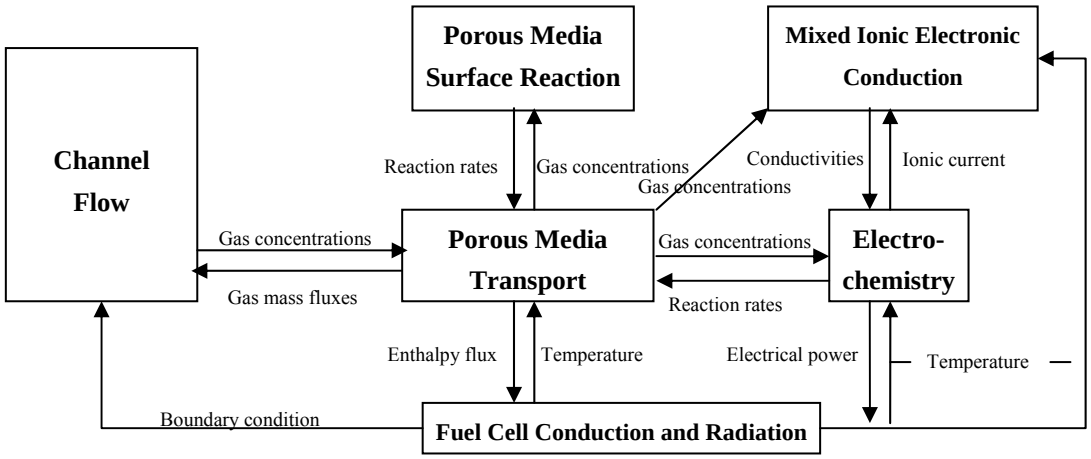

Figure 2-2. Diagram of the model structure

2.3 The Gas Channel Flow Model

The flow model solves the equations for the conservation of mass, momentum, and energy to determine the two-dimensional distributions of velocity, density, temperature, and gas-phase species in the gas chamber surrounding the fuel cell. It allows deployment of multiple cells in one chamber, with each cell either perpendicular or parallel to the streamwise direction. Simulation of a single cell can

be either isothermal or non-isothermal, while that of multiple cells is isothermal only. It is coupled to a separate model for the transport and reaction processes within the cell (described below) at the gas-cell interfaces.

2.3.1 Governing Equations and Basic Assumptions

The differential equations that describes a variable-density, Newtonian fluid flow are given as follows in a general form:

$$\frac{\partial \rho}{\partial t} + \nabla \cdot (\rho \underline{u}) = 0 \tag{2.1}$$

$$\rho \frac{\partial \underline{u}}{\partial t} + \rho \underline{u} \cdot \nabla \underline{u} = -\nabla p - \frac{2}{3} \nabla (\mu \nabla \cdot \underline{u}) + \nabla \cdot \left[\mu \left(\nabla \underline{u} + (\nabla \underline{u})^T \right) \right] \tag{2.2}$$

$$\rho c_p \frac{DT}{Dt} = \frac{Dp}{Dt} + \nabla \cdot (\lambda \nabla T) - \sum_{k=1}^{N_{\text{sp}}} c_{p,k} \underline{j}_k \cdot \nabla T - \sum_{k=1}^{N_{\text{sp}}} h_k \dot{\omega}_k W_k + \Phi \tag{2.3}$$

$$\frac{\partial Y_k}{\partial t} + \underline{u} \cdot \nabla Y_k = -\frac{1}{\rho} \nabla \cdot \underline{j}_k + \dot{\omega}_k \tag{2.4}$$

where symbols with an underscore are vectors, and those without are scalars. Symbol "∇" is the nabla operator and works with both scalars and vectors. Symbol "$\cdot$" takes the dot product of two vectors. The subscript k ($k = 1, \cdots, N_{\text{sp}}$) refers to the k^{th} species in the gas phase, where N_{sp} is the total number of gas-phase species.

The meaning of most variables can be found in the nomenclature, but some need special explanation. The material derivative of a scalar function $f(\underline{x}, t)$ is defined as

$$\frac{Df}{Dt} = \frac{\partial f}{\partial t} + \underline{u} \cdot \frac{\partial f}{\partial \underline{x}} \tag{2.5}$$

where $\underline{u}$ is the velocity vector and $\underline{x}$ is the spatial coordinate vector. It represents the total change in the quantity f as seen by an observer who is following the fluid and is watching a particular mass of the fluid. The gradient of the velocity vector, $\nabla \underline{u}$, is a

tensor, and $(\nabla \underline{u})^T$ stands for its transpose. The diffusive mass flux vector is defined as

$$\underline{j}_k = -\frac{\rho D_{k,m} W_k}{\overline{W}}\left[\nabla X_k + (X_k - Y_k)\frac{\nabla p}{p}\right] - \frac{D_k^T}{T}\nabla T \tag{2.6}$$

in which the contributions come from the spatial variations in component, pressure, and temperature. The coefficient of 2/3 in the momentum equation (2.2) is accurate for monatomic fluid and is good enough for polyatomic fluid (except for shocks).

The system of equations (2.1) to (2.4) can be further simplified for a SCFC system due to its inherent characteristics, based on which we make the following assumptions. First of all, the conservation equations can be written in a zero-Mach number, variable-density formulation. The zero-Mach number assumption applies to situations where the velocities are low (compared to the sound speed) but does not truly mean the flow speed is zero. It decouples density from pressure in the momentum equation (2.2) and eliminates the acoustic CFL restriction on time-step size, which is a condition for the stability of an explicit finite difference discretization of the partial differential equations that describe compressible fluid flows, and can put severe restrictions on the maximum allowable time-step size [6]. For fuel cell applications, the assumption of zero-Mach number is very good, since typical gas velocities are less than 1 m/s in order to provide sufficient residence time to complete the electrochemical oxidation process.

The low flow speed leads to two important conclusions: First of all, it has been calculated that with the typical flow speeds in an SCFC system, the pressure variation in the channel (typically ~10^{-2} Pa) is negligible compared with the pressure itself

(~10^5 Pa). Second, the Reynolds number based on the diameter of the channel is less than 100 under typical operating conditions of the fuel cell, and the Reynolds number based on the thickness of the fuel cell is one to two orders of magnitude smaller. Accordingly, the second assumption is that the pressure in the gas channel is nearly constant (e.g., 1 atm), and the third assumption is that the viscous heating term Φ in the energy equation (2.3) can be neglected because the flow in the channel is low-speed laminar flow. However, the pressure gradient must be retained when the velocity field is computed, since the momentum equations involve the pressure gradient but not the pressure itself. This is consistent with the constant-pressure assumption, since the pressure variation is much smaller than the ambient pressure, and very little error is introduced when calculating the velocity field with the pressure gradient.

Since the pressure and temperature of the gas mixture in a typical SCFC system is relatively low, it can be assumed that the gas mixture is an ideal gas and can be described by

$$p_0 = \rho R_g T = \rho R T \sum_{k=1}^{K} \frac{Y_k}{W_k} . \tag{2.7}$$

It should be pointed out that since the pressure is nearly constant, the density variation in the channel flow results from the spatial variation of the chemical composition (and therefore mean molecular weight), as well as the temperature of the gas, but not from the finite Mach number.

Although the chemical composition varies significantly in the gas channel of an SCFC system, this is mostly due to the catalytic surface reactions and

electrochemistry within the membrane-electrode assembly (MEA). In this study, we assume the gas-phase chemistry is negligible (i.e., $\dot{\omega} = 0$), because the operating temperature of SCFC is not high enough. Gupta et al. [65] reported that at temperatures below 800°C and residence times of a few seconds only a small percent of the methane fuel is reacted in homogeneous reactions. Walters et al. [54] have shown through simulation that the temperature needs to approach 900°C for gas-phase chemistry to play a substantial role for SOFCs using natural gas as a fuel.

2.3.2 Simplification of the Governing Equations

Based on the assumptions above, equations (2.1) to (2.4) can be further simplified. Before making these changes, the momentum, energy, and species conservation equations are rewritten in a conservation form:

$$\frac{\partial(\rho\underline{u})}{\partial t} + \nabla\cdot(\rho\underline{u}\underline{u}) = -\nabla p - \frac{2}{3}\nabla(\mu\nabla\cdot\underline{u}) + \nabla\cdot\left[\mu\left(\nabla\underline{u} + (\nabla\underline{u})^T\right)\right] \tag{2.8}$$

$$\frac{\partial(\rho T)}{\partial t} + \nabla\cdot(\rho\underline{u}T) = \frac{1}{c_p}\nabla\cdot(\lambda\nabla T) - \frac{1}{c_p}\sum_{k=1}^{N_{sp}} c_{p,k}\underline{j}_k\cdot\nabla T \tag{2.9}$$

$$\frac{\partial(\rho Y_k)}{\partial t} + \nabla\cdot(\rho\underline{u}Y_k) = -\nabla\cdot\underline{j}_k\,. \tag{2.10}$$

In a Cartesian coordinate, the nabla operator can be formulated as

$$\nabla = \frac{\partial}{\partial x}\hat{x} + \frac{\partial}{\partial y}\hat{y} \tag{2.11}$$

where $\hat{x}$ and $\hat{y}$ are the unit vector in the x and y directions respectively. The continuity equation is recast in a Cartesian form

$$\frac{\partial\rho}{\partial t} + \frac{\partial(\rho u)}{\partial x} + \frac{\partial(\rho v)}{\partial y} = 0\ . \tag{2.12}$$

In the momentum equation (2.8),

$$\begin{aligned}\nabla\cdot(\rho\underline{\underline{uu}}) &= \left(\partial_x\hat{x}+\partial_y\hat{y}\right)\cdot\left(\rho uu\hat{x}\hat{x}+\rho uv\hat{x}\hat{y}+\rho vu\hat{y}\hat{x}+\rho vv\hat{y}\hat{y}\right)\\ &= (\rho uu)_x\,\hat{x}+(\rho uv)_x\,\hat{y}+(\rho vu)_y\,\hat{x}+(\rho vv)_y\,\hat{y}\\ &= \left[(\rho uu)_x+(\rho uv)_y\right]\hat{x}+\left[(\rho uv)_x+(\rho vv)_y\right]\hat{y}\end{aligned} \tag{2.13}$$

and the divergence of the velocity gradient terms needs special attention,

$$\begin{aligned}\nabla\cdot[\mu(\nabla\underline{u})] &= \nabla_i\hat{e}_i\cdot\left(\mu\nabla_j\hat{e}_j u_k\hat{e}_k\right)=\nabla_i(\mu\nabla_i)u_k\hat{e}_k\\ &= \left[\frac{\partial}{\partial x}\left(\mu\frac{\partial u}{\partial x}\right)+\frac{\partial}{\partial y}\left(\mu\frac{\partial u}{\partial y}\right)\right]\hat{x}+\left[\frac{\partial}{\partial x}\left(\mu\frac{\partial v}{\partial x}\right)+\frac{\partial}{\partial y}\left(\mu\frac{\partial v}{\partial y}\right)\right]\hat{y}\end{aligned} \tag{2.14}$$

and

$$\begin{aligned}\nabla\cdot\left[\mu(\nabla\underline{u})^T\right] &= \nabla_i\hat{e}_i\cdot\left[\mu\left(\nabla_j\hat{e}_j u_k\hat{e}_k\right)^T\right]\\ &= \nabla_i\hat{e}_i\cdot\left(\mu\hat{e}_k\hat{e}_j\nabla_j u_k\right)=\nabla_i\left(\mu\nabla_j u_i\right)\hat{e}_j\\ &= \left[\frac{\partial}{\partial x}\left(\mu\frac{\partial u}{\partial x}\right)+\frac{\partial}{\partial y}\left(\mu\frac{\partial v}{\partial x}\right)\right]\hat{x}+\left[\frac{\partial}{\partial x}\left(\mu\frac{\partial u}{\partial y}\right)+\frac{\partial}{\partial y}\left(\mu\frac{\partial v}{\partial y}\right)\right]\hat{y}\end{aligned} \tag{2.15}$$

where $\hat{e}_i$ ($i=1,2$) is the i^{th} unit vector of the Cartesian coordinate. Substituting (2.13) through (2.15) into (2.8), we get the momentum equations in x and y directions

$$\frac{\partial\rho u}{\partial t}+\frac{\partial\rho uu}{\partial x}+\frac{\partial\rho uv}{\partial y}=-\frac{\partial p}{\partial x}+\frac{4}{3}\frac{\partial}{\partial x}\left(\mu\frac{\partial u}{\partial x}\right)+\frac{\partial}{\partial y}\left(\mu\frac{\partial u}{\partial y}\right)+\frac{\partial}{\partial y}\left(\mu\frac{\partial v}{\partial x}\right)-\frac{2}{3}\frac{\partial}{\partial x}\left(\mu\frac{\partial v}{\partial y}\right) \tag{2.16}$$

$$\frac{\partial\rho v}{\partial t}+\frac{\partial\rho uv}{\partial x}+\frac{\partial\rho vv}{\partial y}=-\frac{\partial p}{\partial y}+\frac{\partial}{\partial x}\left(\mu\frac{\partial v}{\partial x}\right)+\frac{4}{3}\frac{\partial}{\partial y}\left(\mu\frac{\partial v}{\partial y}\right)+\frac{\partial}{\partial x}\left(\mu\frac{\partial u}{\partial y}\right)-\frac{2}{3}\frac{\partial}{\partial y}\left(\mu\frac{\partial u}{\partial x}\right) \tag{2.17}$$

To simplify the energy equation and species conservation equation, the diffusive mass flux $\underline{j_k}$, the most complicated term in both equations, needs to be simplified first. The terms in (2.6) are compared by their order of magnitude, and insignificant terms can be dropped. We first compare ∇X_k and $(X_k-Y_k)\frac{\nabla p}{p}$. For the purpose of the comparison of magnitudes, we first study the x direction and take the ratio of these two terms, with spatial derivatives being approximated by spatial differences.

$$\left[(X_k-Y_k)\frac{\nabla p}{p}\Big/\nabla X_k\right]_x=(X_k-Y_k)\frac{\partial p}{\partial x}\Big/\left(p\frac{\partial X_k}{\partial x}\right)\approx\frac{X_k-Y_k}{\Delta X_k}\frac{\Delta p}{p} \tag{2.18}$$

By definition, the molar fraction X_k and mass fraction Y_k are both of the order of 1, and in a typical SCFC system, the variation of pressure can be easily estimated with the Hagen-Poiseuille flow theory. For example, at 900K, with an average inlet flow

speed of 1cm/sec, the pressure drop along a channel of 20 cm in length (and 1cm in diameter) is of the order 10^{-3} Pa. However, the variation of X_k along the same length is expected to be of the same order of magnitude as X_k. Therefore, the ratio in (2.18) is very small (~10^{-8}) and thus the pressure gradient term can be dropped. This conclusion also applies to the y direction, since for channel flows, the variations in the y direction are less significant.

Therefore the flux expression in (2.6) can be simplified as

$$\underline{j}_k = -\frac{\rho D_{k,m} W_k}{\overline{W}} \nabla X_k - \frac{D_k^T}{T} \nabla T \ . \tag{2.19}$$

Since the natural variable for the species conservation equation is the mass fraction Y_k, it would be more convenient if the flux were represented in terms of mass fraction rather than mole fraction. This can be done at the expense of introducing mean-molecular-weight gradients using the following relation:

$$X_k W_k = Y_k \overline{W} \quad . \tag{2.20}$$

The first term in (2.18) can then be expanded into two terms

$$\frac{\rho D_{k,m} W_k}{\overline{W}} \nabla X_k = \rho D_{k,m} \nabla Y_k + \rho \frac{Y_k}{\overline{W}} D_{k,m} \nabla \overline{W} \tag{2.21}$$

Reference [66] points out that, for flows that have relatively small mean molecular weight gradients $\nabla \overline{W}$, the second term may be negligible; this also applies in the case of SCFC because a dominant amount (over 50 vol%) of inert carrier gas (also called balance gas), usually helium or nitrogen, is always present in the system to alleviate the intense heat release of the MEA by carrying away the excessive reaction heat and reducing the possibility of explosion. This assumption also applies well to studies on

gas-phase combustion [67] with abundant carrier gas, and so the second term in (2.21) can be safely dropped and the flux reduced to

$$\underline{j_k} = -\rho D_{k,m} \nabla Y_k - \frac{D_k^T}{T} \nabla T \qquad . \tag{2.22}$$

A quantitative comparison (Appendix B) shows that under typical SCFC operating conditions, the first term in (2.22) is usually over three orders of magnitude greater than the second term, and so neglecting the latter won't introduce significant numerical errors. Finally, the mass flux is reduced to

$$\underline{j_k} = -\rho D_{k,m} \nabla Y_k \qquad . \tag{2.23}$$

Substituting (2.23) into (2.9) and (2.10), we have:

$$\begin{aligned} \frac{\partial(\rho T)}{\partial t} + \frac{\partial(\rho u T)}{\partial x} + \frac{\partial(\rho v T)}{\partial y} = \frac{1}{c_p}\left[\frac{\partial}{\partial x}\left(\lambda \frac{\partial T}{\partial x}\right) + \frac{\partial}{\partial y}\left(\lambda \frac{\partial T}{\partial y}\right)\right] \\ + \frac{\rho}{c_p} \sum_{k=1}^{N_{sp}} c_{p,k} D_{k,m} \left(\frac{\partial Y_k}{\partial x}\frac{\partial T}{\partial x} + \frac{\partial Y_k}{\partial y}\frac{\partial T}{\partial y}\right) \end{aligned} \tag{2.24}$$

$$\frac{\partial(\rho Y_k)}{\partial t} + \frac{\partial(\rho u Y_k)}{\partial x} + \frac{\partial(\rho v Y_k)}{\partial y} = \frac{\partial}{\partial x}\left(\rho D_{k,m} \frac{\partial Y_k}{\partial x}\right) + \frac{\partial}{\partial y}\left(\rho D_{k,m} \frac{\partial Y_k}{\partial y}\right) . \tag{2.25}$$

The simplified momentum equations (2.16), (2.17), energy equation (2.24), species mass conservation equation (2.25), together with the continuity equation (2.12), are used for the derivation below.

2.3.3 Boundary Conditions

The system of governing equations (PDEs) is elliptic and therefore boundary conditions must be given at all the boundaries of the computational domain. At the channel inlet, flow rates of all species are given, and thus velocity and initial composition is known. Temperature is also specified there. At the channel outlet, the flow is assumed to be fully specified such that there is no variation along the x

direction for any variable. At the top and bottom walls of the channel, non-slip conditions apply to the velocity field, and temperature is specified. Since no chemistry occurs at these two boundaries, the mass flux of all species is zero. On the MEA surfaces that are interfaces between the electrode and the channel flow, mass fluxes are non-zero and so is the velocity component perpendicular to the surfaces. The MEA temperature has a 1-D distribution in its length direction evaluated by another module (discussed later), and for the flow solver, the surface temperature of the MEA is regarded as known. The mass concentration of species is unknown, but can be evaluated using the mass fluxes as boundary conditions. The other two surfaces of the MEA have similar boundary conditions except that mass fluxes and velocity are both zero. The boundary conditions are formulated and summarized in Table 2-1.

Table 2-1. Boundary Conditions for the Gas Channel Flow Model

	u	v	Y_k	T
Inlet	u_{in}	$v = 0$	$\underline{n} \cdot \left(\rho Y_k \underline{u} + \underline{j_k}\right) = \rho_{\text{in}} u_{\text{in}} Y_{k,\text{in}}$	T_{in}
Outlet	$\frac{du}{dx} = 0$	$\frac{dv}{dx} = 0$	$\underline{n} \cdot \underline{j_k} = 0$	$\frac{dT}{dx} = 0$
Top and bottom walls	$u = 0$	$v = 0$	$\frac{dY_k}{dy} = 0$	T_{furnace}
MEA Surface	$u = 0$	Same as Y_k	$\underline{n} \cdot \left(\rho Y_k \underline{u} + \underline{j_k}\right) = \dot{s}_k W_k$	$T_{\text{cell}}(x)$

$\underline{n}$: Outward unit normal vector; $\underline{j_k} = -\rho D_{k,m} \nabla Y_k$

Strictly speaking, the inlet boundary condition of the energy equation should also take the flux form as for the species equation since the two equations are very similar. However, calculation indicates that the backward thermal diffusion from downstream to the inlet causes unnoticeable variation of the temperature at the inlet from the

preset temperature value. This is also true for all gas phase species except hydrogen. Therefore, the constant boundary condition for temperature is good enough.

2.3.4 Non-Dimensionalization of Equations and Boundary Conditions

By casting the governing equations in a non-dimensional form, important insights in the equations can be revealed. Also, for generality considerations (e.g., different measures) and numerical implementation considerations (e.g., different scales), it's a good practice to solve the PDEs in a non-dimensional form. The process of non-dimensionalization starts with the choice of scales, and basic scales include length, time, mass, etc. For the flow problem described by equations (2.12), (2.16), (2.17), (2.24), and (2.25), the basic parameters are listed in Table 2-2, and each of the parameters is denoted by a subscript "0".

Table 2-2 Basic Parameters for Nondimensionalization of Governing Equations

Symbol	Value and Meaning
d_0	Height of the flow channel
u_0	0.01 m/sec; reference velocity
ρ_0	0.4 kg/m^3; reference density
T_0	1000 K; reference temperature
c_{p0}	10^6 J/kg/K; reference specific heat of constant pressure
λ_0	7.5 W/m/K; reference thermal conductivity
μ_0	10^{-5} N·sec/m^2; reference dynamic viscosity
D_0	10^{-4} m^2/sec; reference mass diffusion coefficient

The value of d_0 might change with different cases and thus is not given here. Based on this table, there are a few derived basic parameters that are also very useful, including the reference time $t_0 = d_0 / u_0$, reference pressure $p_0 = \rho_0 u_0^2$, and the kinematic viscosity $\nu_0 = \mu_0 / \rho_0$. Also, the following dimensionless numbers are defined:

$$\mathrm{Re}_0 = \frac{\rho_0 u_0 d_0}{\mu_0},\ \mathrm{Re} = \frac{\rho_0 u_0 d_0}{\mu},\ \mathrm{Pr}_0 = \frac{\mu_0 c_{p0}}{\lambda_0},\ \mathrm{Sc}_0 = \frac{\mu_0}{\rho_0 D_0}\ .$$

For a typical channel height of $d_0 = 15$ mm, the values of Re_0, Pr_0 and Sc_0 are 6.0, 1.33 and 0.25, respectively. The difference between Re_0 and Re is that the latter is defined by $\mu(x,y)$, the local dynamic viscosity of the fluid. Gas properties such as viscosity, diffusivity, thermal conductivity, and specific heat are calculated by Cantera [68] at each point of the flow field based on the local temperature and gas concentrations, which are important for the accurate simulation of the flow field. With these basic parameters and dimensionless parameter groups, the governing equations can be nondimensionalized. For the convenience of formulation, a short-hand notation is used, in which the subscripts "x" or "y" or "t" of a variable indicate taking the corresponding derivative of the variable (e.g., $u_x = \partial u / \partial x$). Details of the derivation is neglected, and the dimensionless governing equations are:

$$\rho_t + (\rho u)_x + (\rho v)_y = 0 \tag{2.26}$$

$$(\rho u)_t + (\rho u u)_x + (\rho u v)_y = -p_x + \frac{4}{3}\left(\frac{u_x}{\mathrm{Re}}\right)_x + \left(\frac{u_y}{\mathrm{Re}}\right)_y + \left(\frac{v_x}{\mathrm{Re}}\right)_y - \frac{2}{3}\left(\frac{v_y}{\mathrm{Re}}\right)_x \tag{2.27}$$

$$(\rho v)_t + (\rho u v)_x + (\rho v v)_y = -p_y + \left(\frac{v_x}{\mathrm{Re}}\right)_x + \frac{4}{3}\left(\frac{v_y}{\mathrm{Re}}\right)_y + \left(\frac{u_y}{\mathrm{Re}}\right)_x - \frac{2}{3}\left(\frac{u_x}{\mathrm{Re}}\right)_y \tag{2.28}$$

$$\begin{aligned}(\rho T)_t + (\rho u T)_x + (\rho v T)_y = {} & \frac{(\lambda T_x)_x + (\lambda T_y)_y}{\mathrm{Re}_0\,\mathrm{Pr}_0\,c_p} \\ & + \frac{\rho}{\mathrm{Re}_0\,\mathrm{Sc}_0\,c_p}\sum_{k=1}^{N_{\mathrm{sp}}} c_{pk} D_{k,m}\left[(Y_k)_x T_x + (Y_k)_y T_y\right]\end{aligned} \tag{2.29}$$

$$(\rho Y_k)_t + (\rho u Y_k)_x + (\rho v Y_k)_y = \frac{1}{\mathrm{Re}_0\,\mathrm{Sc}_0}\left[\left(\rho D_{k,m}(Y_k)_x\right)_x + \left(\rho D_{k,m}(Y_k)_y\right)_y\right]\ . \tag{2.30}$$

The dimensionless boundary conditions have the same form as Table 2-1, with the only difference being the dimensionless mass flux $\underline{j_k} = -\rho D_{k,m} \nabla Y_k / \mathrm{Re}_0 / \mathrm{Sc}_0$.

2.3.5 Computation Grid and Discretization

Equations (2.26) through (2.30) are discretized and solved by the SIMPLEC algorithm, an improved version of the standard SIMPLE algorithm (Semi-Implicit Method for Pressure-Linked Equations) developed by Patankar and Spalding [69]. It is originally an iterative method for solving the momentum equations for laminar flow problems in their discretized form. Now since in the SCFC system the momentum equations (2.27) and (2.28) are coupled to the other three equations, they must be solved together implicitly.

The SIMPLE-based methods have a few advantages for SCFC modeling [70]. First, it is an iterative approach, which is commonly used to solve a whole set of discretized equations. Using a direct solution for solving the entire sets of velocity and pressure components is more difficult. Second, it applies to the situations where the pressure variation is not linked to density, and where there exists a coupling between the pressure and velocity that introduces a constraint on the solution of the flow field. Determining the unknown pressure field is the real difficulty in calculating the velocity field, since there is no obvious equation to solve; thus pressure is used to satisfy the condition for continuity. The SIMPLE-based methods solve this by indirectly specifying the pressure field via the continuity equation, achieved by obtaining a whole set of discretized equations from the momentum and continuity equations and solving the discretized equations by a direct solution. More details can be found in [69].

The SIMPLEC algorithm uses a staggered grid (Fig. 2-3) to discretize the equations. That is, scalar variables such as pressure, temperature, and density are calculated at the center, while the velocity components are calculated for the points that lie on the faces of the control volumes [69]. Dimensions of the control volumes in the grid can be changed, so that the grid can be refined locally. Details of the discretization are discussed in Appendix C, and the discretized equation has a general form

$$a_{i,j}\phi_{i,j}^{n+1} + a_{i+1,j}\phi_{i+1,j}^{n+1} + a_{i-1,j}\phi_{i-1,j}^{n+1} + a_{i,j+1}\phi_{i,j+1}^{n+1} + a_{i,j-1}\phi_{i,j-1}^{n+1} = b_{i,j}^{n} \tag{2.31}$$

and can be written in a matrix form

$$\mathbf{AX} = \mathbf{B} \tag{2.32}$$

with $\phi_{i,j}$ representing the unknown scalar variable ϕ defined on grid point (i,j), superscript n representing the current time level, and n+1 representing the next time

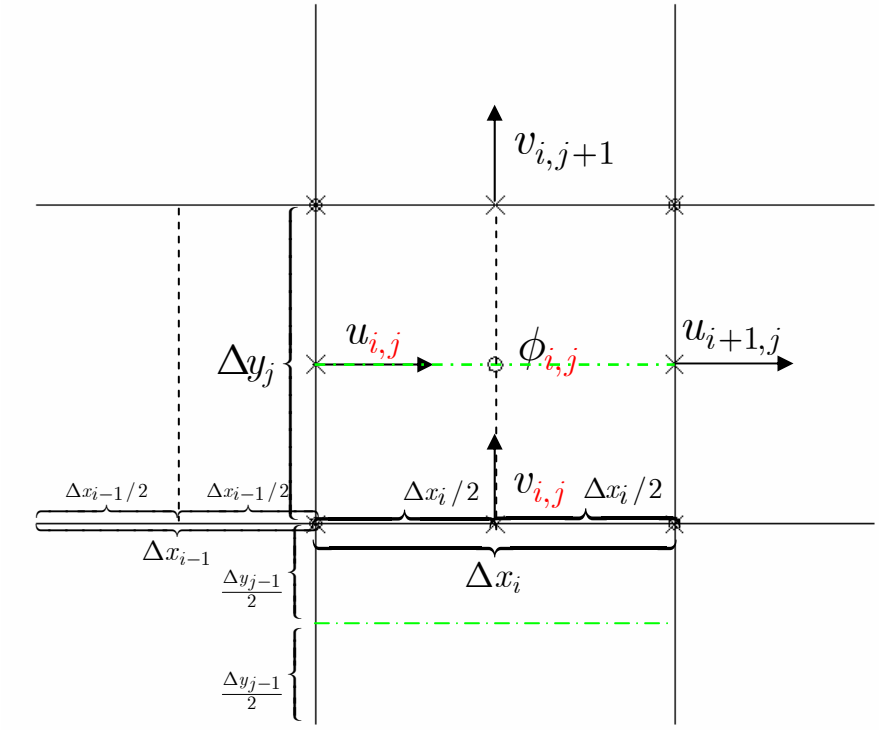

Figure 2-3. The staggered grid of the SIMPLEC algorithm

level. **A** is the coefficient matrix consisting of all the discretized coefficients a in (2.31), and **X** and **B** are respectively the vector of unknowns and vector of source terms in the same equation. Matrix equation (2.32) is solved by the bi-conjugate gradient method.

2.4 The Porous Electrode Transport Model

In order to determine the gas composition at the electrode/electrolyte interface, where the electrochemistry is assumed to take place, it is necessary to compute the coupled problem of transport and reaction within the porous electrodes. Gaseous reactions are neglected and only reactions occurring on the catalyst particle surfaces are considered, due both to the low temperature and to the small pore size, comparable to the mean free path for the molecular species.

The porous electrode model is formulated in terms of the gaseous species of the flow model, and in addition a set of adsorbed surface species on the catalyst particle surfaces with which the gaseous species may react. The mass concentrations $\rho_k \left(k = 1,\cdots,N_{\mathrm{sp}}\right)$ of the gaseous species in the pores are determined by solving the porous-media gaseous species conservation equation

$$\nabla \cdot \underline{j_k} = A_c W_k \dot{s}_k,\ k = 1,\cdots,N_{\mathrm{sp}} \tag{2.33}$$

where $\underline{j_k}$, W_k, and $\dot{s}_k$ are the diffusive mass flux, molecular weight, and molar production rate on the catalyst surface of species k, respectively; A_c is the volumetric specific surface area of the catalyst; and N_{sp} is the number of gaseous species. The mass flux $\mathbf{j}_k$ depends on the gradient of ρ_k, and is evaluated by the Dusty-Gas Model

(DGM) [57]. The DGM used in this study accounts for the major mechanisms for gaseous molecular transport in porous media, including bulk molecular diffusion, Knudson diffusion, and Darcy flow [57, 71]. Zhu et al. [56] have discussed the application of this model to an SOFC anode in detail.

The coverage fractions (or coverages) $\theta_k\,(k = 1,\cdots,N_s)$ of the surface species are computed self-consistently with the gaseous species, by requiring that the surface species are all in steady state, and therefore their net chemical production rates are zero:

$$\dot{s}_k = 0,\ \ k = 1,\cdots,N_s \tag{2.34}$$

where N_s is the total number of surface species, and $\dot{s}_k$ is supplied by the heterogeneous chemistry mechanism (for the anode) that will be discussed shortly.

The electrode sub-model is formulated as a steady-state model, even though the flow model, to which it is coupled, is formulated in a time-dependent form. This formulation is advantageous, since the inclusion of fast reactions would otherwise make the system of equations (2.33) and (2.34) stiff, and would require very small time steps and long computation times. Since only the steady-state solution is of interest, there is no error introduced by this procedure. The steady-state model allows solving equations (2.33) and (2.34) fully implicitly using the damped Newton's method for stiff systems. Given the mass fractions of the gaseous species at the electrode/gas interface, it solves for the steady-state species fluxes through the electrode and surface coverages. The computed fluxes at the electrode/gas interface are fed back to the flow model, where they are incorporated into the discretized

species conservation equations as boundary conditions, and the interface velocity u or $v = \sum_{k=1}^{K} j_k / \rho$ is used as the boundary condition for the momentum equations (2.27) or (2.28).

2.5 Heterogeneous Chemistry

For the calculations presented in this work, an elementary multi-step reaction mechanism [56] that accounts for the partial oxidation and steam reforming of methane over a Ni surface is used. The mechanism consists of 46 heterogeneous reactions between 6 gaseous species and 13 adsorbed surface species. It is designed for typical SOFC operating conditions (temperature and gas components) and has been validated by Hecht et al experimentally [61]. However, this mechanism is not designed to predict coking, where the concentration of oxygen in the gas channel is so low that carbon deposits over the anode catalyst surface. Therefore, only fuel-to-oxygen ratios for which coking is not a problem are considered.

The reaction mechanism for the catalyst in the cathode is a global mechanism of methane full oxidation over $Ba_{0.5}Sr_{0.5}Co_{0.8}Fe_{0.2}O_{3-\delta}$ (BSCF) developed by Mederos et al. [10]. It was found that carbon-bearing products were almost entirely CO_2, and the reaction rate of methane to CO_2 was fit to the expression $r = k \cdot P_{\mathrm{CH_4}}^{\mathrm{m}} \cdot P_{\mathrm{O_2}}^{\mathrm{n}}$, where the rate constant $k = k_0 \exp(-E_{\mathrm{a}} / RT)$, and the exponents *m* and *n* were found to be independent of temperature. The oxidation rates of hydrogen and carbon monoxide over the BSCF catalyst surface were not measured and the oxidation reactions are assumed to be instantaneous, because both species are present in the cathode due to

gas diffusion in the channel flow from the anode side of the cell, and their concentrations are much lower than that of methane.

2.6 The Electrochemistry Model

This model computes the current density as a function of distance *x* from the MEA leading edge given the load potential. It makes the following assumptions: First, electrochemical reactions take place only at the electrode/electrolyte interfaces and are treated as boundary conditions for the porous transport module below. Second, the flow of oxygen-ion current through the electrolyte is assumed to be one-dimensional across the electrolyte from the anode to the cathode. Third, the electrochemistry consists only of the reduction of atmospheric oxygen at the cathode, and the oxidation of hydrogen at the anode. (Although H_2 and CO are both electrochemically active fuels, there is strong evidence that on the anode side, H_2 dominates the charge-transfer chemistry, and water-gas-shift chemistry replenishes the H_2 via reaction of CO with the H_2O that is a product of the H_2 charge transfer [72]). Finally, the ohmic resistance of the electrodes is negligible.

With these assumptions, the relationship between current density and potential difference can be derived. For pure ionic conductor electrolytes such as YSZ, the current density is of course ionic, and a detailed discussion can be found in [3]. For mixed ionic and electronic conductor electrolytes that will be discussed shortly, the derivation of the ionic current in [3] still applies. Subscripts “i” and “e” are used to

denote “ionic” and “electronic” respectively. The ionic current density $i_{\mathrm{i}}(x)$ is obtained from

$$E = E^0 - \frac{L_{\mathrm{e}} i_{\mathrm{i}}}{\sigma_{\mathrm{i}}(T)} - \eta_{\mathrm{act,c}}(i_{\mathrm{i}}) - \eta_{\mathrm{act,a}}(i_{\mathrm{i}}) \tag{2.35}$$

by Newton iteration with charge-transfer overpotentials $\eta_{\mathrm{act,a}}$ and $\eta_{\mathrm{act,c}}$ at the electrode-electrolyte interfaces obtained by solving the Butler-Volmer equation

$$i_{\mathrm{i}} = i_0[\exp(\alpha_{\mathrm{a}}\eta_{\mathrm{act}}f) - \exp(-\alpha_{\mathrm{c}}\eta_{\mathrm{act}}f)], \quad f = F/(RT) \tag{2.36}$$

at the anode- and cathode-electrolyte interfaces respectively. Here L_{e} is the electrolyte thickness, $\sigma_{\mathrm{i}}(T)$ is the electrolyte ionic conductivity, E is the load potential, and E^0 is the Nernst potential defined by

$$E^0 = -\frac{\Delta G^0}{2F} + \frac{RT}{2F}\ln\frac{p_{\mathrm{H_2}} p_{\mathrm{O_2}}^{1/2}}{p_{\mathrm{H_2O}}} \tag{2.37}$$

where ΔG^0 is the standard free energy of the reaction $\mathrm{H_2} + \frac{1}{2}\mathrm{O_2} \rightleftharpoons \mathrm{H_2O}$, the partial pressures $p_{\mathrm{H_2}}$ and $p_{\mathrm{H_2O}}$ are evaluated at the anode-electrolyte interfaces solved from the porous electrode transport model, and $p_{\mathrm{O_2}}$ is evaluated at the cathode-electrolyte interface obtained in the same way. As for other symbols in the equations above, i_0 is the exchange current density, α_{a} and α_{c} are the anodic and cathodic asymmetry factors for each of the electrodes, F is Faraday’s constant, and R is the universal gas constant. Compared with other parameters, α_a and α_c are relatively more difficult to measure by experiment. In this model, they are treated as free fitting parameters. For charge transfer processes that include more than one step, the values of the asymmetry factors can be greater than 1 [56].

Based on the first assumption made at the beginning of this section, the non-zero mass fluxes j_k at the electrode-electrolyte interfaces can be computed when $i_{\mathrm{i}}(x)$ is

known (where k stands for H_2, H_2O, or O_2). While this assumption is good for the thick anode, it is a simplification for the thin cathode, since it is known that the electrochemically active region extends at least ten microns into the porous electrode [55]. However, modeling distributed electrochemistry coupled to catalytic chemistry is complex, and beyond the scope of this work. We will address this point in a future publication. At the anode-electrolyte interface

$$j_{H_2} = -\frac{i_i(x)W_{H_2}}{2F}, j_{H_2O} = \frac{i_i(x)W_{H_2O}}{2F} \tag{2.38}$$

and at the cathode-electrolyte interface

$$j_{O_2} = -\frac{i_i(x)W_{O_2}}{4F} \tag{2.39}$$

where W_k is the molecular weight for species k. These fluxes are used as boundary conditions for the porous electrode transport model. The set of equations (2.33) to (2.36) is solved simultaneously by Newton iteration.

2.7 The Mixed-Ionic Electronic Conductor (MIEC) Model

MIECs are materials that conduct both ionic and electronic charge carriers [73]. Due to their high ionic conductivity, MIECs have found increasing application as electrolytes in SOFCs operated at reduced temperatures. Hibino et al. reported that ohmic resistances of $La_{0.9}Sr_{0.1}Ga_{0.8}Mg_{0.2}O_3$ (LSGM) and $Ce_{0.8}Sm_{0.2}O_{1.9}$ (SDC, 0.2 mm thick, 0.5cm^2 cross-section area) are 1.56 and 1.72 Ω at 700^{o}C, respectively (considerably lower than the 2.90 Ω of YSZ), and concluded that LSGM is the most suitable electrolyte for an SCFC [74].

The model is capable of simulating SCFCs with either pure ionic conductor or MIEC electrolytes. For YSZ, the electrolyte sub-model is simple. The ionic conductivity in (2.35) has the following form:

$$\sigma_{\mathrm{i}}(T) = \frac{\sigma_0}{T}\exp\left(-\frac{E_a}{RT}\right) . \tag{2.40}$$

For an MIEC electrolyte, we adopt the model developed by Riess et al and Gödickemeier et al [75–77]. However, our formulation is much simpler in that the gas concentrations at the electrode-electrolyte interfaces can be directly obtained from the solution of the porous electrode model, while they had to be evaluated through an assumed transport model for the porous electrodes in these references in order to take the concentration overpotential into account correctly. As a result, our description of the MIEC electrolyte employs equations (2.35) and (2.36) to compute ionic current i_{i}, and the electronic current is computed by

$$i_{\mathrm{e}}(x) = -i_{\mathrm{i}}\frac{\sigma_{\mathrm{e}}\left(p_{\mathrm{O}_2}^{\mathrm{C}}\right)}{\sigma_{\mathrm{i}}(T)}e^{\eta_{\mathrm{C}}f}\frac{e^{E\cdot f}-1}{1-e^{-i_{\mathrm{i}}L_{\mathrm{e}}f/\sigma_{\mathrm{i}}}} \tag{2.41}$$

where for the SDC electrolyte of interest here, the electronic conductivity is given by [78]

$$\sigma_{\mathrm{e}}\left(p_{\mathrm{O}_2}\right) = kp_{\mathrm{O}_2}^{-1/4},\ k = aT^{-1}e^{-b/T} . \tag{2.42}$$

Lai et al [78] have systematically studied the electronic and ionic transport properties of SDC, based on which $a = 2.42\times10^{8}\,\mathrm{K}\ \Omega^{-1}\mathrm{cm}^{-1}\mathrm{atm}^{0.25}$ and $b = 2.69\times10^{4}\,\mathrm{K}$ are used for this study. The ionic conductivity σ_{i} assumes the form of equation (2.40). The total current density is the sum of the ionic and electronic currents, i.e.,

$$i_{\mathrm{tot}} = i_{\mathrm{i}} + i_{\mathrm{e}} , \tag{2.43}$$

and is the current output to external circuits.

2.8 The Conduction and Radiation Model

This model predicts the cell temperature, which is a crucial factor for the electrical performance since it dictates reaction rates and electrolyte conductivity. Shao et al. found experimentally that the cell usually runs significantly higher than the furnace temperature [21]. Therefore a complete model must be able to predict this trend.

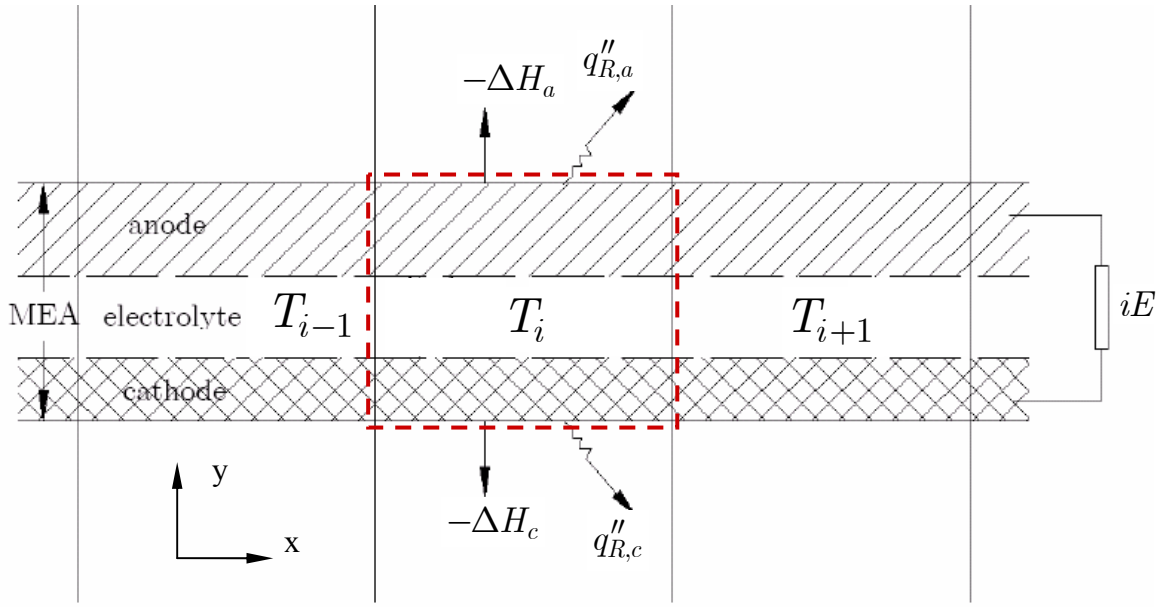

Figure 2-4. Energy balance over a control volume (dashed line) in the cell. T : cell temperature; q''_R : radiation heat flux; ΔH : enthalpy change; iE : power output on external load; subscripts "a" and "c" stand for anode and cathode respectively

Fig. 2-4 shows schematically the energy exchange processes, including conduction within the cell, enthalpy changes at the electrodes, and radiation heat exchange between the furnace and one control volume of the cell. The control volumes coincide with the flow model grid for scalar variables. Since the thickness of the cell is much smaller than its length and the thermal conductivity is high, it's a

good assumption that the cell temperature is uniform along any perpendicular cross-section and is a function of *x* only, which is the distance from the cell leading edge.

The energy balance over a control volume of dimensions Δx and Δy in the cell is formulated as

$$\begin{aligned}\rho_{\mathrm{s}} c_{p,\mathrm{s}} \frac{\partial T_{\mathrm{cell}}}{\partial t} \Delta x \Delta y = & \left(q''_{\mathrm{left}} + q''_{\mathrm{right}}\right)\Delta y - i_{\mathrm{tot}} \cdot E \cdot \Delta x \\ & + \left[\left(-\Delta H\right)_{\mathrm{a}} + \left(-\Delta H\right)_{\mathrm{c}}\right]\Delta x - \left(q''_{\mathrm{R,a}} + q''_{\mathrm{R,c}}\right)\Delta x\end{aligned} \tag{2.44}$$

where ρ_{s} and $c_{p,\mathrm{s}}$ are respectively the average density and specific heat capacity of the solid material in the control volume, q''_{left} and q''_{right} are respectively the conduction heat fluxes across the left and right faces, $i_{\mathrm{tot}} \cdot E \cdot \Delta x$ is the power output to the external load, ΔH is the enthalpy change, and q''_{R} is the net radiation heat flux to the furnace (with subscripts "a" and "c" indicating the anode and cathode, respectively). This formulation takes into account both ohmic heating in the electrolyte, and the heating due to the activation overpotentials, as may be verified by substituting (2.36) into (2.44). Radiation is modeled by

$$q''_R = \sigma\varepsilon\left(T^4_{\mathrm{cell}}\langle x\rangle - T^4_{\mathrm{furnace}}\right) \tag{2.45}$$

where σ is Stefan-Boltzmann's constant and ε is the gray-body emissivity of the cell surface. The emissivity is often known only approximately and treated as a free fitting parameter (discussed later).

2.9 Coupling between the Flow Solver and the Chemistry Solver

Generally speaking, the two-dimensional SCFC model can be categorized into two parts (or solvers). Sections 2.3 and 2.8 can be considered as the solver for the channel flow including heat transfer, and Sections 2.4 through 2.7 can be considered

as the solver for the chemistry in the MEA. The two solvers are coupled at the MEA surfaces though mass and energy transport.

The two parts work in such a way that every time the flow solver advances the solution of the flow field by a specific time step (to time level n, the current time level), the composition of the gas mixture at the anode-gas and cathode-gas interfaces is supplied to the porous electrode model as boundary conditions, and a transient version of equations (2.33) to (2.36) is integrated to steady state. Then the mass fluxes across the electrode-gas interfaces are sent back to the flow solver as boundary conditions for the momentum equation and the species mass conservation equation so as to march the governing equations to time level n+1. Meanwhile, the species' enthalpies are evaluated with the gas composition at the electrode-gas interfaces at the n^{th} time level, and the enthalpy fluxes of all species are calculated by multiplying the mass fluxes with the species' enthalpies respectively. The total enthalpy fluxes in (2.44) i.e., $(-\Delta H)_a$ and $(-\Delta H)_c$ are evaluated by summing all the species' enthalpy fluxes. Then the energy equation of the MEA (2.44) is solved, separately from (2.33) to (2.36).

Regarding the coupling between the two solvers, a few issues must be noted. First, since the solutions of the chemistry solver are based on the solution of the flow solver on the n^{th} time level, the coupling between the flow solver and the chemistry solver is explicit; therefore the whole SCFC model is semi-implicit, considering the flow solver is semi-implicit and the chemistry solver is fully-implicit. The explicit coupling may put limitations on the maximum allowable time step for the time integration in

the flow solver. Second, only the steady-state solution of the model is of interest; the intermediate solution doesn't have a clear physical meaning, because the chemistry solver is formulated in a steady-state form and always returns a steady-state solution, regardless of the time-dependent gas compositions at the electrode-gas interfaces. However, the steady-state formulation and solution algorithm of the chemistry solver is advantageous because otherwise the maximum time step would be determined by the length scale in the MEA, which is two to three orders of magnitude smaller than that of the flow solver. Furthermore, a transient formulation of the chemistry solver would possibly incur stiffness in chemical reactions, which would also dramatically slow down the whole computation process.

2.10 Numerical Solution Scheme for the Governing Equations of the MEA

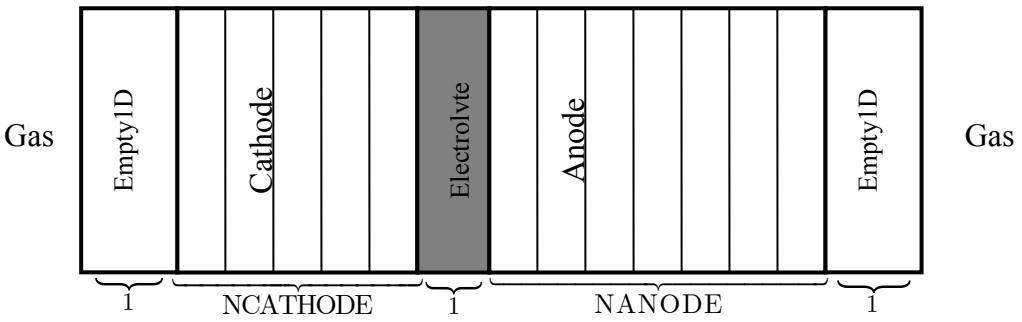

Figure 2-5. Structure of one segment of the MEA and the corresponding discretization

The MEA is divided along its length direction into a number of segments, and each of them is a one-dimensional domain shown in Fig. 2-5. The electrodes are divided into many control volumes, and the height of them can be different. The electrolyte is undivided. Equations (2.33) and (2.34) are discretized on the computational grid of the electrodes, while (2.35) and (2.36) are defined at the

electrode-electrolyte interfaces. These four equations are solved simultaneously by the built-in Newton solver in Cantera.

Cantera handles each electrode and the electrolyte with C++ class Domain1D. The assembly of these Domain1D objects, i.e., the MEA segment, is handled by class Sim1D. In a Sim1D object, the Domain1D objects are classified as bulk domains and connector domains. A bulk domain can be divided by computational grids, like the electrodes, while a connector domain is undividable. The two types of domains must be arranged in an alternating pattern, which is necessary to maintain the bandedness of the Jacobian matrix in the Newton solver. For convenience of the solution process, an Empty1D domain (also a connector domain but a special case of the Domain1D object) is added to each end of the MEA segment (Fig. 2-4). There is only one variable in this domain, and it's always set to zero.

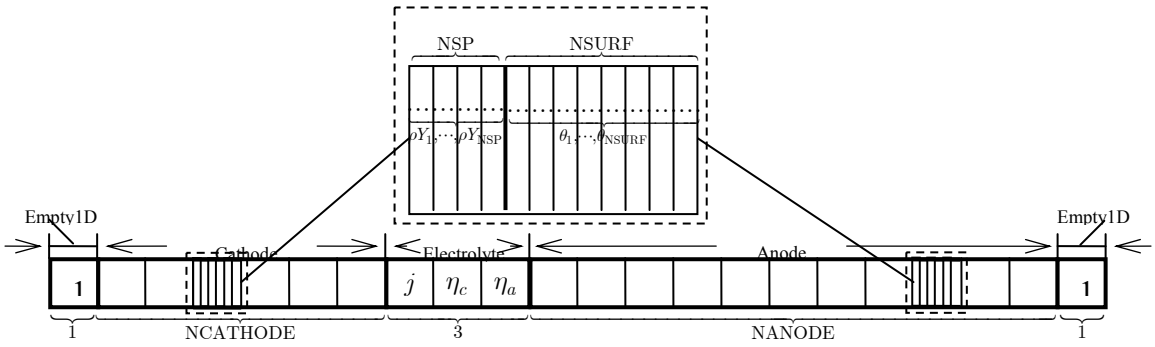

Figure 2-6. Structure of the global solution vector for each segment of the MEA

Correspondingly, the structure of the global solution vector of the Sim1D object is shown in Fig. 2-6. For each control volume in the electrodes, the unknowns are the mass concentrations of all gas-phase species, followed by the surface coverage percentages of all surface-phase species. The number of gas species, NSP, is the same everywhere (i.e., the gas channel and the electrodes), while the number of surface

species, NSURF, depends on the specific heterogeneous reaction mechanism used for the electrode catalyst. As for the electrolyte, there are only three variables defined, including the current density j and the charge-transfer overpotentials η_a and η_c.

Based on the solution procedure discussed above, the model can also solve problems with multi-layer electrodes, each layer with automatic refinement of computational grids. These topics will be discussed in a later chapter.

Chapter 3
Numerical Study of Single-Chamber SOFCs

3.1 Introduction

Compared with experimental studies of SCFC, the numerical modeling approach could study and improve the understanding of important issues in the design and operation of SCFC more systematically, and avoid the time-consuming trial-and-error design-test loop. Furthermore, modeling is particularly useful for exploring realms that are hard (or even impossible) to achieve by existing experimental techniques, such as resolving reactions within the porous electrodes and optimizing important design parameters of the MEA. The insights into the underlying chemical and physical processes obtained in this way are the principal objective of modeling of this type.

The model developed so far is a general numerical framework for stacked SCFCs. In order to use the model to make quantitative predictions to guide experimental design, the uncertainties in the model must be removed by calibration against experimentally measured parameters and performance characteristics of the fuel cell. The calibrated model also has to make predictions and compare with independent measurements to establish its validity. The validated model can then be used to explore different questions in the SCFC system to improve the understanding of fundamental processes and optimize the fuel cell design at different levels. The

discussions in this chapter will shed light on future experimental design and testing of both single MEA and stacks of SCFC.

3.2 Model Calibration and Validation

The general strategy for the calibration process is to fix the parameters that are easier to obtain through direct or indirect experimental measurement first, and then evaluate the hardest ones by fitting the predicted fuel cell performance to measured discharge curves. The following subsections will describe the calibration process step by step.

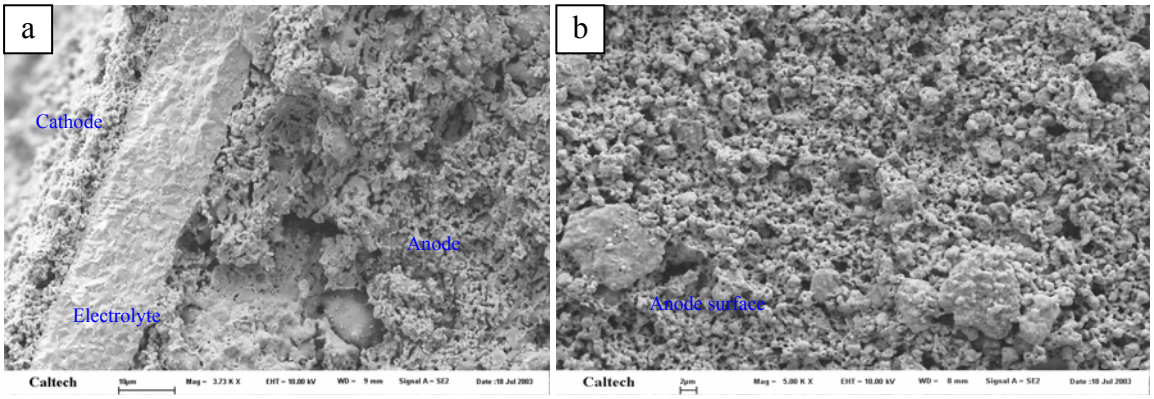

Figure 3-1. SEM image of MEA cross sections. (a) The electrodes and the electrolyte; (b) The anode catalyst surface [22]

3.2.1 Structure Parameters of the MEA

These parameters include the thickness of each layer of the MEA, the conductivities of the electrolyte, and the parameters describing the micro-structure of the electrodes. The thicknesses are measured from the SEM image (Fig. 3-1) of the MEA cross section and the process is very straightforward. Other parameters are discussed as follows.

Specific Surface Area (SSA)

This parameter is the surface area per unit volume of the electrode catalyst and has a dimension of m^{-1} (i.e., m^2/m^3). It is an important indicator of the number of sites available for catalytic reactions to take place over the catalyst surface. For the anode, SSA affects the total reaction rates of the hydrocarbon fuel to produce hydrogen, and for the cathode, it affects the rates of the parasitic combustion of the hydrocarbon fuel and its associated fuel products (e.g., H_2 and CO), thus eventually affecting the oxygen partial pressure at the cathode-electrolyte interface. Therefore SSA is an important parameter for the fuel cell performance.

The SSA of the cathode catalyst $Ba_{0.5}Sr_{0.5}Co_{0.8}Fe_{0.2}O_{3-\delta}$ (BSCF) was measured by Mederos [10] using the BET (Brunauer-Emmett-Teller) method, which is based on the physical adsorption of gas molecules on a solid surface. The value is 1.0582×10^6 m^{-1}.

The SSA of the anode catalyst Ni was measured by Shao [79]. The SSA of the Ni powder after sintering at 1300°C is about 0.1 m^2/g, which corresponds to 7×10^5 m^{-1}.

For Ni anode materials, the SSA is important when the fuel for electrochemistry (e.g., H_2 or CO) has to be generated in-situ through catalytic surface reactions. A higher specific surface area can also increase the length of the triple-phase boundary (TPB), which is important for electrochemical reactions. Furthermore, in materials like BSCF and likely SDC, where the electrocatalysis happens on the surface of the oxide and not at the TPB, having more oxide surface directly increases the amount of

reactive area. Therefore the specific surface area is an important parameter that affects power output.

Electrolyte Conductivities

The model has the capability to simulate fuel cells with either pure ionic conductor (e.g., YSZ) electrolyte or mixed electronic-ionic conductor (MIEC; e.g., SDC) electrolyte. The pure ionic conductor electrolyte only conducts oxygen ions and is mostly used in the conventional dual-chamber SOFCs that operates at 800^{o}C or higher in order for the electrolyte to have enough conductivity. This type of material has been widely studied, and the conductivity data is readily available in literature. The simulation of YSZ cells in this work adopts the conductivity from Ref [56].

The MIEC electrolyte conducts both oxygen ions and electrons. Due to a typically higher ionic conductivity than pure ionic-conducting materials, it is particularly suitable for single-chamber SOFCs despite the undesirable electronic conduction, since these fuel cells must operate at a temperature low enough for the catalysts to maintain some degree of selectivity; this typically limits the temperature to below 700^{o}C, which is significantly lower than that of conventional SOFCs with a YSZ electrolyte. For this reason, SCFCs demonstrated to date have used ceria-based electrolytes, such as SDC. As a result, the total current involves the ionic current and a detrimental electronic current in the reverse direction (2.41).

In order to simulate ceria-electrolyte cells, the ionic and electronic conductivities both need to be measured accurately. These transport properties of the ceria used in

this model have been fully characterized by Lai et al., with the result reported in [78]. The electronic conductivity (2.44) depends on both oxygen partial pressure and temperature, with values $a = 2.42 \times 10^8 \mathrm{K\ \Omega^{-1} cm^{-1} atm^{0.25}}$ and $b = 2.69 \times 10^4$ K, whereas the ionic conductivity (2.40) depends only on temperature, with an exponential term of 1.15×10^5 K Ω^{-1} cm^{-1} and an activation energy of 0.67 ± 0.01 eV [10].

Porosity, Tortuosity, Pore Radius, and Particle Diameter

These four parameters are used by the Dusty Gas Model [57] for calculating the effective diffusion coefficient of the gas-phase species. The effective molecular binary diffusion coefficient in the porous media D_{kl}^e is related to the binary diffusion coefficient D_{kl} by

$$D_{kl}^e = \frac{\phi}{\tau} D_{kl} \tag{3.1}$$

where ϕ is porosity and τ is tortuosity [56]. The (average) pore radius r_p is used to calculate the diffusion coefficient of the Knudsen diffusion, which occurs due to gas-wall collisions and becomes dominant when the mean free path of the molecular species is much larger than the pore parameters. The effective Knudsen diffusion coefficient can be expressed as [56]

$$D_{k,\mathrm{Kn}}^e = \frac{4}{3} \frac{\phi}{\tau} r_p \sqrt{\frac{8RT}{\pi W_k}} \ . \tag{3.2}$$

The particle diameter d_p is not used unless the porous electrode is assumed to be formed by closely packed spherical particles with diameter d_p. In this case, the permeability of the porous media can be expressed by

$$B = \frac{\phi^3 d_p^2}{72\tau (1-\phi)^2} \ . \tag{3.3}$$

For the study in this thesis, the values of ϕ, r_p, and d_p are estimated from the SEM images of the MEA cross section (Fig. 3-1). The tortuosity is hard to measure or estimate, and so the typical value of 3.6 for porous media is taken from [56].

3.2.2 Parameters for Electrochemistry

In this thesis, electrochemistry refers to the oxidation of hydrogen by oxygen ion at the anode-electrolyte interface and the reduction of oxygen at the cathode-electrolyte interface as a result of charge transfer. The fuel cell electrochemistry is simulated by the Butler-Volmer equation (2.36), in which the unknowns are the exchange current density i_0, the asymmetric factors (also called transfer coefficients) for anodic reaction and cathodic reaction α_a and α_c, and the activation overpotential η_{act} for the charge transfer process. The overpotential is one of the unknowns that the model is going to solve for, and all other parameters were measured directly or indirectly from experiment.

Exchange Current Density

The exchange current can be viewed as a kind of "idle current" for charge exchange across the electrode-electrolyte interface, and is a measure of any system's ability to deliver a net current without a significant energy loss due to activation [80]. A system with a high exchange current density has fast kinetics and can respond rapidly to a potential change.

The exchange current density i_0 generally depends on both temperature and the local composition at the electrode-electrolyte interface, and the exchange current densities used for the simulation of SCFC in this work were supplied by Haile's group [10] by measuring the interfacial area specific resistance (ASR) for an electrode | electrolyte | electrode cell (two-electrode) configuration. This quantity is related to the terms of the Butler-Volmer equation according to

$$\mathrm{ASR}^{-1} = \left.\frac{di}{d\eta}\right|_{\eta=0} = i_0\,(\alpha_c + \alpha_a)\frac{F}{RT} \tag{3.4}$$

and this yields

$$i_0 = \frac{RT \cdot \mathrm{ASR}^{-1}}{(\alpha_c + \alpha_a) \cdot F}\ . \tag{3.5}$$

Note that in this formulation the number of electrons transferred during the reaction (often denoted as n) is implicitly included in the definition of the asymmetry factors, and that for charge transfer processes that include more than one step, even without the inclusion of n, the sum of the asymmetric factors can be greater than one [56]. Equation (3.5) shows that measurement of the interfacial ASR does not completely define the exchange current density. However, the ASR data do yield i_0 within a constant factor, the sum of the asymmetry parameters. These terms were used as fitting parameters in simulating the fuel cell polarization data.

In specific, for the typical SCFC configuration Ni-SDC | SDC | BSCF-SDC in this work, the interfacial ASR for the Ni-SDC | SDC interface was taken from the experimental data of Lai and Haile [78], measured from Pt | SDC | Pt symmetric cells under reducing conditions. They proposed that ceria itself is directly active for the electrochemical oxidation of hydrogen and the reaction is limited by the rate of

removal of electrons from the reaction sites, so that the nature of the metal species should not affect electrocatalysis rates. The ASR was found to be dependent on oxygen partial pressure as well as temperature, according to

$$(\mathrm{ASR})^{-1} = (\mathrm{ASR}_0)^{-1} \exp\left(\frac{-E_{\mathrm{act}}^{\mathrm{anode}}}{k_b T}\right) P_{O_2}^{-1/4} \tag{3.6}$$

with ASR_0 = 8.13 × 10^{-9} Ωcm^{2}atm$^{-¼}$ and $E_{\mathrm{act}}^{\mathrm{anode}}$ = 2.67 eV. The oxygen partial pressure at the anode electrolyte interface is calculated from the equilibrium between H_2, O_2, and H_2O, where the hydrogen and water partial pressures are obtained from the porous electrode submodel.

The interfacial ASR for the BSCF-SDC | SDC interface was obtained from impedance measurements of electrolyte-supported BSCF-SDC | SDC | BSCF-SDC symmetric cells under oxidizing conditions. Impedance data were collected at temperatures of 450 to 725°C, and under oxygen partial pressures of 0.01 to 1 atm. Like the anode, the cathode interfacial resistance was found to depend on both temperature and oxygen partial pressure p_{O2}. In this case, however, the exponent in the p_{O2} dependence also varied with temperature, yielding an overall expression

$$(\mathrm{ASR})^{-1} = (\mathrm{ASR}_0)^{-1} \exp\left(\frac{-E_{\mathrm{act}}^{\mathrm{cathode}}}{k_b T}\right) P_{O_2}^{\gamma(T)} \tag{3.7}$$

with $(ASR_0)^{-1}$ = 1.35 × 10^8 Ω^{-1}cm^{-2}atm$^{-\gamma}$ and $E_{act}^{cathode}$ = 1.16 eV, and γ(T) being well-fit according to $\gamma(T) = \gamma_0 + \gamma_1 \exp(T/T_\gamma)$, where γ_0 = 0.35, γ_1 = 3.43×10^{-6} and T_γ = 91.3 K.

Asymmetric Factors

The asymmetric factor (or charge-transfer coefficient) is a measure of the symmetry of the energy barrier of the charge transfer process. In a redox reaction, the

energy barrier is marked by the intersection of the standard free energy curves of the oxidant and reductant. The intersection is symmetrical if the factor is 0.5. In the great majority of experiments, the factor appears to be constant, and in most systems it turns out to lie between 0.3 and 0.7 [80].

For the fuel cell electrochemistry in this work, the asymmetric factors are very difficult to measure directly by experiment. Therefore the values of these factors are determined by fitting the model-predicted electrical performance to experimentally measured current-voltage (I-V) curves.

The fitting process works by picking a few (usually just one) points on the I-V curve near the peak power density location and setting the load potential to be the same as in the experiment each time. Since in the Butler-Volmer equation, it is the positive exponential term that has a predominant influence on the current density, the anodic factor is adjusted on both the anode side and cathode side, so that the simulated current density matches the experimental value.

The experimental data-set obtained at a furnace temperature 600°C (Fig. 3-2a) was used to calibrate the model, using an isothermal simulation in which the cell temperature was fixed at the measured value of 743°C. Because the heat transfer aspects are not included in the isothermal simulation, values for the emissivity and thermal conductivity were not necessary at this stage. The identical set of parameters were then used to simulate the polarization curves corresponding to the other two sets of conditions, again, isothermally, using the actual (measured) cell temperatures (Fig. 3-2b and c). Through the calibration process, the anodic parameter of 1.0 and 0.6 are

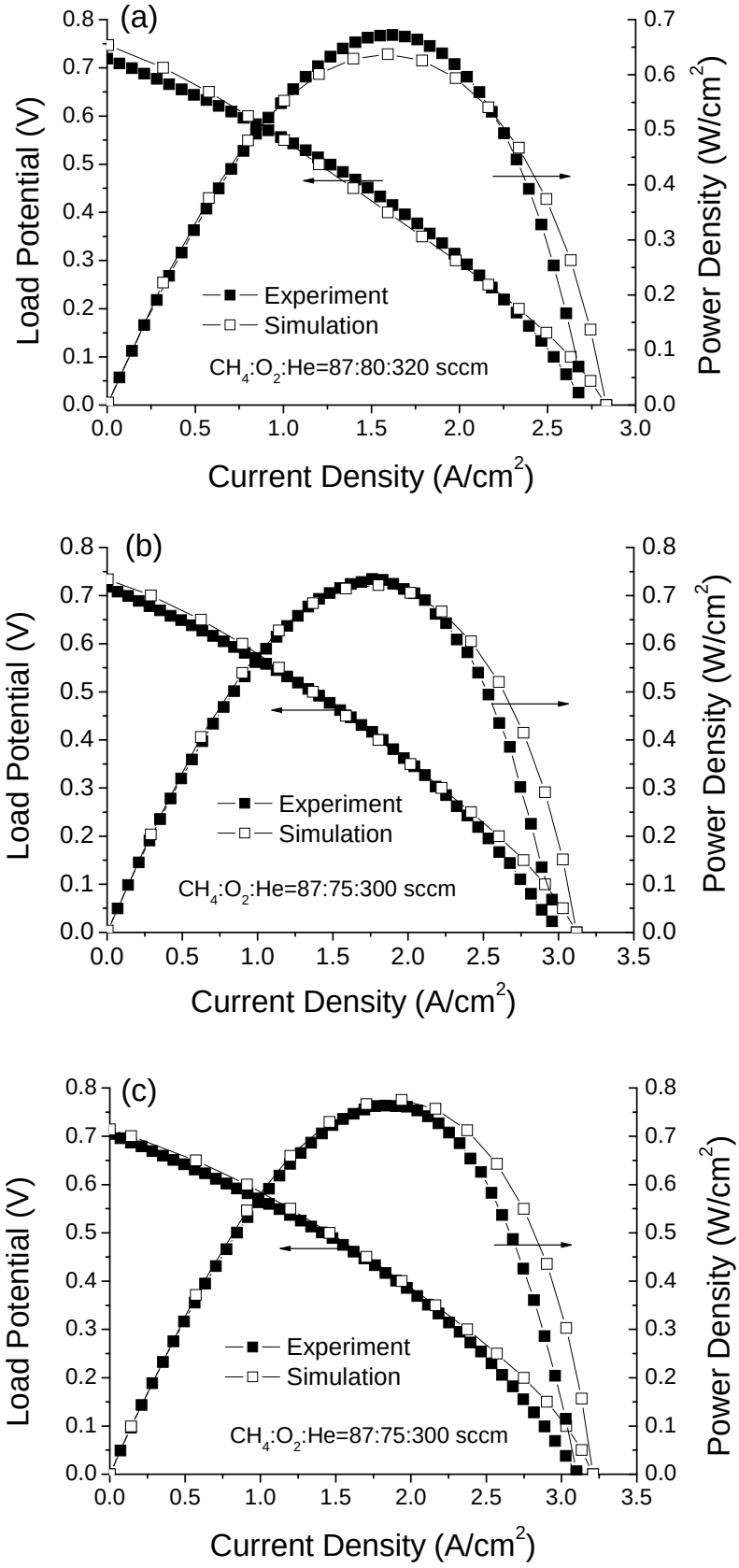

Figure 3-2. Simulated vs. experimental polarization curves for CH_4, O_2 and He flow rates indicated. (a) T_{furn} = 600°C, T_{cell} = 743°C; (b) T_{furn} = 625°C, T_{cell} = 763°C; and (c) T_{furn} = 650°C, T_{cell} = 786°C. Simulations performed isothermally using measured cell temperatures

obtained for the electrochemistry on the anode and cathode side respectively. As Fig. 3-2 indicates, there is excellent agreement between the experimental data and the simulations, validating the overall approach and giving confidence in the accuracy of the model for performance predictions.

3.2.3 Emissivity and Thermal Conductivity

For single-chamber configurations of the SOFC, the cell temperature can be 100-200^{o}C beyond the furnace temperature [19, 20, 24] due to the exothermic reactions within the anode, so that radiation heat transfer becomes important. However, the two parameters that determine the (1-D) temperature distribution in the MEA, emissivity and thermal conductivity, are unavailable from the literature and thus are also obtained by fitting the temperature rise and streamwise temperature gradient across

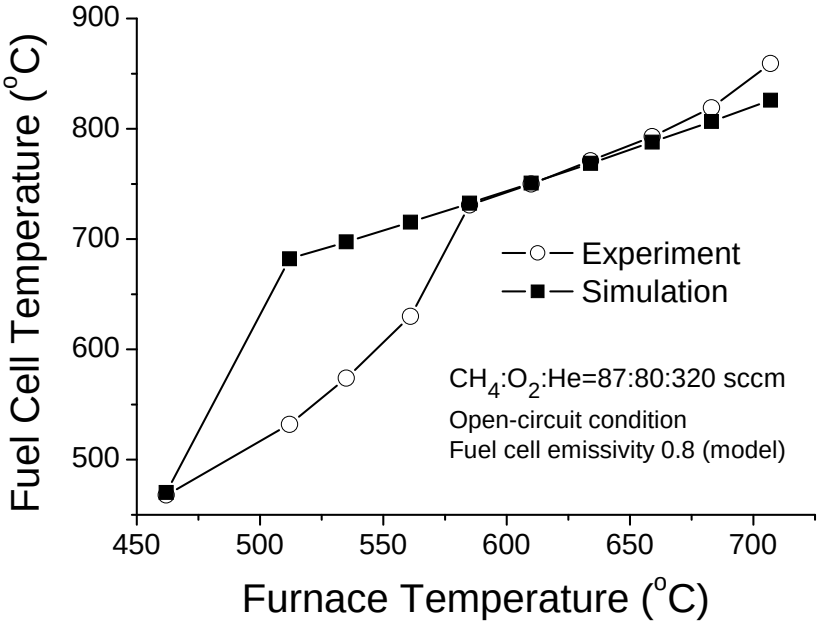

Figure 3-3. Simulated and measured cell temperatures for the operational conditions indicated

the cell to the experimental data obtained for a selected fuel cell experiment. From the fit at this single condition, the temperature rises observed were well-simulated (Fig. 3-

3), indicating the appropriateness of the derived material properties (emissivity = 0.8 and thermal conductivity of 30 W/m/K). Although in reality the two parameters may well be functions of location and depend on material, it is assumed for simplicity that they are both constant all over the MEA.

Table 3-1. Parameters for a Ni-SDC|SDC|BSCF-SDC MEA obtained through model calibration

Parameters	Value	Units
Anode: Ni + SDC		
Thickness	700	μm
Porosity	0.5	-
Tortuosity	3.6	-
Average pore radius	0.2	μm
Average particle diameter	1.0	μm
Specific catalyst area	7×10^5	m^2/m^3
α_a*	1.0	-
α_c*	0.4	-
Cathode: BSCF+SDC		
Thickness	10	μm
Porosity	0.3	-
Tortuosity	1.0	μm
Average pore radius	0.2	μm
Average particle diameter	1.0	μm
Specific catalyst area	1.0582×10^6	m^2/m^3
α_a*	0.6	-
α_c*	0.4	-
Electrolyte: SDC		
Ionic conductivity: $\sigma_i = \sigma_0 T^{-1} \exp(-E_a / R / T)$		
Electronic conductivity: $\sigma_e = k_e T^{-1} \exp(-E_e / R / T) p_{O_2}^{-1/4}$		
Thickness	15	μm
σ_0	3.87×10^7	S·K/m
E_a	82.3	kJ/mol
k_e	2.418×10^{10}	$S \cdot K \cdot atm^{0.25}/m$
E_e	223.3	kJ/mol
MEA		
Emissivity *	0.8	-
Heat conductivity *	18.0	W/m/K

3.2.4 Remarks on the Calibration and Verification Procedure

Model calibration and verification based on experimental data laid a solid groundwork for the quantitative prediction of the performances of SCFC. Moreover, since the numerical model is a general framework for simulating fuel cells with a thin MEA and a 2-D gas flow geometry, the calibration procedure can be applied to the simulation of other types of fuel cells, such as the conventional dual-chamber SOFC and even fuel cells with proton-conducting electrolytes. Different fuel cell systems should have different parameter sets, and the calibration process should be carried out first whenever a quantitative prediction by the model is needed. This will be discussed in chapters that follow.

The parameters obtained by the fitting procedure are based on certain simplification assumptions and thus may not carry a well-defined physical meaning. The criteria for judging if the parameters are acceptable is the agreement between predicted and measured performance, such as power output and temperature rise, and the "agreement" is confirmed if the relative difference between model prediction and experiment measurement is below a certain threshold. By this definition, the acceptable parameters for predicting the fuel cell performance exist in a narrow parameter space rather than taking unique numerical values. Also, for a 2-D model that simulates a 3-D system in reality, the predicted trends are more meaningful than the precise numerical values for a better understanding of the fundamental questions that govern the fuel cell operation, and therefore the numerical values of the

parameters, as long as they fall in a reasonable range (e.g., by their definition) and lead to good predictions, will not be the emphasis of further discussion.

The parameters obtained through model calibration are listed in Table 3-1. Parameters marked by "*" were obtained by the fitting process. Predicted results based on these parameters have been shown in Fig. 3-2.

3.3 Numerical Study of SCFC Performance

Based on the quantitative calibration and good agreement between prediction and experiment measurements discussed previously, the following discussions will focus on utilizing the model to study important issues in SCFC design and operation. With the detailed physical model, it is possible to examine the effects of different parameters on the overall SCFC performance in a way that is nearly impossible from experiment alone, since effects that cannot be separated in reality can be turned on or off in a model. Topics such as the optimum fuel-to-oxygen ratio, the management of the flow geometry, and the optimization of some important design parameters will be discussed.

3.3.1 Fuel-to-Oxygen Ratio

A significant question of interest for SCFC operation is the optimal fuel-to-oxygen ratio. The working principles of SCFC (discussed in the first chapter) determine that the maximum power density should occur under a fuel-rich condition, meaning that there is insufficient oxygen present for complete combustion of the fuel

(i.e., f/o ratio is above combustion stoichiometry). This is also verified by several experimental groups [18, 19, 21, 81]. Due to the mixing of the fuel and oxygen, it is understandable that there exists such a ratio that the power output of the fuel cell maximizes, since in the extremes of either insufficient fuel or oxygen, at least one of the electrodes will run short on one reactant for electrochemistry, so that the power output suffers. However, the mechanism responsible for the optimum f/o ratio remains unclear and needs in-depth discussions.

Table 3-2. Parameters for an SCFC MEA Structure with YSZ electrolyte

Parameters	Value	Units
Anode		
Thickness	700	μm
Porosity	0.35	-
Tortuosity	3.5	-
Average pore radius	0.25	μm
Average particle diameter	2.5	μm
Specific catalyst area	7.0×10^{5}	m^2/m^3
α_a	1.5	-
α_c	0.5	-
Cathode		
Thickness	10	μm
Porosity	0.35	-
Tortuosity	3.5	-
Average pore radius	0.25	μm
Average particle diameter	2.5	μm
Specific catalyst area †	1.06×10^{6}	m^2/m^3
α_a	0.5	-
α_c	0.5	-
Electrolyte: $\sigma_i = \sigma_0 T^{-1} \exp(-E_a / R / T)$		
Thickness	15	μm
σ_0	3.6×10^{7}	S·K /m
E_a	80.0	kJ/mol
MEA		
Emissivity	0.8	-
Heat conductivity	18.0	W/m/K

A YSZ cell is numerically simulated to study the optimum fuel-to-oxygen ratio. Since the optimal ratio is defined by the maximum power density, it is better to explore the question with YSZ-based cells, for ceria-based SCFC involve the reverse electrical current that sensitively depends on the cell operating conditions and will make the discussion much more complicated. The simulation geometry is the same as described in Fig. 2-1 (see Chapter 2). The channel is taken to be 15 mm high and 135 mm long, and a uniform computational mesh of 21 cells (along the height) by 75 cells (along the length) is used for the channel flow. A single MEA of length 12.6 mm and thickness 0.73 mm is placed horizontally in the channel, centered vertically and with the leading edge located at 25.2 mm from the entrance to the channel. The MEA is divided into 7 segments (cells) of uniform lengths along the streamwise direction. The anode and cathode are divided into 10 and 8 control volumes in the y direction respectively. The electrolyte is not discretized.

The molar flow rate of methane at the inlet is held fixed at 21.97 mol/m^2/s, and the molar ratio of oxygen to helium is fixed at 1 to 4. For methane, stoichiometric combustion occurs for a CH_4/O_2 (volumetric) ratio of 0.5. In the simulations discussed below, this ratio was varied from 0.5 to 5.0. A small amount of hydrogen and water is assumed to be present at the inlet at the beginning of the temporal integration, so that the Nernst potential E^0 in (2.37) is well-defined at the inlet. The feed rates of the two gases are reset to zero during the simulation when they are generated by the MEA. The temperature is held at 750^{o}C and the load potential is fixed at 0.5 V, the voltage

corresponding to the maximum power density for all cases. The total flow rate is fixed to eliminate the influence of velocity.

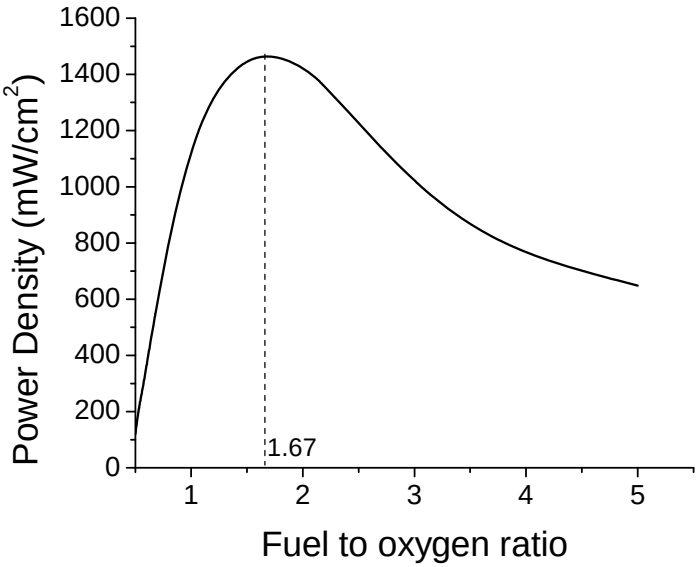

Figure 3-4. Simulated power density versus fuel-to-oxygen ratio at 750^{o}C and load potential of 0.5 V; YSZ electrolyte

The parameters used to describe the MEA structure are listed in Table 3-2. The specific surface area of the cathode, the thicknesses of electrodes and the electrolyte are obtained through the calibration process. All other parameters are taken from [56].

The power density is plotted versus the CH_4/O_2 ratio in Fig. 3-4, and the optimum ratio (for maximum power) is found to be 1.67. While it is useful to know the precise value of the optimum CH_4/O_2 ratio, it is more instructive to understand the factors responsible for this result. To understand the dependence of power density on fuel-to-oxygen ratio, the partial pressures of all the gas-phase species (directly obtained from the solution of the porous electrode transport model) at the anode-electrolyte interface are first plotted in Fig. 3-5, together with the oxygen partial pressure at the cathode-

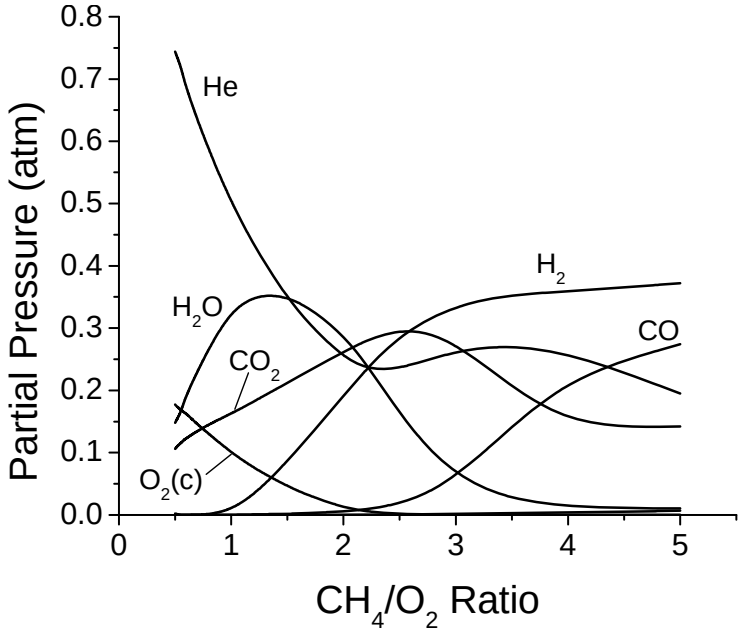

Figure 3-5. Partial pressure of gas species at the anode-electrolyte interface (plus O_2 at cathode-electrolyte interface) at the middle (along *x* direction) of the fuel cell; T=750^{o}C; E_{load} = 0.5 V

electrolyte interface at the middle (in the streamwise direction) of the cell versus the CH_4/O_2 ratio. When the ratio is close to stoichiometric (0.5), very little hydrogen is generated in the anode because most methane that penetrates into the anode is fully catalytically oxidized. On the other hand, when the ratio is over 2.0, although abundant hydrogen is generated in the anode (and diffuses to the anode-electrolyte interface), the oxygen concentration on the cathode side is reduced, due to both the low oxygen flow rate and the increased concentration of H_2 and CO transported from the anode side, which consume oxygen through their full oxidation (in addition to the full oxidation of methane) over the cathode catalyst surface. Since in this model it is hydrogen that is the electrochemically active fuel species, and in addition oxygen is required for the cathode reaction to take place, both must be present (in the anode and cathode, respectively) for a current to flow; the optimal fuel-to-oxygen ratio is the one

that simultaneously results in adequate hydrogen at the anode and oxygen at the cathode.

Due to the coupling of many physical and chemical processes, the optimum fuel-to-oxygen ratio cannot be determined by simply assuming either full oxidation of the fuel (for maximum enthalpy change) or partial oxidation of the fuel (for the highest yield of H_2). Since it is the concentrations of H_2 and O_2 at the electrode-electrolyte interfaces that ultimately determines the fuel cell power, the optimum CH_4/O_2 ratio (defined by the flow rates of the gas feed at peak power condition) has to be determined by considering all possible processes that influence the conversion of fuel to H_2 in the anode, the transport of contributing gas phase species in both the electrodes and the gas channel, and electrochemistry at electrode-electrolyte interfaces. The parameters describing these processes include, but may not be limited to temperature, electrode catalyst activity, electrode microstructure, flow geometry and exchange current density. Flow geometry (including MEA orientation and flow field dimensions) is probably the most sensitive factor for the optimum ratio. It influences local power density along the MEA (and thus the optimum CH_4/O_2 ratio) because convection and transport determines the distribution of reactants around the MEA. Since the distribution of power density depends on location along the MEA, the optimum ratio of 1.67 can be interpreted as a value at which the point-wise average power density of the fuel cell is the highest. However, not all locations of the fuel cell achieve their maximum power simultaneously. Fig. 3-6 shows the contour plot of the local current density versus CH_4/O_2 ratio and location on the MEA. The optimum

ratio is found to decrease with distance from the leading edge because according to the simulation results, oxygen is consumed faster (by moles) than methane, due to the coexistence of partial and full oxidation of methane in the anode; thus the gas mixture becomes increasingly fuel-rich as it flows along the MEA. Therefore, at a downstream location, a higher oxygen flow rate is needed at the inlet than in an upstream location, so that the optimum fuel-to-oxygen ratio decreases along the flow direction.

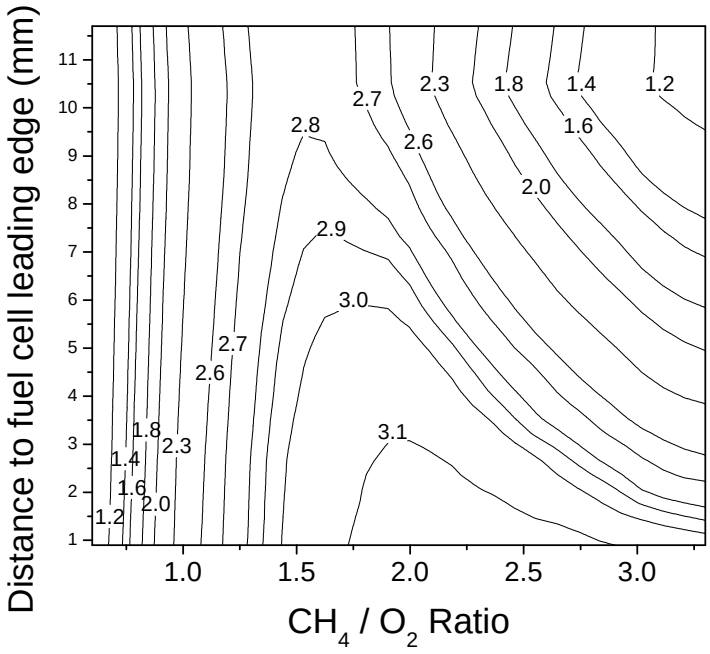

Figure 3-6. Contour plot of local current density (A/cm^2) vs. CH_4/O_2 ratio and location on the MEA at 750°C and load potential of 0.5 V

The optimum ratio and MEA performance can be enhanced by reorienting the MEA without changing any other parameter. To achieve this, more understanding about the coupling between different parts of the MEA through the external gas flow is needed. In the geometry with the MEA parallel to the channel axis, the upstream cells of the MEA have a strong influence on the downstream ones, but not vice versa. This is verified by Fig. 3-7, which shows for different MEA lengths (with the leading

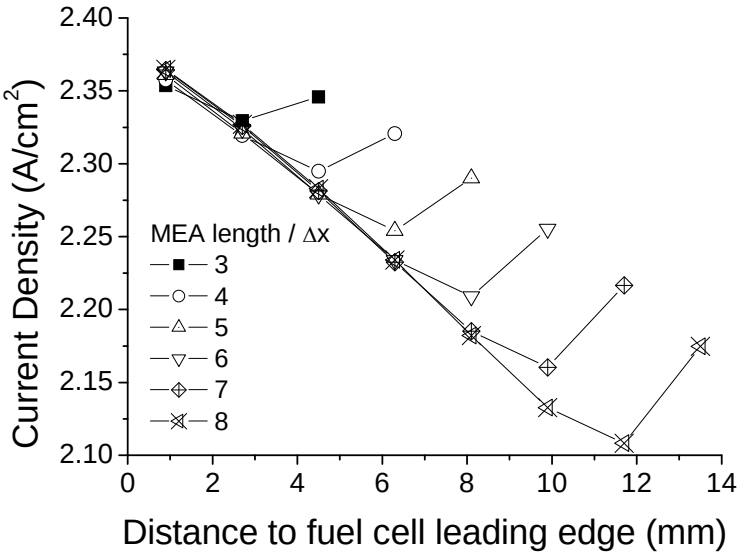

Figure 3-7. Current density along the MEA for different MEA lengths; Flow rate CH_4:O_2:He=1:1:4

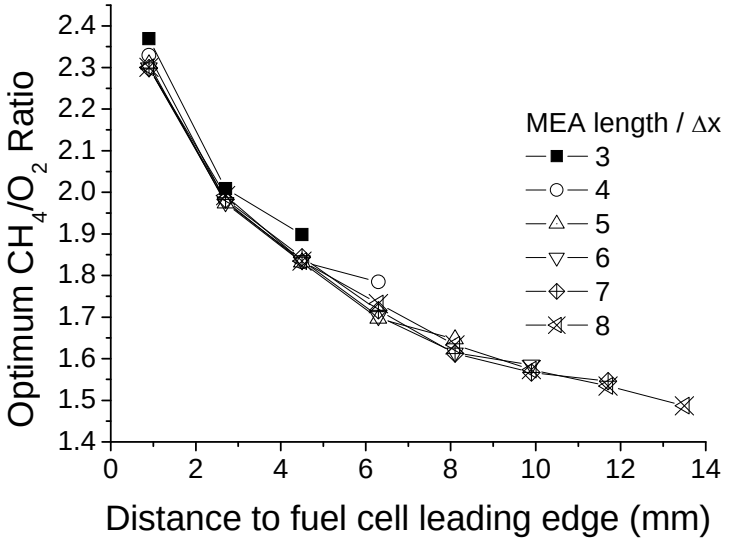

Figure 3-8. Optimum fuel-to-oxygen ratio of each cell along the MEA for different MEA lengths; Δx: x-dimension of one computation grid

edge fixed), the current density distribution along the MEA at flow rates CH_4:O_2:He=1:1:4. Except for the last two cells of each MEA, the power density at other locations fall almost along the same curve, indicating that flow convection downstream is much stronger than backward diffusion. The current density of the last two cells of each MEA is elevated because the unconsumed methane and oxygen that bypass the MEA on both sides mix at the trailing edge. For the same reason, the

optimum CH_4/O_2 ratio of each cell along the MEA shows a similar trend in Fig. 3-8. For a better understanding of the one-way influence, the two-dimensional distribution (mole fractions) of gas phase species in the gas chamber is shown in Fig. 3-9. From the figures, it can be inferred that because of the depletion of oxygen by upstream cells, flow geometries that improve the oxygen distribution over the MEA surface could have a higher optimum ratio and a better electrical performance. In the discussion that immediately follows, it will be demonstrated that reorienting the MEA could improve the fuel cell performance. Here, a similar effect can be shown for the optimum ratio. When the MEA is oriented such that the cathode is facing the fresh gas feed, the optimum ratio would increase to 2.5.

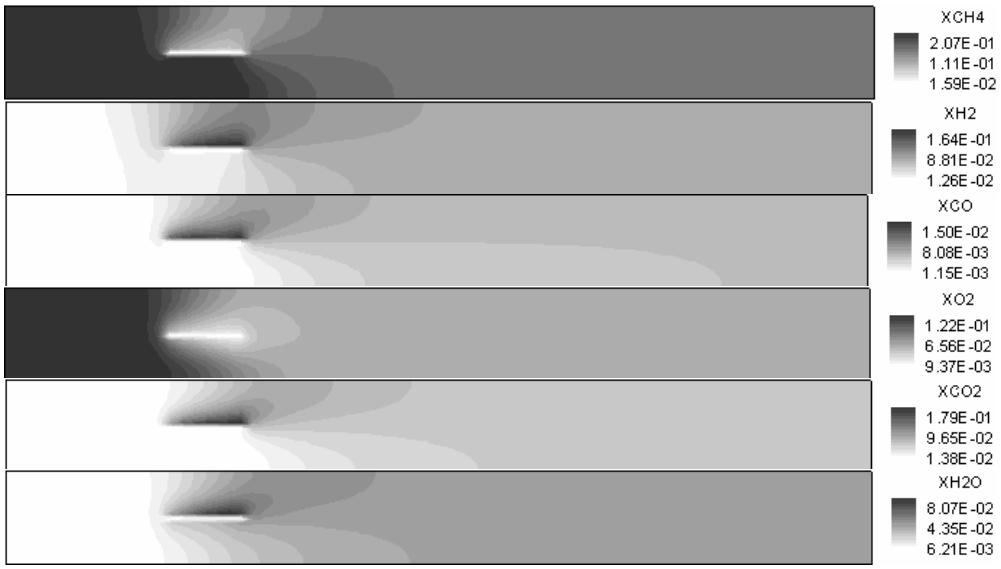

Figure 3-9. Two-dimensional distribution of gas phase components in the gas chamber at opt. fuel-to-oxygen ratio

Meanwhile, temperature and electrochemistry will influence the rates and equilibrium of the catalytic reactions, and so will influence the optimum ratio as well. Computation results show that in the range of 650 to 750^{o}C, the ratio decreases monotonically with temperature. The exchange current density of the anode has little

influence, but that of the cathode could increase this ratio by 35% (to 2.2) when it is lowered by 2 orders of magnitude, indicating that the electrochemical properties of the cathode material might be a more important consideration in cell design. Furthermore, the catalytic activity and structural parameters of the electrodes (e.g., thickness, porosity, and pore size) jointly dictate the distribution of reactants and products within the electrodes, and thus eventually the concentration of H_2 at the anode-electrolyte interface and O_2 at the cathode-electrolyte interface. So these factors are also expected to be partly responsible.

3.3.2 Flow Geometry

As discussed in the previous section, flow geometry determines the distribution of gas-phase species along the MEA surface and thus sensitively influences the fuel cell performance, making it one of the top priorities to consider in SCFC system design. This section discusses the effect of different flow geometries (i.e., the deployment of MEA) in the gas channel for both single and multiple MEAs.

Orientation of Single MEA

Unlike dual-chamber SOFCs, experimental studies showed that the performance of single-chamber SOFCs sensitively depends on flow geometry. The simplest case is that with all other conditions the same, different orientations of the fuel cell could result in different current-voltage characteristics. Stefan et al. [23] tested four different SCFC flow geometries in a mixture of propane and air. In their study, a

single MEA was placed either parallel or perpendicular to the flow direction. They showed that for the two perpendicular geometries, the one with the cathode exposed to the fresh gas feed had a better performance in terms of power density, open circuit voltage and short circuit current. To study this effect, the influence of the MEA orientation on power output is examined. In specific, the MEA is perpendicular to the gas flow direction, with modes 1 and 2 defined in Fig. 3-10 as the cathode and anode respectively exposed to the fresh gas mixture. The diameter of the MEA is reduced to 5.29 mm. An SDC-electrolyte cell is used with Ni anode and BSCF-SDC cathode. The simulation is based on parameters listed in Table 3-1. I-V polarization curves are computed with flow rates of CH_4:O_2:He=87:75:300 sccm and an isothermal temperature 750^{o}C.

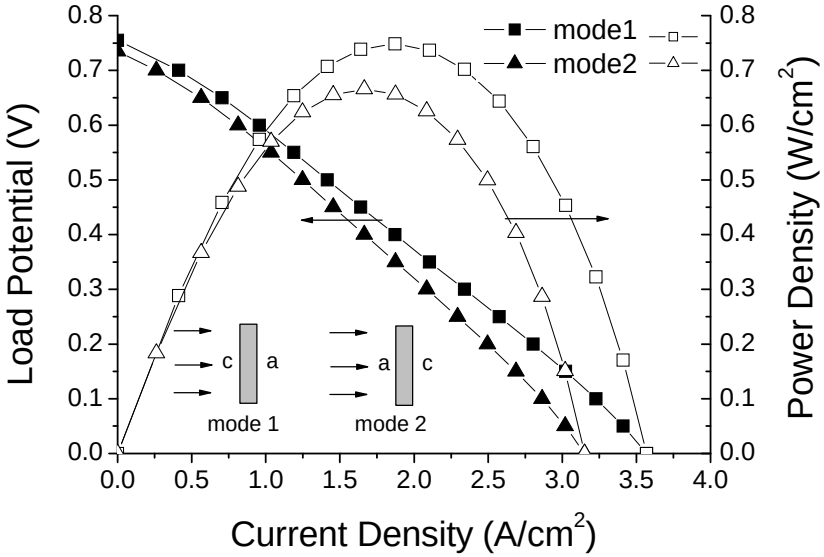

Figure 3-10. Comparison of fuel cell polarization curves for cells placed in different orientations; a: anode, c: cathode

As shown in Fig. 3-10, the performance of the fuel cell with the two geometries has the same trend as in literature. The peak power density and short circuit current of mode 1 are both substantially (12% and 13% respectively) greater than that of mode 2.

The open circuit voltage of mode 1 is 0.755 V, slightly higher than 0.735 V of mode 2, as well. An investigation of the partial pressures of gas-phase species within the electrodes shows that the improvement is due to the higher oxygen partial pressure at the cathode-electrolyte interface. Specifically, the interfacial oxygen pressure of mode 1 is twice that of mode 2. The latter is lower not only because part of the oxygen is consumed by the anode prior to its arrival at the cathode, but also because the partial oxidation products (H_2 and CO) generated by the anode are transported in the gas phase (via both convection and diffusion) to the cathode. There, they consume additional oxygen through their full oxidation over the cathode catalyst surface. Overall, it is apparent that enhanced performance can be obtained by optimizing flow geometry, even in the absence of modifications to the fuel cell component materials or dimensions.

However, compared with the geometry in which the fuel cell is parallel to the channel axis, the total power output of the perpendicular configurations may not be higher because the width (or diameter) of the fuel cell is limited by the channel height (or diameter). In order to reduce the upstream gas-supply pressure and allow for reasonable gas flow speed past the fuel cell, the fuel cell edges need to be kept away from the channel walls by a reasonable distance. By comparison, the parallel case has less limitation on the fuel cell width (diameter), especially if the shape of the fuel cell is non-circular, and thus can still generate a high total power output.

Interaction between Two MEAs

Fuel cells are usually used in stacks to increase the total power output because the voltage of a single cell is too low (usually 0.7 to 0.8V under operating condition [1]). Therefore, an investigation of the interaction between two MEAs is more helpful for SCFC system design. In this section, the configuration with two identical MEAs aligned with the axis of the flow channel is discussed. The distance between them is the same as the length of the MEA. The channel height is 15.875 mm and the length is 9 times the height. The MEA leading edge is located at 26.7 mm from the channel inlet, and the incoming gas composition is CH_4:O_2:He = 174:150:600 sccm. The electrolyte is SDC, and simulation parameters are listed in Table 3-1. Temperature is 700^{o}C isothermal, and load potential is fixed at 0.4 V for maximum power output.

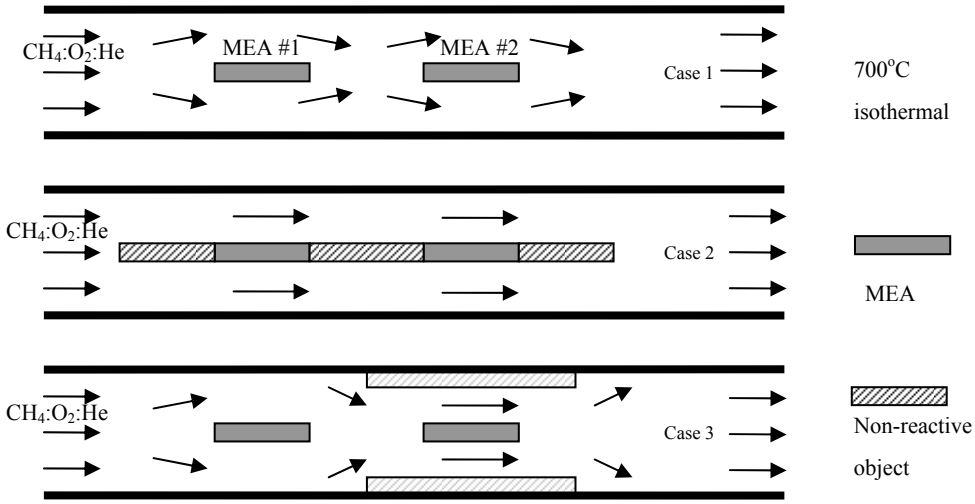

Figure 3-11. Flow geometries for an upstream and a downstream MEA; case 1: base case; case 2: with inert blocks; case 3: with a narrower channel around the 2nd MEA

For this configuration, three cases are compared (Fig. 3-11), with case 1 being the prototype for comparison by the other two. In the first case, the power densities of MEA #1 and 2 are 577 and 533 mW/cm^2, respectively. The second MEA has a lower

value because of the one-way influence of the upstream MEA, similar to what has been discussed above (Fig. 3-7, 3-8 and 3-9). However, the gap between the two MEAs makes it highly possible for the products (e.g., syngas) from the anode of the first MEA to diffuse to the cathode of both the first and the second MEAs to consume more oxygen. For the second MEA in particular, this additional consumption of oxygen could further affect the power output adversely in addition to the depletion of methane and oxygen on its anode side by the upstream MEA.

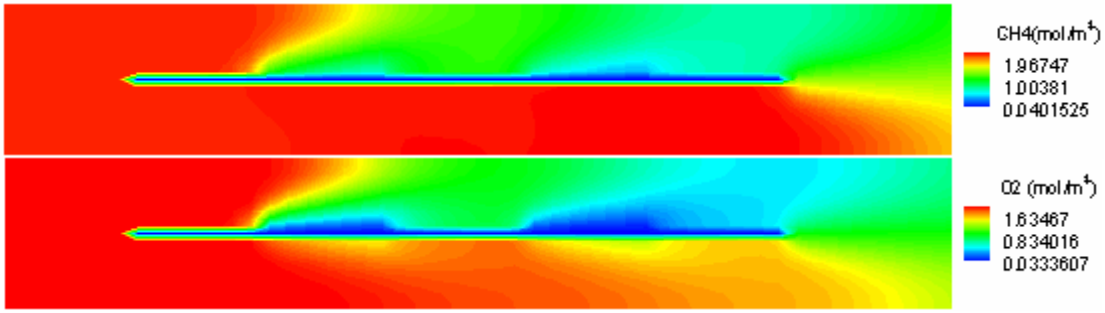

Figure 3-12. Molar concentration of CH_4 and O_2 in the gas channel for case 2

As the first attempt to improve the performance of both MEAs, case 2 blocks the diffusion passage from the anode to the cathode by adding three non-reactive plates with the same dimension as the MEAs. Compared with case 1, this case results in an identical performance for the first MEA and a very small (0.9%) improvement for the second MEA (538 mW/cm^2). The modeling results about gas concentrations in the channel and in the electrodes indicate that that the blocks work both ways. That is, although the harmful syngas diffusion from the anode to cathode is prevented, the beneficial diffusion of methane and oxygen that bypasses the cathode of the first MEA to the anode of the second MEA is also blocked. As shown in Fig. 3-12, there is still much more CH_4 and O_2 left on the cathode side compared with the anode side

(especially the second MEA). By the discussion of the f/o ratio, it is easy to understand that the depletion of these two reactants by the anode of the first MEA significantly overshadows the second one, and thus a replenishment of them for the anode of the second MEA from the cathode side of the first MEA could improve the production of hydrogen and thus the performance of the second cell.

Based on this analysis, an alternative geometry is discussed in case 3, in which the second MEA is placed in a narrower channel, and as a result its power output is effectively improved by 2.4% to 546 mW/cm^2. From the perspective of the flow field, the maximum flow speed over the second MEA increases from ~ 44 cm/sec to ~ 60 cm/sec after two non-reactive blocks of thickness 2.27 mm are attached to the channel walls, and the higher flow speed along the MEA is helpful to alleviate the depletion effect by delivering more reactants to the downstream portion of the same MEA. Meanwhile, the narrower channel makes the diffusion path of gas-phase species shorter on either side of the second MEA, which is beneficial to the whole MEA too. In addition, because the diffusion block between the two MEAs is taken away, the remaining CH_4 and O_2 from the lower portion of the channel can easily diffuse to the

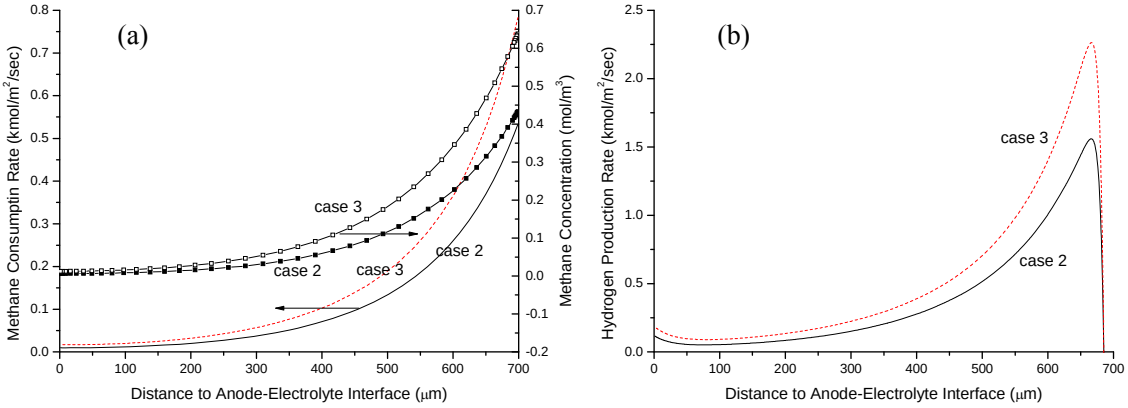

Figure 3-13. Reaction rates of methane and hydrogen within the anode of the second MEA for case 2 and case 3. (a) methane consumption rate; (b) hydrogen production rate

anode side of the second MEA, which results in a higher concentration of methane and higher production rate of hydrogen in the anode of the second MEA (Fig. 3-13).

3.3.3 Anode Thickness

A key fuel cell parameter amenable to variation (and not yet systematically studied in the experimental literature) is the anode thickness. Because the anode plays such a critical role in SCFC operation it can be anticipated that fuel cell power output would be sensitive to the anode dimensions. Fig. 3-14 shows the power density as a function of anode thickness at a fixed load potential of 0.4 V (which approximately corresponds to the voltage at peak power). The gas flow rate is CH_4:O_2:He=87:75:300 sccm. Because the anode dimensions will influence the heat and cell temperature rise, the simulation was performed non-isothermally with a furnace temperature of 600^{o}C. The actual (computed) cell temperature is also shown in the figure.

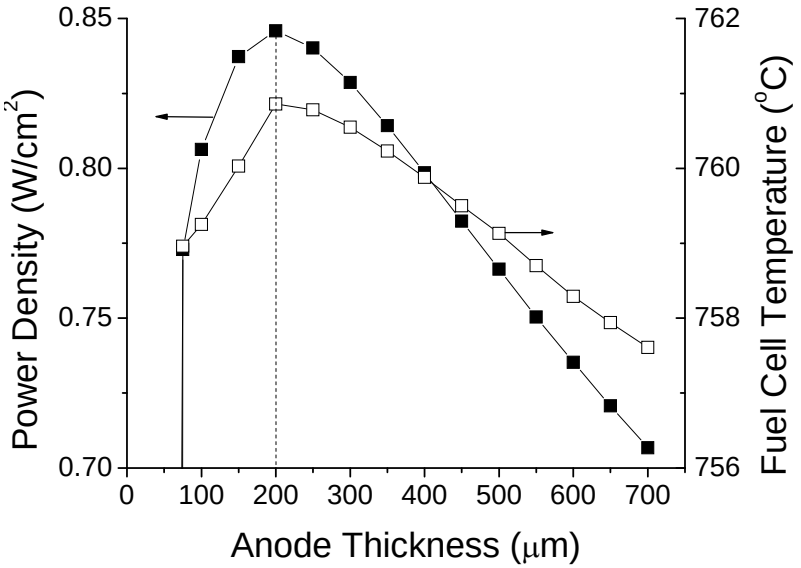

Figure 3-14. Fuel cell power density at 0.4 V and 600°C furnace temperature as a function of anode thickness

In the experimental configuration mentioned earlier, the anode thickness is fixed at 700 μm. The simulation results indicate that the power output is indeed highly sensitive to the anode dimensions and there exists an optimum value. While the maximum in power output may not occur exactly at 200 μm, as suggested by the simulation, it is clear that reducing the anode thickness from its present value will improve performance. The cell temperature has a similar dependence on anode thickness, peaking in this case at 200 μm as well. The computed gas compositions (data not shown) reveal that hydrogen production occurs preferentially at the exterior surface of the anode, and that, for thicker anodes, the maximum hydrogen concentration is high due to the abundance of surface reaction sites. However, the hydrogen concentration at the electrolyte-anode interface is higher for thinner anodes because of the shorter diffusion path, leading to better performance for thin anodes. When the anode thickness is lowered beyond a critical value, the loss of catalytic sites begins to have a detrimental effect, reflected also in the dramatic decrease in cell temperature. These effects combine to produce the thickness dependence of power output evident in Fig. 3-14.

3.3.4 The Influence of Temperature on Fuel Cell Performance

Temperature influences the rates of all reactions in an SCFC and thus it is a critical parameter in SCFC design. By definition, the SCFC must operate within a temperature range high enough for catalytic reactions over the electrode catalyst surfaces to proceed at considerable rates, and yet not too high to harm the selectivity

of the catalysts over the beneficial reactions. In fact, not only the catalytic surface reactions but also the electrochemical reactions at the triple-phase boundary (TPB) depend sensitively on temperature, since these two types of reactions are coupled to each other through the species transport in the porous electrodes, and thus temperature affects their rates not only in a direct (Arrhenius) way but also indirectly through the change of species concentration within the bulk of the electrodes. These effects will be explored in this section.

SCFC with YSZ Electrolyte

The fuel cell performance is computed at different temperatures for an MEA with YSZ electrolyte (described in Table 3-2). The anode and cathode materials are Ni and LSM-YSZ for considerations of electrochemistry and/or catalytic chemistry. The flow rate of methane is fixed at 87 sccm, and oxygen is varied from 60 to 90 sccm, with its ratio to helium fixed at 1:4.

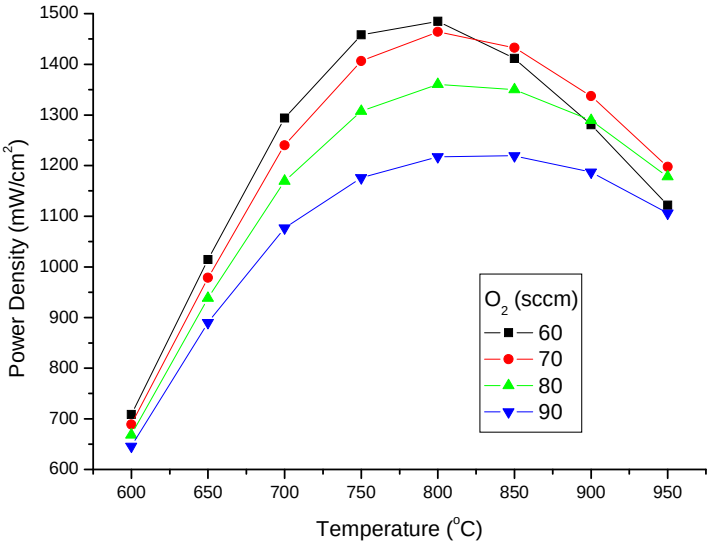

Figure 3-15. Power density of a YSZ cell at different temperatures and oxygen flow rates. Load potential = 0.5 V; T=750^{o}C

The peak power density at each temperature is plotted in Fig. 3-15, and for all oxygen flow rates, the optimum temperature range is around 800°C. Analysis of the surface reaction rates and gas concentrations within the electrodes under different operating conditions show that the existence of the optimum temperature range is mainly due to the change in the cathode exchange current density, partly due to the decrease of selectivity of the cathode for oxygen reduction, and possibly also due to the decrease of selectivity of the anode for reactions producing hydrogen with the increase of temperature.

Anode catalyst selectivity

For anode-supported fuel cells like the one under discussion, the first reason that one might think responsible for the performance loss is the drop in selectivity (i.e., more preferential for combustion) of the anode catalyst for hydrogen generation reactions. To see whether this is true, the global reaction in the whole anode can be obtained by summing the production/consumption rates of the gas-phase species multiplied by the corresponding volume (i.e., area in 2D) over all control volumes:

$$\sum_{k\in \text{ reactants}} \left(\sum_{j=1}^{N} \sum_{i=1}^{M} r_{i,j,k} \Delta x_i \Delta y_j \right) = \sum_{k\in \text{ products}} \left(\sum_{j=1}^{N} \sum_{i=1}^{M} r_{i,j,k} \Delta x_i \Delta y_j \right) . \tag{3.8}$$

The reaction rates of each species can be normalized by the reaction rate of methane, and the normalized global reaction can be written in a general form as follows:

$$CH_4 + \alpha\, O_2 + \beta\, H_2O = \gamma\, H_2 + \epsilon\, CO + \eta\, CO_2 \ . \tag{3.9}$$

Since there is initially no water in the fuel/oxygen mixture, the water in Eq. 3.9 comes from the electrochemistry at the anode-electrolyte interface. Fig. 3-16 shows the absolute and relative reaction rates of the global reaction (3.9) at O_2 flow rate of 60 sccm. Figure 3-16a demonstrates that the absolute reaction rate increases

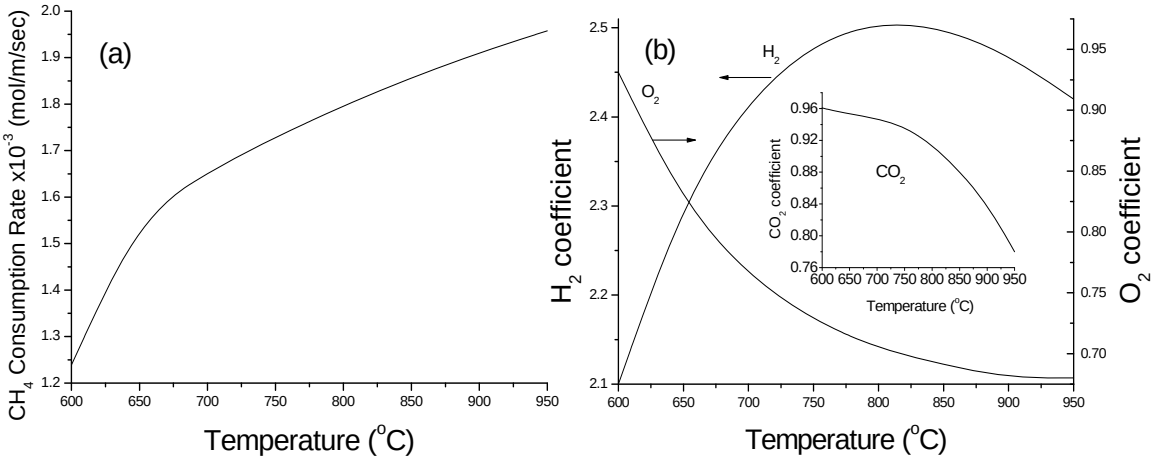

Figure 3-16. Reaction rates of the global reaction in the anode at O_2 flow rate of 60 sccm and temperature of 750°C; (a) absolute rate of methane, (b) relative rates of selected species

monotonically with temperature, but figure 3-16b shows the H_2 coefficient peaks at 800°C and the relative O2 consumption is always decreasing. Also, the CO_2 coefficient drops from 0.96 at 600°C to 0.78 at 950°C, indicating that the global reaction is even less in favor of combustion of methane at higher temperatures, but is more favorable to the production of CO (by carbon balance) than H_2 at temperatures 800°C and higher. Therefore, it can be inferred from Fig. 3-16 that the selectivity of the anode catalyst for H_2 production drops at temperatures higher than 800°C, although the absolute production rate of H_2 still goes up with temperature.

Reaction rates at other O_2 flow rates are similar to Fig. 3-16, but the production rate of H_2 decreases with O_2 flow rate and water becomes a net product at O_2 flow rate of 90 sccm. This explains the drop of power density at ~ 800°C for O_2 flow rate

changing from 60 to 90, but still does not account for the existence of the maximum power density versus temperature for each O_2 flow rate. Since the absolute production rate of hydrogen increases with temperature, the selectivity of the anode catalyst cannot be the major reason for the decrease of power output when temperature is higher than 800^{o}C.

Exchange current density

Therefore the focus is switched to exchange current density i_0. First of all, a sensitivity analysis in [6] computed with the same electrochemistry parameters based on [56] showed that the fuel cell power output is much more sensitive to i_0 on the cathode side because the cathode charge-transfer overpotential is higher, and thus increasing the exchange current density on the cathode side can improve the fuel cell performance more significantly by reducing this overpotential. A similar test is calculated for this example and also shows that the fuel cell power output is not sensitive to the anode i_0, indicating that the anode exchange current density cannot be the reason for the deterioration of power density at high temperatures either. However, it must be pointed out that the exchange current densities in [56] is specifically formulated for the Ni|YSZ|LSM-YSZ system, which turns out to have a higher overpotential across the cathode-electrolyte interface. This may not be true for other systems, for example, those with BSCF cathodes, and the analysis in this section may not apply to the exchange current density on the cathode side, but actually to whichever electrode that has a higher overpotential.

So the most likely reason is the cathode exchange current density, which is a function of the oxygen partial pressure $p_{O_2,c}$ at the cathode-electrolyte interface, given by [56]

$$i_{0,c} = i^*_{O_2} \frac{\left(p_{O_2,c} / p^*_{O_2}\right)^{1/4}}{1 + \left(p_{O_2,c} / p^*_{O_2}\right)^{1/2}} \tag{3.10}$$

where the reference pressure $p^*_{O_2}$ was presented by Matsuzaki et al. [82] for an LSM-YSZ interface as

$$p^*_{O_2} = A_{O_2} \exp\left(-\frac{E_{O_2}}{RT}\right) \tag{3.11}$$

with $i^*_{O_2} = 2.8\ \mathrm{A/cm^2}$, $A_{O_2} = 4.9 \times 10^8\ \mathrm{atm}$, and $E_{O_2} = 200\ \mathrm{kJ/mol}$. The oxygen partial pressure $p_{O_2,c}$ and the exchange current $i_{0,c}$, calculated with $p_{O_2,c}$, are plotted in Fig. 3-17.

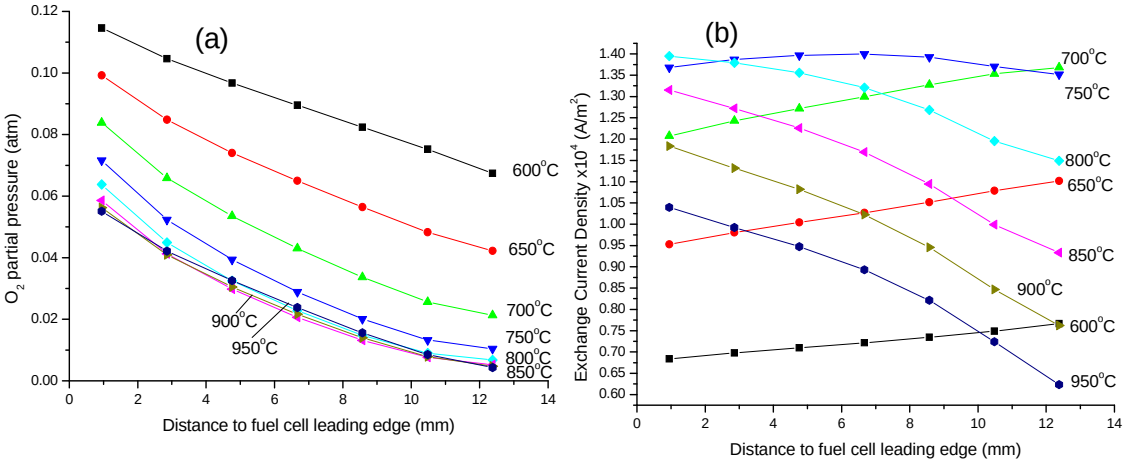

Figure 3-17. The oxygen partial pressure (a) and exchange current density (b) at the cathode-electrolyte interface along the fuel cell at different temperatures; O_2 flow rate: 60 sccm

It can be seen that due to oxygen depletion along the flow direction, $p_{O_2,c}$ decreases with distance from the fuel cell leading edge. At any location *x* along the cathode, the pressure goes down with temperature, and does not change much when temperature is higher than 800°C. This is because the rates of the parasitic combustion

of the fuel species CH_4, H_2 and CO increase with temperature and outweigh the increase of O_2 partial pressure in the gas feed. Since an ideal cathode of an SCFC should only promote oxygen reduction and be inert towards full oxidation reactions, this means the selectivity of the cathode decreases with temperature. By comparison with the monotonic decrease of $p_{O_2,c}$, the exchange current $i_{0,c}$ maximizes at 750°C, and it increases with distance from the fuel cell leading edge at lower temperatures, while it decreases with the distance at higher temperatures. This is because the reference pressure $p^*_{O_2}$ grows Arrheniusly with temperature, so that $p_{O_2,c} / p^*_{O_2}$ is much larger than 1 at low temperatures and smaller than 1 at high temperatures. The power density in Fig. 3-15 maximizes at 800°C instead of 750°C because the growth of the exponential term in the Butler-Volmer equation with temperature exceeds the decrease of the exchange current density in the range of 750°C to 800°C.

Corresponding to the influence of the cathode exchange current density on power output (and thus the current density), the partial pressures of H_2 minimizes at 800°C and that of H_2O maximizes at the same time (Fig. 3-18). The trend is the same at all other oxygen flow rates.

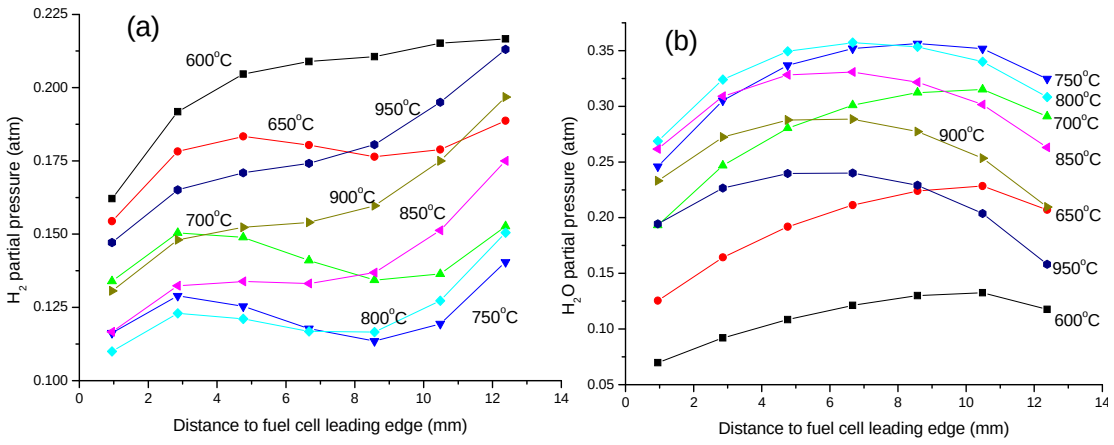

Figure 3-18. The partial pressures of (a) H_2 and (b) H_2O at the anode-electrolyte interface

A comparison of the cathode i_0 at different O_2 flow rates shows that its value does not change significantly with O_2 flow rate below 750°C, but increases considerably with O_2 flow rate above this temperature. Also, the higher the temperature is, the more noticeable the change is. This is because of two reasons: First, although $p_{O_2,c} / p^*_{O_2}$ is smaller than 1 at higher temperatures, the increase in O_2 flow rate increases the value of $p_{O_2,c}$ and thus brings the ratio closer to 1. Second, the monotonicity of function $x^{0.25}/(1+x^{0.5})$ (for equation 3.10) leads to a sharp increase with x for $0 \le x \le 1$ and a slow decrease with x for $x > 1$. This explains why in the temperature range below 800°C in Fig. 3-15 the curves for various O_2 flow rates all increase sharply, but when temperature is higher than 800°C, they decrease more and more slowly with the increase of O_2 flow rate.

A further examination of the cathode i_0 also reveals that the value of the exchange current density is very close at 800°C for different O_2 flow rates. Thus the trend that the maximum power density decreases with O_2 flow rate cannot be explained by the cathode i_0. This actually falls back to the question of the optimum fuel/oxygen ratio. The result shows that the total production rate of hydrogen within the anode decreases monotonically with O_2 flow rate, and thus 60 sccm is the best among the four oxygen flow rates and should yield the highest power.

SCFC with SDC Electrolyte

A different fuel cell with an SDC electrolyte is also computed, the ionic conductivity of which is assumed to be twice of the value of YSZ. The influence of

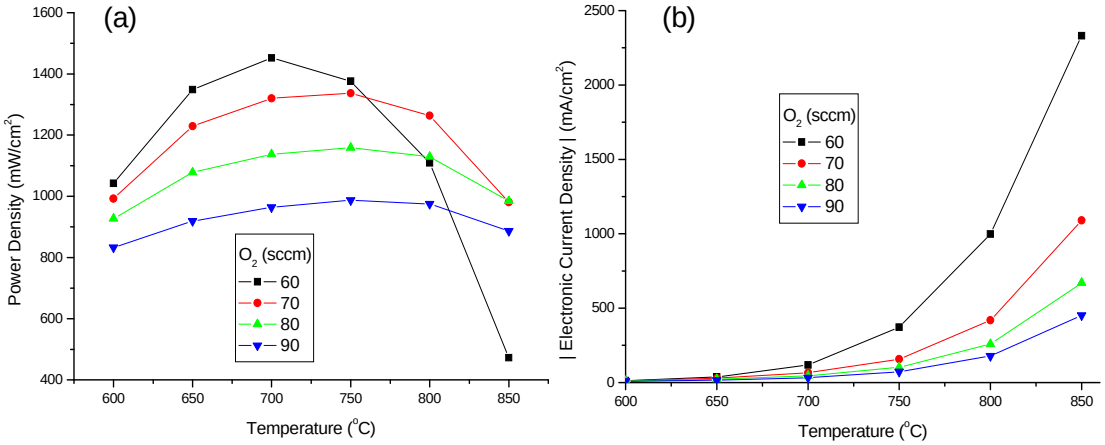

Figure 3-19. Performance of an SDC cell at different temperatures and oxygen flow rates; Load potential = 0.4 V; T=750^{o}C; (a) Power density, (b) Electronic current density

temperature on power density is shown in Fig. 3-19. By comparison with the YSZ case, the curves are much less steep at lower temperatures (i.e., below 750^{o}C) due to the higher ionic conductivity of SDC. However, as shown in the second figure, the reverse (i.e., negative) electronic current grows dramatically with temperature, resulting in a significant reduction in the maximum power density that offsets the benefit of the high ionic conductivity, and shifts the temperature corresponding to the maximum power to a lower temperature by 50 to 100^{o}C. At each temperature in Fig. 3-19b, the electronic current is suppressed by a higher O_2 flow rate due to the increase of O_2 partial pressure at the cathode-electrolyte interface. Under the combined influence of temperature and O_2 partial pressure, the power density curve corresponding to O_2 flow rate of 60 sccm in Fig. 3-19a drops drastically at higher temperatures (i.e., above 700^{o}C). Except for these differences, the influence of temperature on the cathode exchange current density, the ionic current density, and the concentrations of H_2 and H_2O at the anode-electrolyte interface are similar to the YSZ case.

In brief summary, for anode-supported SCFCs with Ni anode and the electrochemical properties discussed above, within normal operating temperature range, temperature influences the fuel cell performance mainly through the influence on the exchange current of the electrode (in this case the cathode) that has a higher resistance for the charge-transfer reactions, rather than the selectivity of the anode material over H_2-generating reactions. The reference pressure $p^*_{O_2}$, which is an inherent characteristic of the cathode material, is the key factor in the change of power output versus temperature. The decrease of cathode selectivity contributes to the change of cathode current density by affecting the oxygen partial pressure, and the selectivity of the anode catalyst decreases with temperature above 800^{o}C, but either is unlikely to be the primary reason for the influence of temperature on fuel cell power. For fuel cells with MIEC electrolytes such as SDC, power output at high temperatures is also harmed by the exponential growth of the reverse electronic current, especially at lower oxygen flow rates.

3.3.5 Flow Rate, Power Output and Efficiencies of SCFC

Fuel cell efficiency and fuel utilization are the most important issues on the system design level. The fuel cell efficiency is defined as [56]

$$\eta = \frac{W_e}{\dot{m}_{f,in}\Delta h_{in}} \tag{3.12}$$

where W_e is the electrical power output of the fuel cell, $\dot{m}_{f,in}$ is the fuel mass flux at the inlet, and Δh_{in} is the enthalpy released by completely oxidizing the fuel (i.e., combustion heat). The fuel utilization efficiency is defined as [56]

$$\varepsilon_U = 1 - \frac{\dot{m}_{\mathrm{f,out}} \Delta h_{\mathrm{out}}}{\dot{m}_{\mathrm{f,in}} \Delta h_{\mathrm{in}}} \tag{3.13}$$

where $\dot{m}_{\mathrm{f,out}}$ is the mass flux of the fuel at the channel outlet and Δh_{out} is the heating value associated with completely oxidizing the exhaust flow. In this discussion, the lower heating value (LHV) of methane and other fuels (H_2, CO) is used to define η and ε_U. The LHV is defined as the amount of heat produced by the complete combustion of a unit quantity of fuel when the water in the product is in a vapor form. By definition, η and ε_U depend on both the fuel (yet not relevant to oxygen) flow rates at the inlet and the electrical performance (e.g., power output) of the fuel cell. The influence of both factors will be discussed in this section.

Efficiency and Fuel Utilization versus Fuel Flow Rate

First of all, the influence of fuel flow rate is explored: To start with, the same YSZ cell discussed in the last section is simulated with a fixed ratio of the gases in the gas mixture, CH_4:O_2:He = 1:0.8:3.2. Temperature is 750°C and load potential is 0.5 V. Compared with SDC cells, the YSZ cell has the advantage of avoiding the reverse electronic current that could be extremely high at low oxygen flow rates. The high

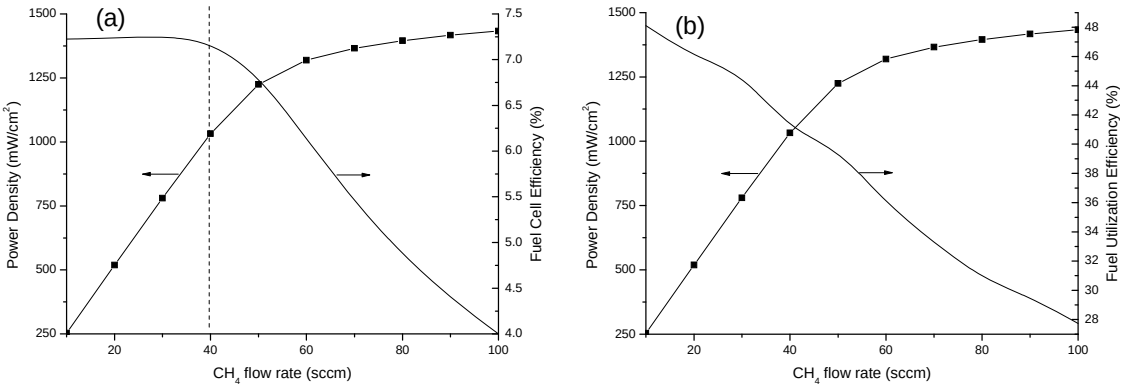

Figure 3-20. Power output and efficiencies of a YSZ cell at different methane flow rates with a fixed ratio of CH4:O2:He = 1:0.8:3.2; T=750°C; E=0.5 V

electronic current keeps the computation from going down in oxygen flow rate (and the total flow rate) because the total power output decreases much faster compared with YSZ cells, and thus the YSZ cell is a better choice for studying the efficiencies.

Results at a fixed methane/oxygen ratio

The power density and efficiencies are shown in Fig. 3-20, charted against the methane flow rate, which ranges between 10 sccm and 100 sccm with a step size of 10 sccm. In Fig. 3-20a, it can be seen that when CH_4 is less than 40 sccm, the power density increases linearly with CH_4 flow rate, and the fuel cell efficiency is almost a constant (~ 7.2%). This indicates that the electrical power generated by the fuel cell is controlled by transport (i.e., diffusion and convection) of (some) gas species. However, when CH_4 is higher than 50 sccm, the power density gradually levels off and the efficiency decreases almost linearly to 4%. This indicates that when the fuel flow rate is high enough, the transport limitation goes away, and power generation is limited by the kinetics (both catalytic and electrochemical) in the fuel cell. On the other hand, the fuel utilization efficiency in Fig. 3-20b decreases monotonically with CH_4 flow rate in the whole range from 48% to 28%. This is because the increase of methane flow rate improves the channel flow speed and thus increases the amount of fuel that bypasses the fuel cell.

Analysis and improvement

To have a better understanding of the efficiency curves, Fig. 3-21 plots the conversion percentage of methane and oxygen versus methane flow rates. It is

interesting to notice that the conversion curve of oxygen has a trend similar to the fuel cell efficiency curve, while the conversion curve of methane is very similar to the fuel utilization curve. This further indicates that the flow rate of oxygen is the controlling factor for the fuel cell efficiency, since oxygen has a higher conversion percentage than methane, and thus the transport limitation of oxygen is the bottleneck of the fuel cell power output. For the same reason, the amount of unspent methane that bypasses the fuel cell is much more than oxygen, and should increase with the incoming methane flow rate. This explains the monotonic decrease of the fuel utilization.

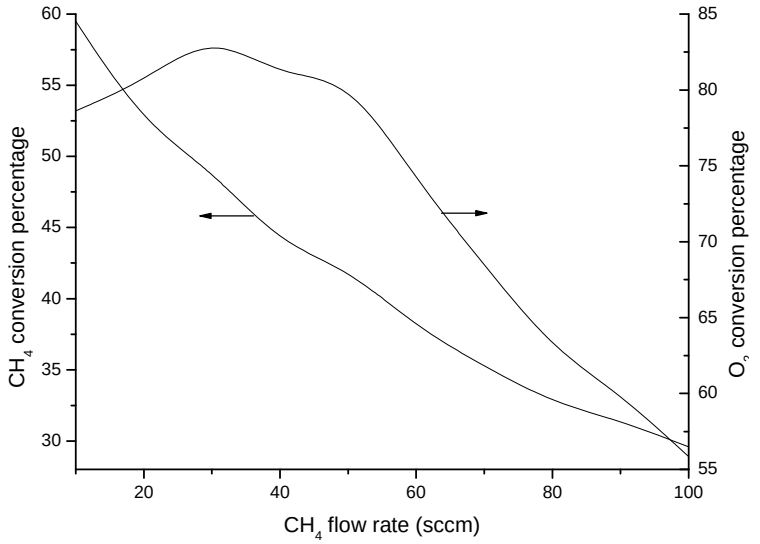

Figure 3-21 Conversion percentages of methane and oxygen at different methane flow rates

Based on the above analysis, the fuel cell efficiency could be improved by increasing the amount of oxygen, especially for methane flow rates lower than 40 sccm. This is verified by simulation results at higher oxygen flow rates. Fig. 3-22 shows the fuel cell efficiency and fuel utilization percentage for a O_2:CH_4 ratio from 0.8 to 1.6 with a step size of 0.2. The maximum fuel cell efficiency of each curve initially increases with the ratio up to 13.3% at O_2:CH_4 = 1.4, and then drops sharply

afterwards. On the other hand, when the flow rate is high, the fuel cell efficiency decreases almost linearly with the O_2:CH_4 ratio. The analysis is as follows.

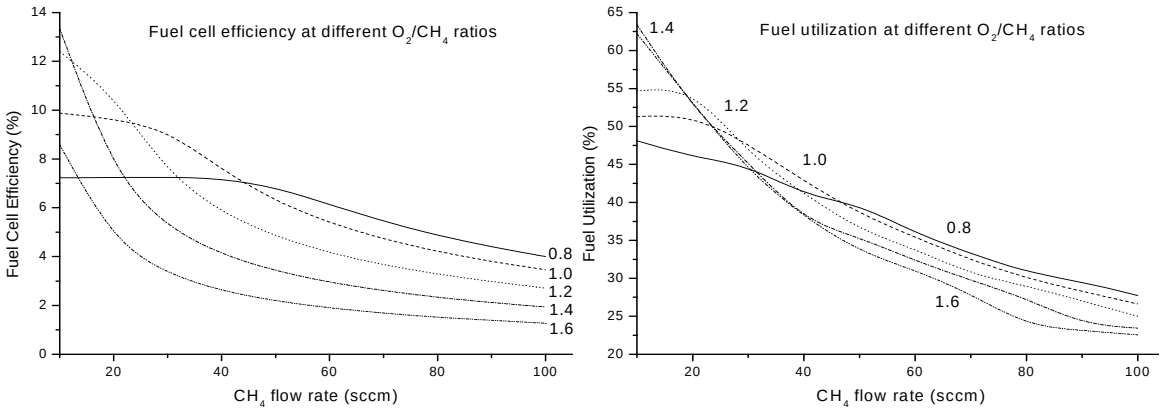

Figure 3-22. LHV efficiency and fuel utilization of a YSZ cell at different O_2/CH_4 ratios

Since in the definition of fuel cell efficiency (equation 3.12), the incoming enthalpy of the fuel only depends on the methane flow rate, the change of efficiency with different O_2:CH_4 ratio at each methane flow rate is essentially the change of power output with respect to the same set of conditions. Therefore, the efficiency curves can be analyzed in a similar way as in the last section. On the lowest end of methane flow rate, simulation result shows the oxygen partial pressure at the cathode-electrolyte (C-E) interface can be very low due to the consumption by electrochemistry and combustion of the fuel on the cathode side. For example, at O_2:CH_4 = 0.8, the incoming oxygen partial pressure is 0.16 atm; but at CH_4 flow rate of 10 sccm, the O_2 partial pressure at the C-E interface $p_{O_2,c}$ is in the range of 3×10^{-8} to 1×10^{-4} atm. This pressures increases with the O_2:CH_4 ratio to the range of 2.5×10^{-2} to 7×10^{-2} atm at O_2:CH_4 = 1.6 at the same methane flow rate. By comparison, the reference pressure (equation 3.12) at 750°C is $p^*_{O_2} = 3\times10^{-2}$ atm. Recall that in the

definition of cathode exchange current density $i_{0,c}$ (equation 3.10), for $x = p_{O_2,c} / p^*_{O_2} \in [0,1]$, function $x^{0.25}/(1+x^{0.5})$ increases sensitively with x, increasing O_2:CH_4 ratio can significantly improve $i_{0,c}$. However, as O_2:CH_4 ratio approaches 1.4, the ratio $p_{O_2,c} / p^*_{O_2}$ is very close to 1, so that the maximum fuel cell efficiency peaks at O_2:CH_4 = 1.4. When the ratio is higher than 1.4, $p_{O_2,c} / p^*_{O_2}$ is larger than 1, so that the cathode j_0 becomes insensitive to $p_{O_2,c}$ (and thus the O_2:CH_4 ratio). In this range, the fuel cell power output is dominated by the anode side exchange current density $i_{0,a}$ instead, which decreases with the O_2:CH_4 ratio. This is because the global reaction in the anode is more in favor of the H_2 production at lower O_2:CH_4 ratio, so that the H_2 concentration at the anode-electrolyte interface decreases with the O_2:CH_4 ratio, resulting in the same trend in anode exchange current density. This explains the drop of fuel cell efficiency when O_2:CH_4 is higher than 1.4.

The reason for the monotonic decrease of fuel cell efficiency with O_2:CH_4 ratio at higher flow rates is as follows. Along the methane flow rate axis (horizontal), when CH_4 is higher than 50 sccm, $p_{O_2,c}$ becomes universally higher than $p^*_{O_2}$, so that $i_{0,c}$ plateaus as discussed. Under this condition, the fuel cell power output is predominantly determined by $i_{0,a}$, which decreases with the O_2:CH_4 ratio due to its influence on H_2 production rate.

The change of fuel utilization is similar to the fuel cell efficiency. The reason is that it changes in the same way as the current density. (This will be discussed shortly.) Since in the above discussion the load potential is fixed, the fuel utilization changes in the same way as the fuel cell power output and thus the fuel cell efficiency.

Efficiency and Fuel Utilization at Constant Fuel Flow Rate

Besides the investigation of the influence of fuel flow rate on η and ε_U, a study of their dependence on the fuel cell electrical performance (e.g., I-V relationship) will provide more insights on relevant factors and thus could indicate possible approaches to improve the efficiencies. In the following discussion, the incoming flow rates of all gas species will be fixed at CH_4:O_2:He = 100:100:400 sccm.

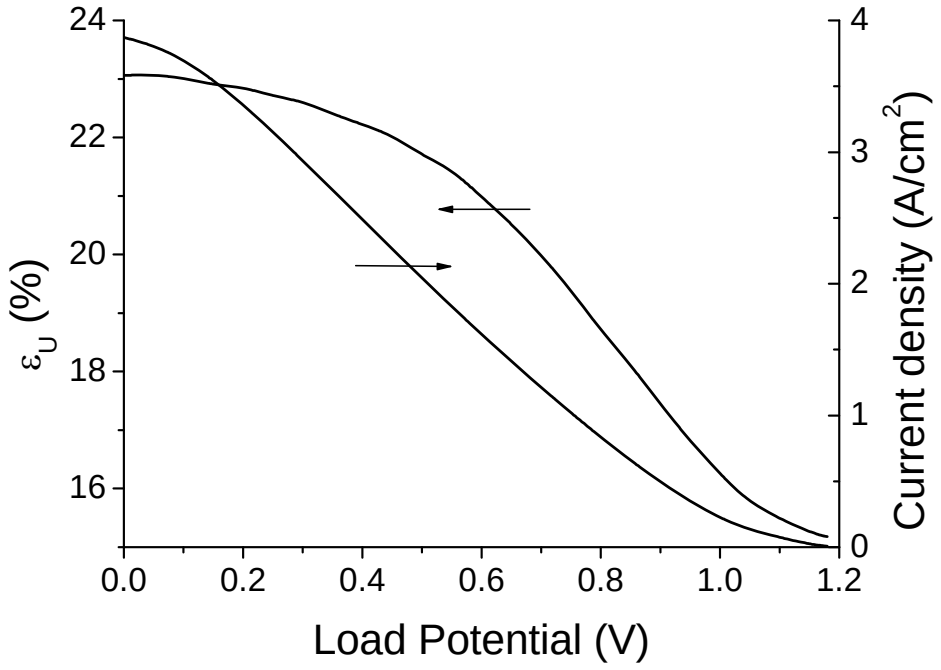

Figure 3-23. Fuel utilization ε_U and current density as functions of load potential

Result

With the fixed flow rates, the LHV of the inlet fuel is irrelevant to the operating conditions of the fuel cell, and so η changes in the same way as the fuel cell power W_e does. Therefore it maximizes where the power output does. In contrast, the fuel utilization depends on voltage in a very similar manner as the current does, also assuming fixed gas flow rates. As shown in Fig. 3-23, fuel utilization efficiency ε_U

decreases monotonically with load potential. The similarity is because the consumption rate of hydrogen by electrochemistry at the anode-electrolyte interface strongly influences the conversion of methane by partial oxidation, reforming and water-gas shift reactions.

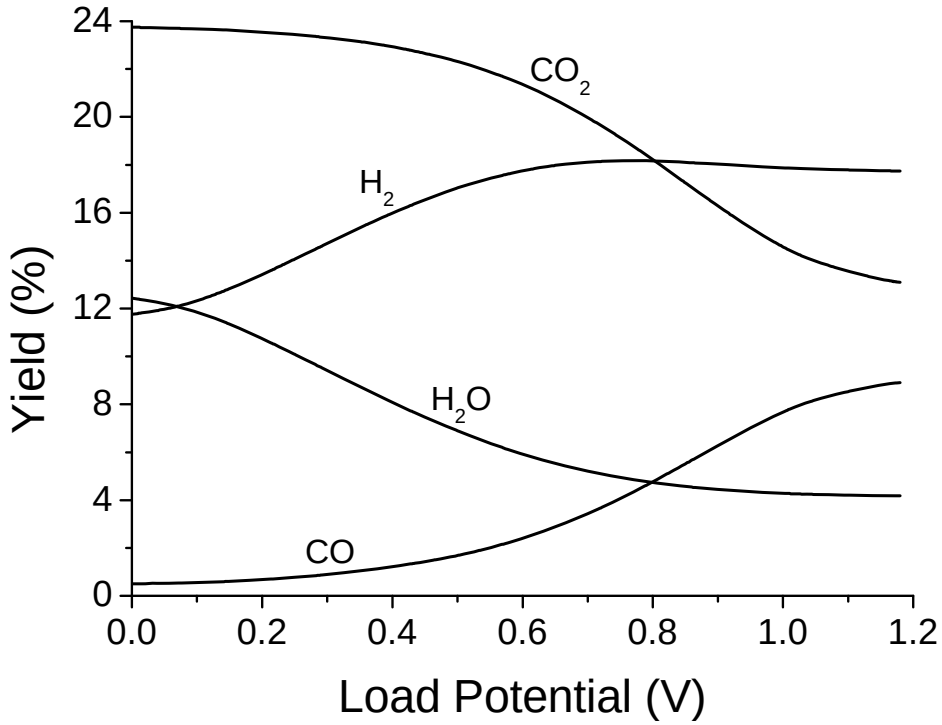

Figure 3-24. Yield percentage of gas-phase product species as functions of load potential. CO and CO_2 are based on C balance; H_2 and H_2O are based on H balance

Analysis

To better understand this relationship, it is meaningful to explore the conversion of methane to other products relevant to the load potential. First of all, two definitions "yield" and "selectivity," need to be introduced for further discussion. The yield of species *k* is the ratio of the total amount of product *k* to the initial amount of reactant; the selectivity of species *k* is the ratio of the total amount of product *k* to the total amount of product of interest. Both percentages need to be calculated based on the

balance (conservation) of one element that the species contains (which in our case could be C, H, or O). Fig. 3-24 and 3-25 show the yield and selectivity percentages (calculated at the outlet of the flow channel) of the products including CO, CO_2, H_2, and H_2O. They demonstrate that at short-circuit condition, reacted methane is almost uniformly converted to CO_2 because the consumption rate of hydrogen by electrochemistry is at its highest. As a result, water concentration is highest while hydrogen concentration is lowest (compared with their concentrations at other voltages). At open-circuit condition however, although very little hydrogen is consumed by electrochemistry, the fuel utilization is still 15%. This is because the catalytic reactions mentioned above are still occurring within the porous Ni anode. Since very little hydrogen is consumed by electrochemistry, the water must be generated by (direct or equivalent) full-oxidation of methane. Meanwhile, both H_2 and

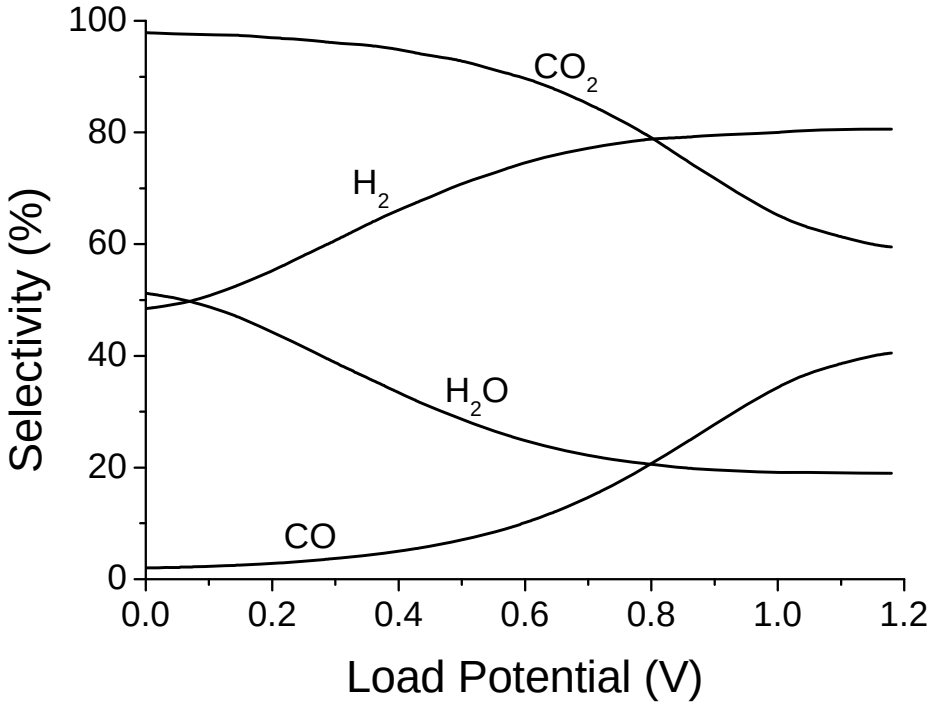

Figure 3-25. Selectivity percentage of gas-phase product species as functions of load potential. CO and CO_2 are based on C balance; H_2 and H_2O are based on H balance

CO reach their maximum, indicating that the reaction rates of methane reforming and water-gas shift reaction are still high.

Possible Approaches for Improving the Efficiency and Fuel Utilization

Based on the above analysis, the efficiency and fuel utilization of the SCFC system are generally low. Although the reasons seem complicated, they all boil down to the unspent fuel that bypasses the fuel cell due to some lack of optimization in the system design. Therefore, the optimization of flow rate, fuel/oxygen ratio, flow geometry, fuel cell layout, microstructure parameters of the electrodes and parameters of electrochemistry (such as the exchange current density), as well as some operating conditions such as the temperature and load potential, are all very important to the improvement of the efficiency and fuel utilization. Except the flow rates, all other parameters contribute to the improvement by enhancing the fuel cell power output. The influence of these two categories is discussed as follows.

The flow rates, and especially the flow rate of the fuel, determine the amount of energy coming into the system. If only high efficiency and high fuel utilization are sought, then the lower flow rate is the better, since it brings longer residence time for catalytic surface reactions in the electrodes and lower spatial speed in the flow channel, thus allowing more time for reactants to diffuse to the fuel cell and reducing the amount of fuel wasted. However, there are also a few drawbacks. At low flow rates, at least one of the reactants (the fuel or oxygen) is depleted very quickly along the flow direction, resulting in a “partly working” fuel cell, meaning only a short

portion of the fuel cell is actually generating power. Furthermore, based on the simulation results, high efficiencies and high power are not very likely to be achieved at the same time. Lower flow rates set a smaller upper limit for the total energy from which the electrical power can be extracted, and thus limit the total power output. Higher flow rates, on the other hand, improve the distribution of reactants along the whole fuel cell and improves the total power output, but at the cost of increasing the flow speed and the unreacted fuel that bypasses the fuel cell.

Since in practical applications, high total power output is often desired over high efficiency, the factors that could contribute to the improvement of fuel cell power generation carry more weight in the optimization of an SCFC system. In general, the factors that are less dependent on others can be optimized first. This includes the well-known approaches of using highly selective and catalytic electrode materials that also have high exchange current density, together with ways to make the diffusion path of gas-phase species shorter by improving the microstructure of the electrode (such as using a higher porosity). The discussion in this chapter also suggests that reducing the anode thickness by some extent can improve the performance by the same reasoning.

As for flow geometry, a few things need to be considered. First, simulation results show that a narrower channel can effectively improve the fuel cell power by forcing the gas flow closer to the fuel cell and reducing the waste of reactants. Therefore, narrower channels should be adopted in SCFC systems. Second, improving fuel cell performance by changing fuel cell orientation might not be feasible because the total area of vertical fuel cells is limited by the channel height, limiting the total

power output. Third, multiple fuel cells should be used as an array (or a stack) in the same flow channel to increase the total power output. As discussed in this chapter, the layout of the fuel cells makes a difference in their performance. Relative positions that harm the functionality of neighboring fuel cells should be avoided. A design with a decreasing number of fuel cells and shrinking cross-section area of the flow channel should make a good use of the fuel and thus give a high performance. At the channel inlet, fuel cells should be deployed in pairs with either anode-facing-anode or cathode-facing-cathode configuration. Downstream to these cells, a narrower channel with only one fuel cell at each horizontal location can be used to improve the fuel utilization and power generation. For this design, high gas flow rates have to be used.

Other factors including fuel/oxygen ratio, temperature, and load potential need to be optimized together with the parameters discussed above. For a single cell with YSZ electrolyte, the best temperature range is 750 to 800^{o}C, and the one for cells with SDC electrolyte is lower by 50^{o}C or more. However, the exchange current is also an important consideration for determining the optimum temperature range. As discussed above, the inherent characteristic of the exchange current at different temperatures can significantly affect the location of the peak power. Furthermore, for a multi-cell SCFC system, downstream cells might have a different optimum temperature range than the upstream ones, due to the change of gas concentration along the flow direction and thus the change in exchange current. Under such situations, more weight should be given to the cells generating the highest power when determining the optimum temperature range for the whole system. Due to these complications, the optimization

process of the temperature needs more experimental and modeling study on the basis of a good knowledge of the fuel cell's catalytic and electrochemical properties. Likewise, the optimum fuel/oxygen ratio and load potential for a multi-cell system also depend on the above factors, due to the spatial variation in composition for the goal of maximizing the total power output; these also require further research combining experimental and modeling.

Chapter 4
Adaptation of the SCFC Model to Dual-Chamber Fuel Cells

4.1 Introduction

The SCFC model has been capable of predicting the discharge characteristic of SCFCs and proves a useful tool for systematically optimizing the SCFC systems. Compared with other types of fuel cell systems, the physical and chemical processes involved in a SCFC system are more complex, due to the mixing of fuel and oxidant. Given the model's capability to manage geometry in the flow channel and complex physics plus chemistry in the MEA, it is not difficult to adapt the model to simulate other types of fuel cells, specifically fuel cells in the commonly seen dual-chamber configuration.

Generally speaking, the working principles of the MEA of different types of fuel cells are similar, but the performance of the fuel cell can often be transport-limited in two-dimensions or more. Compared with the existing plug-flow (1-D) models [56] for most dual-chamber SOFC, the 2-D numerical model developed here provides a more powerful tool to study the influence of transport phenomena in one more dimension. In particular, many dual-chamber tests were performed in a button-cell configuration, and this is beyond the capability of the plug-flow models. Compared with some existing two- and three-dimensional models [33, 47], the detailed chemistry enables the model presented here to study the fuel cell operation with deeper insights into the

fundamental physical and chemical processes. In addition, the MEA submodel's capability of automatically refining the computational grids (discussed in the next chapter) provides higher accuracy and reliability for studying fuel cell performances. Dual-chamber fuel cells with both oxygen-ion-conducting and proton-conducting electrolytes are discussed in this chapter.

4.2 Dual-Chamber Solid Oxide Fuel Cells

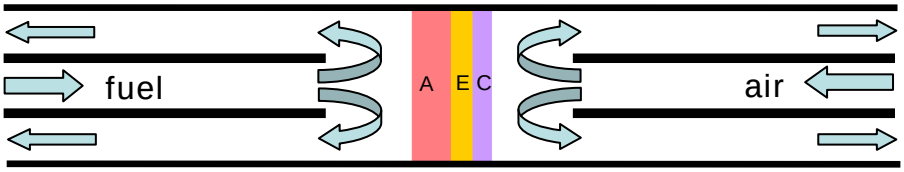

Figure 4-1. Schematic diagram of a dual-chamber SOFC in the button-cell configuration. A: anode; C: cathode; E: electrolyte

The planar fuel cell in the button-cell configuration is illustrated in Fig. 4-1. The anode chamber and cathode chamber are separated by the MEA with seals to prevent gas leakage. In many experiment designs, tubes with a smaller diameter are often used to deliver the fuel (H_2 or hydrocarbons) and oxidant (usually air) to the anode and cathode respectively. This flow geometry can be handled by the SCFC model by defining a vertical MEA in the flow channel that extends to both the top and bottom walls with the addition of several inert objects (walls) to represent the tubes for gas delivery.

In experiments, the flow rates of the fuel and the air are often high enough so that the power output does not go up with flow rates anymore. The model assumes this condition when simulating dual-chamber fuel cells, and the primary reason is that the simplification of the gas species mass flux (equation 2.6) requires that the spatial

variation of the mean molecular weight be small. Unlike the single-chamber cases, the dual-chamber fuel cells do not usually have a dominant balance gas in the anode chamber, and thus the small variation in the mean molecular weight needs to be satisfied by using high flow rates. Also for this reason, the dimensions of the flow channel and the fuel cell do not matter to the power density, and thus give the computation more flexibility.

In this section, a YSZ-electrolyte cell is simulated with parameters taken from [56] unless stated otherwise. To briefly summarize, the simulation is performed for the geometry in Fig. 4-1 with anode, cathode, and electrolyte thicknesses being 1220, 30, and 25 μm respectively. Flow rates are high enough, and temperature is 800^{o}C isothermal.

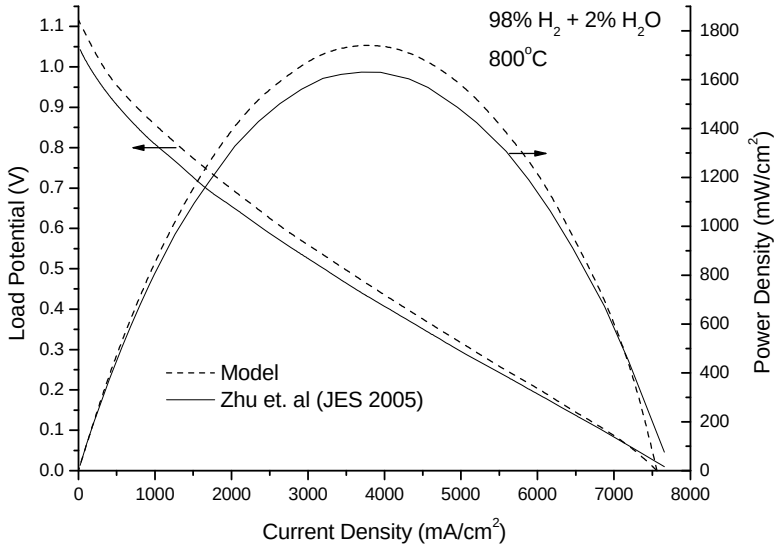

Figure 4-2. Discharge characteristics of a dual-chamber SOFC with moisturized H_2 fuel

First of all, the model simulates the polarization curve using moisturized H_2 (98 vol% H_2 + 2 vol% H_2O) and air, and the result is compared with [56]. Fig. 4-2 shows that the simulated curve has a good agreement with literature results. However there

are some slight differences with the peak power and the open-circuit voltage. This is probably because of the difference in geometry. Reference [56] uses a 5cm-long flow channel with a cross-section area of 1 mm^2. With such a high aspect ratio, the depletion of the fuel and oxygen along the channel should be more significant than in the button cell discussed here. The good match verifies that the SCFC model can be adapted to simulate dual-chamber fuel cells.

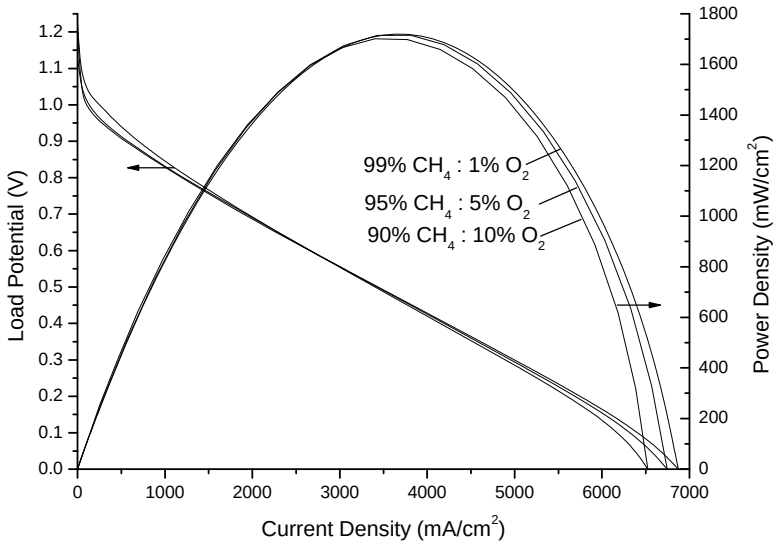

Figure 4-3. Discharge characteristics of a dual-chamber fuel cell running on methane with small oxygen addition in the anode chamber

Secondly, the model is used to simulate the fuel cell running on methane with small oxygen addition in the anode chamber. This approach has been used by some experimental groups [83] to mitigate the coking problem for cells running on hydrocarbon fuels. Three cases with 1 vol%, 5 vol%, and 10 vol% oxygen are simulated respectively, and the polarization curves are plotted in Fig. 4-3. The comparison shows that even with a 10 vol% oxygen addition, the drop of maximum power density is only 1.5%. Although similar experimental studies in literature use higher hydrocarbons (e.g., octane), the qualitative conclusion should be the same: i.e.,

the small addition of oxygen in the anode chamber does not significantly affect the cell efficiency (or power output). The coking issue is not discussed here because the anode reaction mechanism was not designed for predicting coking. However, the reactions in the anode in the presence of minor amount of oxygen will be discussed in the next chapter in greater detail.

4.3 Dual-Chamber Solid Acid Fuel Cells

Lastly, as a further examination of applying the general theoretical framework to different types of fuel cells, the dual-chamber model is modified to simulate solid acid fuel cells (SAFC). Solid inorganic acid compounds (or simply, solid acids) such as $CsHSO_4$ and $Rb_3H(SeO_4)_2$ have high proton conductivities, but they have generally been thought unsuitable for fuel cell electrolytes until Haile's study very recently [84]. By definition, the major difference between the SOFC and the SAFC is the ion conduction and electrochemistry. The electrolyte of SOFC (e.g., YSZ) conducts oxygen ions from cathode to anode, while the electrolyte of SAFC (e.g., $CsHSO_4$) conducts protons from anode to cathode. Correspondingly, water is generated on the cathode side in an SAFC as opposed to the anode side in an SOFC.

Except the ion conduction, another significant difference is that solid acid fuel cells operate at a much reduced temperature range of 230 – 250^{o}C. They operate in this temperature range because it is required in order for the solid acid to go through phase transition and acquire higher conductivity. Fig. 4-4 shows the change of conductivity of CsH_2PO_4 with temperature [85].

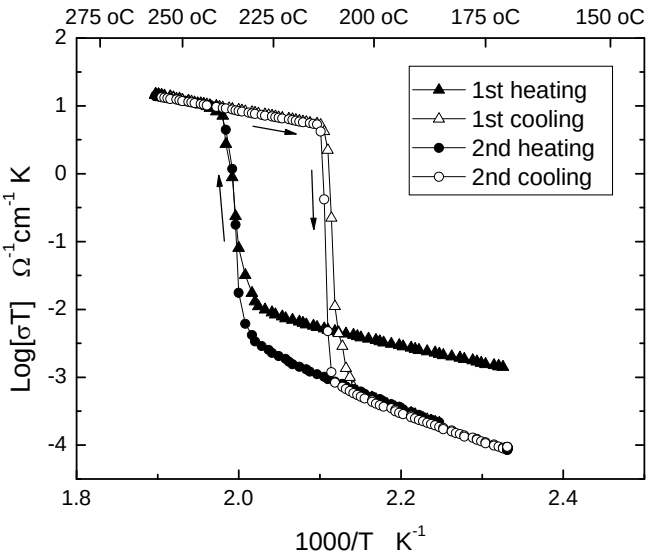

Figure 4-4. Conductivity of polycrystalline CsH_2PO_4 versus temperature [85]

Like the SOFCs, solid acid fuel cells also have many issues in design and testing that require further understanding to improve their performance. For example, the heating effect due to charge transfer reactions changes the actual temperature of the MEA and thus sensitively influences the fuel cell's performance [79]. To understand these critical issues, the joint effort of experiment and modeling would prove more efficient, similar to the pattern that works for SOFCs. However, modeling study for this type of fuel cells has not been reported in the literature. As the first step to simulate the SAFC, the dual-chamber SOFC model can be modified based on the differences mentioned above and then calibrated and validated based on experimental data, a procedure introduced in the third chapter.

On the modeling side, the change of electrochemistry needs the values of exchange current densities for charge transfer reactions at the anode-electrolyte and cathode-electrolyte interfaces, respectively. The asymmetry factors (or charge transfer

coefficients) of the Butler-Volmer equation will be evaluated later through the fitting process to experimental data.

Due to the limited availability of experimental data [85], the simulation is performed at 250°C with exchange current densities and electrolyte conductivity measured at the same temperature. The anode and cathode exchange current densities are $j_{0,a} = 1150\ \mathrm{A/cm^2}$ and $j_{0,c} = 54\ \mathrm{A/cm^2}$, respectively [85], and the conductivity of CdP is 2.88 Ω^{-1} m^{-1}. Highly moisturized hydrogen (60 vol% H_2 + 40 vol% H_2O) and oxygen (60 vol% O_2 + 40 vol% H_2O) at high flow rates are used for the anode and cathode chambers, respectively. The thickness of the anode, cathode, and electrolyte are all 100 μm.

Since the asymmetry factors of the Butler-Volmer equation are unknown, the model was first calibrated by adjusting these factors to match one point on the measured polarization curve, a procedure introduced in the previous chapter. The calibrated model then makes a prediction of the whole curve to be compared with experiment results. The asymmetry factors together with other simulation parameters are summarized in Table 4-1.

Fig. 4-5 shows that the comparison is satisfactory. The agreement between experiment and simulation for voltages above 0.4 V is very good. At lower voltages, the predicted current is higher than experimental values probably because of the difference in microstructure parameters (e.g., porosity). These parameters are either estimated or taken from SOFC literature, and may have a relatively large deviation

from their actual values in the SAFC. The prediction accuracy can be further improved after these parameters are known.

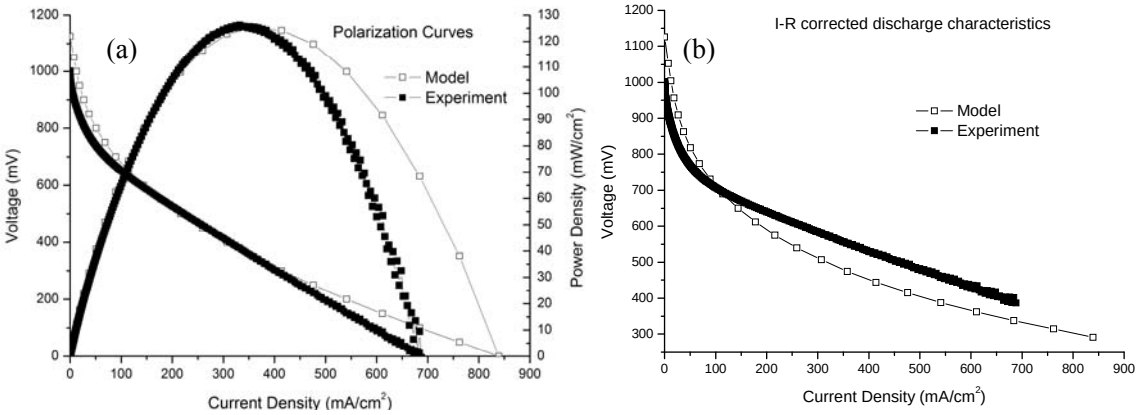

Figure 4-5. Comparison of discharge characteristics of a solid-acid fuel cell. (a) Original (b) I-R corrected

Table 4-1. Parameters for the simulation of a solid acid fuel cell

Parameters	Value	Units
Anode:		
Thickness	100	μm
Porosity	0.5	-
Tortuosity	3.6	-
Average pore radius	0.2	μm
Average particle diameter	1.0	μm
Exchange current density	1.15×10^7	A/m^2
α_a*	0.50	-
α_c*	0.50	-
Cathode:		
Thickness	100	μm
Porosity	0.5	-
Tortuosity	3.0	μm
Average pore radius	0.2	μm
Average particle diameter	1.0	μm
Exchange current density	5.4×10^5	A/m^2
α_a*	0.35	-
α_c*	0.65	-
Electrolyte: $\sigma_i = \sigma_0 T^{-1} \exp(-E_a / R / T)$		
Thickness	100	μm
σ_0	1.258×10^7	S·K/m
E_a	39.3	kJ/mol

Fig. 4-6 and 4-7 show the simulated charge transfer overpotentials at the cathode-electrolyte and anode-electrolyte interfaces respectively. By comparison, it is explicit that the major overpotential falls at the cathode-electrolyte interface, and thus the local heating effect by the charge-transfer reaction should be dominant compared with that on the anode side. On the basis of the good agreement between predicted and experimental I-V characteristics, the model then provides a useful tool to study more

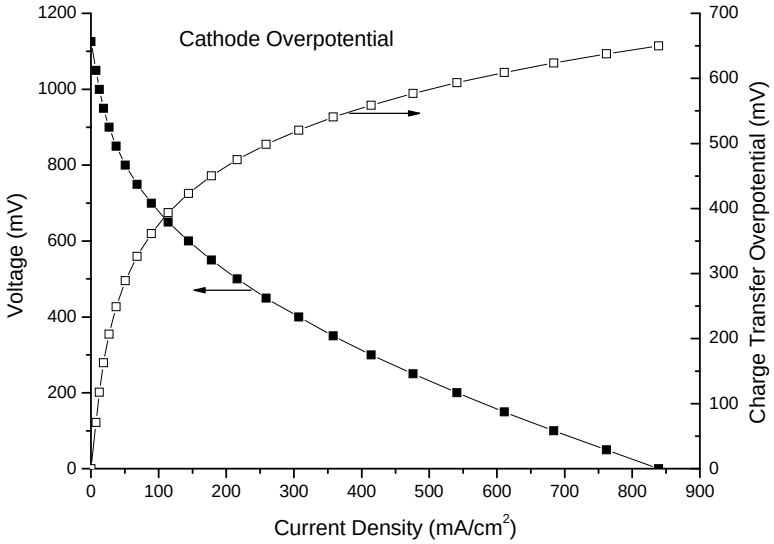

Figure 4-6. Simulated charge transfer overpotential at the cathode-electrolyte interface.

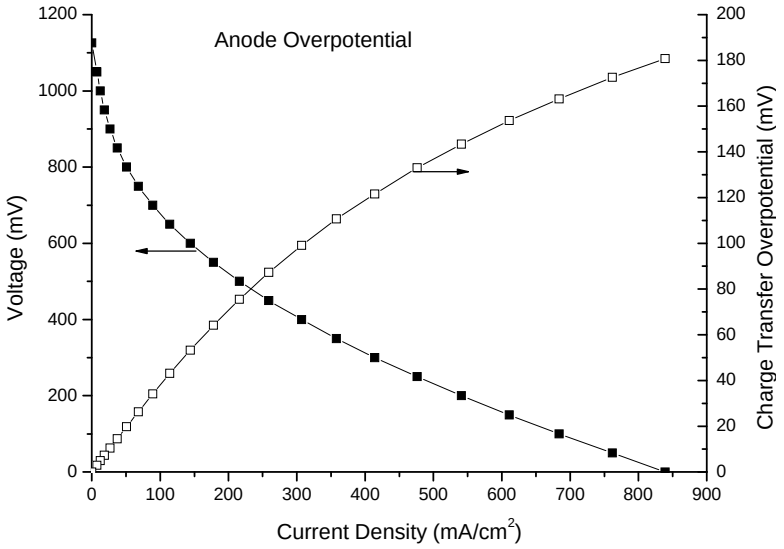

Figure 4-7. Simulated charge transfer overpotential at the anode-electrolyte interface

advanced questions in the SAFC design, such as the heat effect of the charge-transfer reactions. This is future work and will not be discussed here.

Chapter 5
Advanced Topics

5.1 Introduction

Previous chapters presented the theoretical framework of the model and discussed its application in studying the optimization of single-chamber SOFC systems and predicting the discharge characteristics of general dual-chamber fuel cells. Fundamental parameters and processes such as temperature, electrochemistry, and catalytic reaction and transport in porous electrodes (especially the anode for anode-supported type) have proved critical to fuel cell performances, and thus understanding these factors would contribute to future fuel cells with a better design. In particular, there are some issues not covered in previous chapters that are common to more than one type of SOFCs and are important for further research of these fuel cells. Among them, the reactions in the anode in the presence of oxygen (from tiny to large amounts) will be discussed in this chapter; understanding the coupled catalytic oxidation/reforming chemistry and diffusion within the anode can lead to better designs of the anode that better favor hydrogen production in the single-chamber case, and are more coking resistant for SOFCs in general. Detailed structure of the reaction zones in the anode of both single- and dual-chamber SOFCs is presented. Meanwhile, the Cantera-based software approach for better resolving the reaction zone structure without increasing computational cost is also discussed. This general approach also

applies to future study of other important issues, such as the distribution of potential and temperature within the electrodes and the electrolyte of the fuel cell.

5.2 Reactions Zones in an SOFC Anode with Oxygen Addition

Among the components of an SOFC, the anode presents perhaps the most significant technical barrier to creating an efficient, economic, and environment-friendly technology that makes better use of readily available fuels [86]. Ongoing research has been trying to address these issues by seeking anode materials that possess excellent catalytic, electrochemical, and mechanical properties; the nickel-zirconia cermet anodes are currently the dominant SOFC anode due to their structural stability, small thermal expansion mismatch with popular electrolyte materials, and good catalysis to hydrogen oxidation and steam reforming of hydrocarbon fuels [86]. In particular, the anode-supported MEA (membrane-electrolyte assembly) structure is advantageous for hydrocarbon fuels, for it also serves as a reforming or catalytic partial oxidation (CPOX) catalyst in addition to conducting current [3]. However, it is generally not possible to operate nickel-based anodes on higher hydrocarbon-containing fuels because nickel also catalyses the formation of carbon filaments (i.e., coking) from hydrocarbons under reducing conditions [86], and coking can still occur on Ni catalysts even under thermodynamically non-coking conditions [83]. Formation of carbon deposits on Ni particles is responsible for excessively high activation polarization, which leads to the rapid deterioration of cell performance [87]. For example, Zhan et al. reported that the use of iso-octane causes severe coke buildup on

the Ni-YSZ anode and leads to degradation of the anode [83]. Various approaches including steam reforming, addition of oxygen to the fuel stream, and incorporation of dopants into the conventional anode material have been tried in an attemp to mitigate this problem [3, 86].

The oxygen-addition approach is the focus of this chapter. For the purpose of carbon removal, it has the advantage (compared with steam reforming) of working well for both methane and higher hydrocarbons, requiring only a small amount, and not substantially affecting the cell efficiency [83, 86]. For example, Zhan et al. report that a 2% addition to the iso-octane fuel yielded fully stable performance without measurable carbon deposits [83]. While effective for suppressing coke formation for SOFCs in general, mixing oxygen with hydrocarbon fuels and the ensuing catalytic reactions in particular are also the working principles of single-chamber SOFCs (SCFC). More than just the reactant for cathode electrochemistry, oxygen can react with the fuel on the anode side as well, generating hydrogen for anode electrochemistry. Ni-based catalysts have been demonstrated to also exhibit a good activity and selectivity for synthesis gas formation from CH_4/O_2 mixtures [88]. The oxidation of the fuel is exothermic, which can help mitigate the cooling effect of the endothermic reforming reaction in the anode bulk, and in some cases can help maintain the operating temperature [83]. Especially in the presence of a large amount of oxygen (as in the case of SCFCs), the heat release becomes so intense that a substantial temperature rise is usually observed experimentally, which in some cases,

can allow the fuel cell to work steadily without additional external heating (e.g., a furnace) [81].

Despite the possible benefits of oxygen addition, current understanding of the detailed reaction mechanism of oxygen with the fuel species in a typical SOFC anode is rather limited, due to the complexity of the reactions, the lack of experimental diagnostic methods that could resolve the reactions in the microstructure in-situ, and the current focus on steam reforming in numerical modeling studies.

In this chapter, the heterogeneous reactions in the anode of an anode-supported MEA with both large (for SCFC) and small (for dual-chamber SOFC) oxygen addition are studied numerically. Although the oxidation of the fuel in general could occur both in the gas-phase (i.e., homogeneous) and between the gas-phase and the catalyst surface (i.e., heterogeneous) [3], for methane the homogeneous reaction does not play a substantial role for SOFCs until 900^{o}C [54], which is higher than the normal operating temperature of most SOFCs. Therefore, only heterogeneous chemistry is considered here.

In the existing literature concerning using oxygen for coke prevention in SOFC operation, the role of oxygen in the heterogeneous reactions is not clear [83], and in the majority of the SCFC studies, its role is vaguely explained as partially oxidizing the hydrocarbon fuel to produce syngas, without any discussion of the reaction pathway [89]. It is a common practice to use mass spectrometer [83, 90] or gas chromatograph [18] to analyze the outlet gas in an SOFC experiment, which is

necessary but far from being sufficient to determine what reactions are actually taking place in the anode.

Studies using fixed-bed reactors provide some useful insights. DeGroote et al. show the existence of total combustion followed by steam reforming reactions and water-gas shift reaction in a numerical study of catalytic partial oxidation of methane to syngas over nickel [91]. Deutschmann et al. carried out a series of experimental and modeling studies concerning surface and gas-phase chemistry on different catalyst metals in a short-contact-time reactor [60, 88]. From these measurements, they developed a multi-step, elementary reaction mechanism to describe steam-assisted catalytic partial oxidation of methane in small-channel monolith reactors using Ni supported on alumina. This discussion employs the mechanism developed by Deutschmann et al. in [56] to study the anode catalytic chemistry with various oxygen additions under typical SOFC operating conditions. The reliability of the mechanism has been validated by the work of Hecht et al. for dual-chamber SOFC [61], and by the previously published work of this model for single-chamber SOFC [10], for cases with and without oxygen addition in the fuel stream. For the purposes of this study, it is assumed that this reaction mechanism provides an adequate description of the catalytic chemistry within an SOFC anode. The discussion will show that the reactions in the anode are much more complex than a simple, distributed partial oxidation, and that understanding these reactions (including combustion, reforming, and shift reactions) will be helpful in optimizing the anode structure. Although the numerical model was originally developed for single-chamber SOFCs, with the

experimental validation of the simulation results [10] and the good agreement of predicted results with literature (in the previous chapter), useful conclusions could be drawn for dual-chamber cases as well. However, this mechanism was not designed to predict coking, and so in this study, only cases for which coking is not a problem are discussed.

The numerical model developed so far has some particular strength in studying the anode reactions. That is, given a heterogeneous reaction mechanism, not only the distribution of gas-phase and surface-phase species within the porous electrodes can be obtained, but the reaction rates of each species and the heat release rates at every point within the electrode can be calculated. Furthermore, surface reactions can be turned on or off depending on the needs of the study. These features are very useful in studying the catalytic kinetics within the anode with oxygen addition in the fuel stream.

In keeping with previous chapters, the anode and cathode of cells studied here are nickel/YSZ and $Ba_{0.5}Sr_{0.5}Co_{0.8}Fe_{0.2}O_3$ (BSCF), respectively. The electrolyte is either YSZ or $Ce_{0.8}Sm_{0.2}O_{1.9}$ (SDC). The thicknesses of the anode, cathode, and electrolyte are taken to be 700, 10, and 15 microns, respectively, and temperature is fixed at 750^{o}C unless stated otherwise. The cell runs in a mixture of methane and oxygen with specified flow rates, with helium being the balance gas. The flow rate of methane is 87 sccm (ml/min at standard conditions) and the ratio of oxygen to helium is always 1:4. The dimensions of the gas channel are 15.875 mm by 142.875 mm and other details of the computational domain can be found in [10].

First of all, a YSZ cell is simulated in the single-chamber configuration at open-circuit condition. Compared with SDC electrolytes, YSZ is a pure ionic conductor and the rate of electrochemisty at electrode-electrolyte interfaces at all locations along the cell approaches zero under such a condition, thus simplifying the study for the anode reactions by ruling out the influence of electrochemistry. For this case, the fuel-to-oxygen ratio is set at the inlet to be the partial oxidation stoichiometry, i.e., CH_4:O_2:He=2:1:4. The computational grid for the anode is automatically refined by the model, and the finest grid sizes, which occur at the anode-gas and anode-electrolyte interfaces, are around 1μm, enough for resolving the species profiles. The cell is divided into 7 segments of equal lengths along the flow direction, and the central one, which is about 6.7 mm from the fuel cell leading edge, is chosen for analyzing the results.

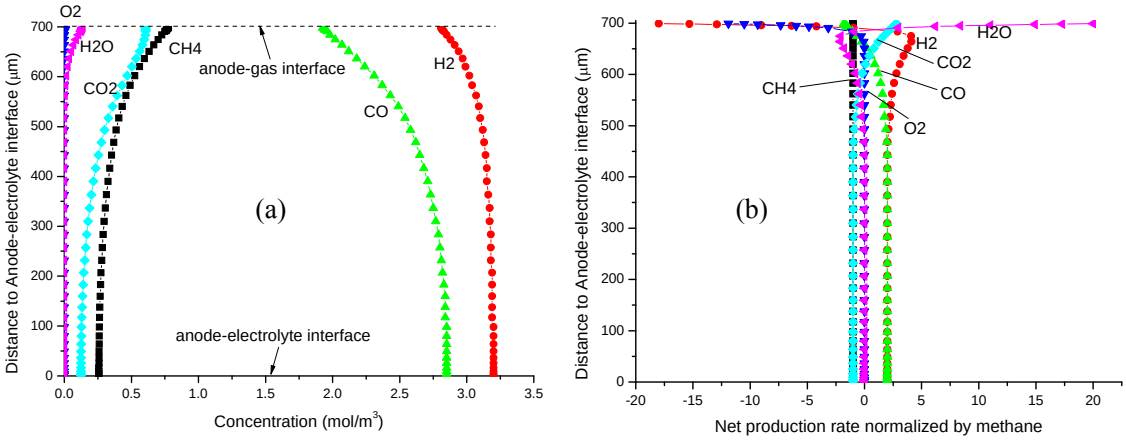

Figure 5-1. Concentration and net production rates of gas species in the anode of a single-chamber SOFC at open-circuit condition

Fig. 5-1a shows the concentration of gas-phase species within the anode. Although the amount of oxygen is half that of methane at the inlet, it is much less over the anode-gas interface due to the catalytic reactions in the anode that will be discussed shortly. It's also obvious that oxygen penetrates into the anode only about

25μm, while methane is abundant throughout the whole anode thickness. The quick depletion of O_2 and the production of H_2O and CO_2 near the anode-gas interface indicate the possibility of combustion instead of partial oxidation or reforming reactions.

A further study of the surface reaction rates reveals a three-layer structure of the anode reactions and confirms the existence of a combustion zone, shown in Fig. 5-1b. All the rates are normalized by that of methane: The production rate of methane is always -1 (minus sign means "consumed"), and the rate for any other species means how many moles of such species are produced for each mole of methane consumed. Starting from the anode-gas interface, 99% of the O_2 is consumed within a 25μm-thick layer by combustion with H_2 and CO produced deeper in the anode, rather than CH_4. At 1μm beneath the interface, for example, the global reaction can be written as $CH_4 + 18H_2 + 1.8CO + 11.9O_2 = 2.8CO_2 + 20H_2O$, and understandably the reaction in this layer is highly exothermic. The heat release of the fuel cell is concentrated in this thin layer and transferred to the other parts through conduction. The methane partial oxidation claimed in literature is unlikely to occur because nickel is an excellent catalyst for the oxidation of hydrogen (1), and in the presence of a large amount of syngas (as reported in literature), it is impossible for O_2 to selectively react with CH_4 but not with either H_2 or CO.

The syngas consumed in the combustion zone is generated by the reforming zone extending roughly from 25 to 200μm away from the anode-gas interface, into which the H_2O produced in the combustion layer diffuses and reacts with methane. H_2O is

depleted in this layer; in the third layer that immediately follows, which extends up to 500μm above the anode-electrolyte interface, the syngas is produced by methane and CO_2 from the combustion layer, and the global reaction can be written as $CH_4 + CO_2 = 2CO + 2H_2$.

The three-layer structure of the anode is in general agreement with the indirect route of the syngas production suggested by Ishihara et al. [88] in the study of methane partial oxidation with oxygen permeating ceramic membrane reactors, for which combustion of CH_4 to CO_2 and H_2O is followed by reforming reaction of CH_4 with H_2O and CO_2 –CO and water–gas shift conversions. The 25μm-thick combustion layer mimics the reactor entrance, where an extremely rapid variation of temperature, velocity, and transport coefficients occurs [88]. The heat release in this layer not only provides the heat for the endothermic steam reformation [3], but also leads to a significant temperature rise, verified both experimentally by several groups [19, 24, 27, 81] and numerically as discussed in Chapter 3.

However, one major difference between the reactor and an SOFC anode is the contribution of steam by electrochemistry. Because H_2O plays an important role in both reforming and water-gas shift reactions, the layered structure of the anode in the presence of electrochemical reactions can be different and needs a further study. Therefore the load potential is changed to 0.5 V (for maximum power output) and the results are shown in Fig. 5-2. By comparison, a large amount of H_2O is produced by electrochemistry, providing enough steam for the reforming of methane and the water-gas shift reactions. As a result, the concentration of methane decays more

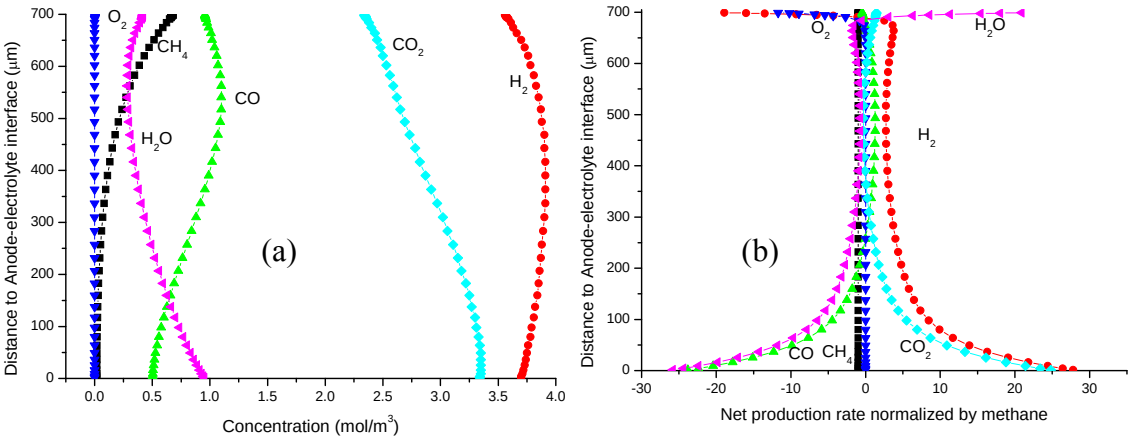

Figure 5-2. Concentration and net production rates of gas species in the anode at 0.5 V

rapidly with depth into the anode, and the concentrations of hydrogen and CO_2 are higher, while that of CO is considerably lower compared with the open-circuit case. The similarities include the combustion layer of ~ 25μm thick and the reforming layer, with thickness extending from 175 to 475 μm due to the higher concentration of H_2O. As for the third layer, not only does the thickness reduce to ~200 μm, but the dominant reaction is water-gas shift, also due to the presence of H_2O.

In Fig. 5-2, it's interesting to notice that there is a minimum for H_2O at ~ 600 μm and a maximum for H_2 at ~ 400 μm. A calculation of mass fluxes of species shows that the steam produced by the combustion layer never goes downwards beyond the 600 μm line, and the H_2 and CO generated by this part of the steam diffuses back to be fully oxidized. On the other hand, the steam generated by electrochemistry goes upwards to the 600 μm line. The H_2 it generates through reforming partly diffuses to the combustion layer, and partly diffuses back to the anode-electrolyte interface, where it is converted to H_2O again. This means that the H_2 for electrochemistry is not directly relevant to the oxidation of methane, but is solely produced by internal reforming. The major role of O_2 is supplying the heat to steam reforming by way of

full oxidation of the syngas. The combustion makes the gas mixture in the flow channel increasingly fuel-rich so that more oxygen is needed by the downstream part of the fuel cell, shifting the optimum fuel-to-oxygen ratio towards the fuel-lean condition, as discussed in Chapter 4. The working principle of SCFC cannot be simply explained as the partial oxidation of methane, nor does it make sense to superpose the local reactions to get some nominal "global" reaction for the whole anode, because different regions of the anode are responsible for different functionalities.

The three-layered structure of the anode exists for a wide range of operation parameters including voltage (0 volt to open-circuit), temperature (550 – 800^{o}C at least) and the fuel-to-oxygen ratio (0.5 to 2.0 at least), and the general pattern is the same. However, there are quantitative differences depending on specific conditions. For example, at lower voltages (e.g., short-circuit), methane is depleted faster due to the higher concentration of H_2O produced by electrochemistry, and therefore the reforming layer is narrower, while the water-gas shift layer is wider; at smaller fuel-to-oxygen ratios (e.g., stoichiometry for methane combustion), the combustion layer can be much wider due to the abundant oxygen, resulting in a very low H_2 concentration and power output. As for temperature, although the Deutschmann mechanism does not apply above 800^{o}C, it can be inferred that the combustion layer will become wider with temperature because the selectivity of the nickel anode goes down, which could result in a loss of power output. One example is Hibino's earlier study of SCFC [11, 15, 74], in which the furnace temperature is 950^{o}C and the fuel

cell temperature should be well above 1000°C. The low power output should be partly accounted for by the combustion layer under such high temperatures.

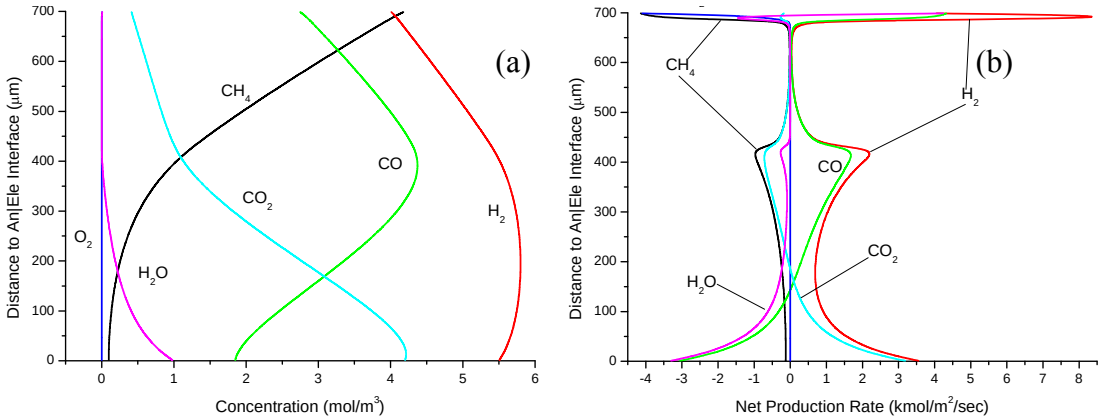

Figure 5-3. Concentrations and net production rates of gas-phase species in a dual-chamber SOFC anode

Besides the single-chamber case, the dual-chamber SOFC in a button cell configuration (Fig. 4-1) is also investigated with 5% addition of oxygen in the methane fuel stream in the anode chamber at 800°C. Although the Deutschmann mechanism is not designed to predict coking, this study will certainly bring more insights into the role that oxygen plays in preventing coking. The cathode chamber is supplied with air at a flow rate of 250 sccm. Load potential is 0.5 V, and all other parameters are the same as the single-chamber case. Fig. 5-3 shows the species profile and net production rates along the centerline in the button cell. In this case, the anode structure is more complicated than the single-chamber case. One major difference is that there is no combustion layer. Starting from the anode-gas interface, there is a very thin layer of ~ 5 μm in which methane is partially oxidized by ambient O_2 to syngas and water, and the heat release is positive. This process quickly depletes most of the oxygen entering the anode, and the water and CO_2 produced by this oxidation enables

reforming of the methane to occur in the next 15 μm or so. The water production rate changes from positive to negative, and the CO_2 rate is also negative, while H_2 and CO are being produced. In this region, the heat release is negative. From 650 μm to 450 μm, no significant reaction happens because H_2O generated by the partial oxidation is consumed. From 450 μm to 400 μm, CH_4 and CO_2 start to be consumed again and syngas is produced, but the concentration of H_2O is still close to zero in this region. Therefore the reaction is "dry" reforming. The layer between 400 μm and 100 μm is a regular reforming region, in which H_2O produced by electrochemistry converts CH_4 to syngas. Finally, in the last 100 μm before the electrolyte, methane is almost depleted, and the dominant chemistry is water-gas shift, with the steam coming from the electrolyte and the CO coming from the dry-reforming and regular reforming layers above.

Compared to the case with no oxygen addition, the presence of oxygen generates heat and steam within the 20 μm layer beneath the anode-gas interface. The increase of cell temperature due to the heat release and the steam reforming of methane are both beneficial to prevent coking. Also, the power output is not influenced because the amount of oxygen is too small. As discussed in the previous chapter, 10 vol% oxygen is needed to reduce the power output by 1.5%, thus validating the conclusions of Zhan et al. [83].

5.3 Simulation of Multi-layer Electrodes

For the purpose of improving SOFC performance or reducing coking, some groups have suggested the possibility of a composite anode, and positive results have

been reported [83, 92]. Correspondingly, the model is upgraded to simulate a multi-layer anode, each layer with different microstructures and metal catalyst, and with computation mesh automatically refined (discussed below).

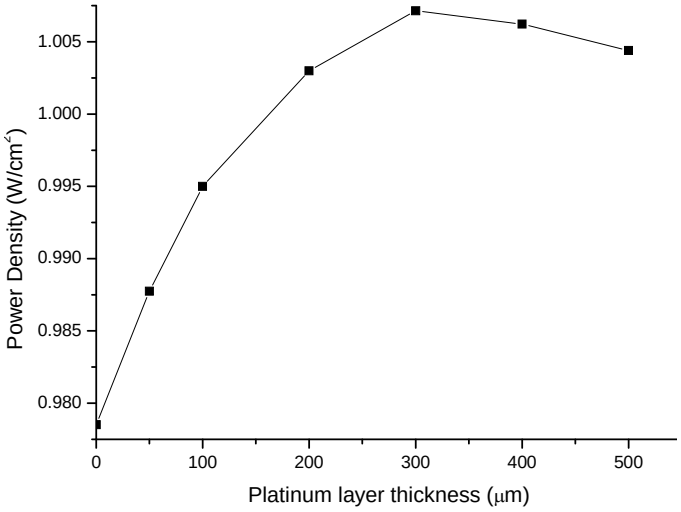

Figure 5-4. Maximum power density of a single-chamber SOFC with Ni-Pt composite anode versus Pt layer thickness

The simulation of the multi-layer electrodes requires a change of solution structure based on Cantera. As discussed in Chapter 2, the electrode layers are defined as bulk domains and the electrolyte is a connector domain. The difference between these two types of domains is that the former can be discretized with computational grids while the latter cannot. For multi-layer electrode simulation, one bulk domain is needed for each layer, and two adjacent layers are connected by a connector domain as shown in Fig. 5-4. The difficulty with such simulations is the match of dusty-gas model (DGM) fluxes of gas-phase species at the interface between each two electrode layers. Due to the requirement to keep the Jacobian matrix corresponding to the global solution vector banded, the control volume of one electrode layer on one side of the interface cannot directly use the solution values on the control volume across the

interface in the other electrode layer. As a result, the connector domains are necessary to separate the layers. The unknowns defined within each connector domain are the DGM fluxes of all gas-phase species evaluated with the states of the gas mixture on either side of the interface.

When evaluating the Jacobian matrix for all the nonlinear equations being solved over the MEA domain, Cantera calculates the residual of each equation by iterating over the whole MEA domain in two passes: first over the bulk domains during which only the solution corresponding to the bulk domains are perturbed, and second over the connector domains over which only the solution corresponding to the connector domains are perturbed. The part of the residual of the bulk domain related to the interfacial mass fluxes is not evaluated until the second pass. This ensures that the mass fluxes across the boundary are unique and computed correctly.

Next, an example is discussed to show the application of the upgraded model. An SCFC with the anode composed of two different layers of metal is simulated at 750^{o}C. The thicknesses of both layers changes, with the total thickness fixed at 700 μm. Combinations among Ni, Rh, and Pt are attempted, and in most cases deliver worse performance than the monolayer nickel anode of 700 μm. However, the composite anode with platinum on the gas side and nickel on the electrolyte side is slightly better, as shown in Fig. 5-5. The highest power is 3% higher than the monolayer anode case, and the corresponding platinum layer thickness is 300 microns. The possible reason is that platinum is a better catalyst for syngas combustion than it is for CH_4 combustion, and it is not a good catalyst for CH_4 reforming, so that more CH_4 is saved in the

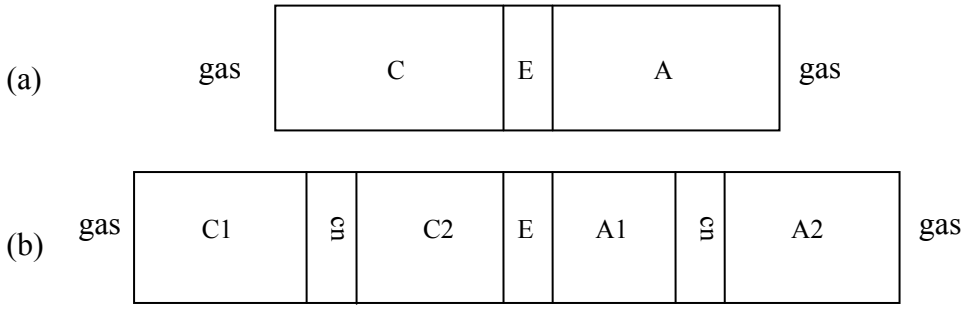

Figure 5-5. Schematic illustration of the computational domain of an MEA with (a) single-layer electrodes and (b) multi-layer electrodes. A, C, E stands for anode, cathode and electrolyte respectively; cn stands for connector domains

combustion layer for the production of H_2 in the nickel layer for electrochemistry. This topic will be discussed in more detail in a future paper.

5.4 Automatic Refinement of the 1-D Computation Grid in the MEA

For the discussions about the reaction zones in the anode (both single- and multi-layer) above, the automatic refinement feature of Cantera for the computation grid within each layer of the electrode is employed. The refinement is necessary because catalytic reaction rates and heat release rate at the electrode-gas are so high that a uniform grid either does not have enough resolution to reveal enough details of the thin reactive layer beneath the interface, or satisfies the resolution requirement at the cost of increasing the number of grid points at regions where refinement is not necessary, leading to dramatic increase of computation expenses.

The automatic refinement process starts with an initial grid that can be non-uniform, and only refines regions where the change of some variable is above some user-specified threshold. The variables include the ratio of species concentrations, the slope of the species' concentration profile, and the curvature of the profile between

two adjacent grid points. However, the automatic refinement has some limitations for the control-volume approach. Since this method works by inserting a new grid point wherever refinement is necessary, and since the unknown variables are defined at the center of each control volume, the space between the first grid point and its adjacent boundary cannot be refined afterwards, and likewise for the last one. Therefore, for the study of the reaction zones in the anode, the initial grid needs to be refined at both the anode-gas and anode-electrolyte interfaces, in order to resolve well the full oxidation reaction and possible reactions induced by water from electrochemistry. A cosine distribution of the grid spacing is used for this purpose, and the smallest grid resolution of grid point numbers of 9, 19, and 29 correspond to a uniform grid with 20, 100, and 200 points respectively.

5.5 Concluding Remarks

Through simulation of an SOFC anode with oxygen addition, it is found that three distinct regions exist: starting from the anode-gas interface a thin outer layer in which oxygen is nearly fully consumed in oxidizing methane and hydrogen, followed by a reforming region, and then a water-gas shift region deep within the anode. The results indicate that partial oxidation of methane is unlikely to be the major contributor to either sygnas production or cell heating. Rather, the hydrogen for electrochemistry is mostly produced by internal reforming even in the presence of abundant oxygen (i.e., the single-chamber cases), and cannot be explained by a simple, global partial oxidation reaction. The heat effect is mainly due to the full rather than partial

oxidation of both syngas and methane even under fuel-rich conditions. Based on these understandings and the automatic refinement of the computational grid, the possibility of a composite anode with different layers of metal catalysts is explored, and a Ni-Pt composite anode is found to deliver a better performance than a monolayer Ni anode.

Chapter 6
Conclusions and Future Work

6.1 Conclusions

A two-dimensional numerical model for simulating the single-chamber solid oxide fuel cell (SCFC) system has been developed. The model is based on first principles governing fuel cell operation from the microscopic level in the membrane electrode assembly up to the macroscopic level in the channel flow of gas mixture. It is the first model to simulate the stacked SCFC in both single- and multiple-cell configurations. The model is comprehensive in the sense that it involves different modules corresponding to the important processes responsible for various aspects of fuel cell operation and performance. The particular strength of the model is the capability to simulate different geometries in the flow channel and the catalytic surface chemistry in the anode of solid oxide fuel cells, both of which have significant influence on SCFCs.

Model calibration with experimental data is a necessary step to connect this theoretical framework to reality and make quantitative predictions. The process first minimizes the degree of freedom by adopting as many directly or indirectly measured parameters as possible, and then fits the unknown parameters by fitting to measured data under different operating conditions. The fact that the predicted results of the calibrated model show good agreement with experimental results indicates that the model captures the most important factors in the single-cell SCFC system developed

jointly (Haile group) in the same project, and that the calibration process is reliable. Although the actual device is 3D, for those running under typical conditions introduced in the thesis, the 2D model is sufficient, and the possible reason is that the spatial flow speed is high enough to reduce the effects (such as lateral diffusion) in the third dimension significantly.

Based on the experiment-verified model, several important open questions in SCFC development are explored numerically, and useful insights are obtained. Generally speaking, the electrical performance of the SCFC is eventually decided by electrochemistry at the electrode-electrolyte interfaces, and analysis of various factors should be centered on this. The optimal fuel-to-oxygen ratio is found to be an average result of its local value along the fuel cell, and is influenced by many factors. Flow geometry is a particularly sensitive one among them. The reorientation of the cell results in significant change in the ratio by improving the oxygen distribution along the cell and thus improving the exchange current density. Other parameters—including catalyst activity, electrode microstructure, and temperature—although they may not be as sensitive, influence the ratio in a similar way by eventually affecting the concentrations of H_2 and/or O_2 at the anode- and cathode-electrolyte interfaces respectively.

Another major concern in SCFC design, as in any other fuel cell system, is power output and efficiency. As discussed in Chapter 3, the efficiency of SCFC is generally low due to the large amount of reactants that bypasses the MEA. However, unlike the conventional dual-chamber SOFCs which are used for relatively large-scale stationary

power generations, the SCFCs are designed for portable power generation applications (see Appendix A) and the major goal is to compete with present-day lithium batteries. Even with an efficiency of ~10%, the power generation capability of SCFC systems can still be highly attractive for practical applications due to the high energy density of the hydrocarbon fuels that they operate with.

Possibilities to improve power generation are explored based on the available experimental data within the current theoretical framework (e.g., the heterogeneous reaction mechanism of the anode). Since the fuel cell under discussion is anode-supported, more focus is placed on the anode side. The approaches to improving power generation work by reducing losses (overpotentials) at different parts of the MEA and can be largely grouped in four categories.

The first category reduces the mass transfer overpotential by making improvements to the diffusion of gas-phase species from the flow channel to the electrode-electrolyte interfaces. For the anode in particular, reducing the anode thickness has proved effective based on simulation results, since it shortens the diffusion path. On the other hand, improving the effective diffusion coefficient is also effective. This can be achieved by improving the porosity, reducing the tortuosity of the porous electrode, and/or improving the binary diffusion coefficient of the gas mixture by way of using helium instead of nitrogen as the balance gas.

The second category targets the charge transfer overpotential, which can be reduced by improving the exchange current density. Computation results show that the electrode-electrolyte interface with a smaller anodic asymmetry factor incurs

higher overpotential; thus increasing its exchange current density will lead to a more significant reduction.

The third category focuses on reducing the ohmic resistance, and the common practice is to use a thin layer of MIEC instead of pure ionic conductor as the electrolyte, and to support it on one of the electrodes. However, the operating condition of the cell must be carefully managed since the total power output can suffer a significant drop due to the reverse electronic current, which goes up dramatically with the increase of temperature and the decrease of oxygen partial pressure.

The fourth category for improving fuel cell power generation is by making a better use of the gas reactants. This includes the management of flow geometry by either reducing the width of the flow channel, or reorienting the cell and increasing the total number of cells. Using a narrower channel accelerates the flow speed and improves the power output for both single cells and cell arrays. The perpendicular orientation of the fuel cell, although having the potential of a higher power density, is possibly not an ideal geometry for considerations of total power output because of limitations on total area. Increasing the number of fuel cells is an effective way to enhance the fuel utilization and total power generation, but it puts more challenges to flow geometry design. In general, harmful fuel cell positions, including those throttling the gas supply to either of the electrodes and those promoting harmful parasitic reactions in the cathode, should be avoided. Furthermore, the usage of multiple cells is effective only when the gas flow rates are high enough for the

transport limitation to go away. When the total flow rate is low, the power generation of the fuel cell is dominated by gas diffusion in the flow channel, and the small total energy input into the system results in poor power generation, although the fuel cell efficiency might be high. Due to this reason, the fuel cell efficiency (and possibly fuel utilization) needs to be considered together with the total power output in practical applications, and a compromise is often needed for both numbers to be relatively high. Besides these four categories, some other factors such as electrode selectivity and temperature are also important for the fuel cell power output. Highly selective and reactive electrode catalysts with enough surface reaction sites are ideal. Temperature needs to be controlled within a reasonable range and the range depends on the type of electrolyte and the inherent electrochemical characteristic of the exchange current densities.

The model is also updated to simulate other fuel cells with different geometry and/or electrolyte, and good agreement between predicted results and experimental/literature results is also achieved. This proves that the theoretical framework of the 2D model adequately describes the important processes in the operation of the fuel cells simulated, and that the calibration process based on actual measurements is effective.

Despite the positive comparison between modeling and experiment, the results predicted by the model may not be precise, partly because the model is based on many simplification assumptions, and partly because of the uncertainties in experimental measurements, especially for the quantities obtained indirectly (e.g., by estimation).

Therefore, predicted trends are more important than numerical values. Also, one should not extrapolate too far out of the parameter space in which the model is designed. For example, the upper limit of the temperature at which the model can be applied depends on the temperature limit of the anode reaction mechanism and the assumption that gas-phase chemistry is not significant.

Compared with experiments, the particular attractive feature of this model is not only the efficiency and systematicness in SCFC design and optimization research, but also the capability to explore realms unachievable by existing experimental techniques, such as "probing" a designated location in the porous electrode. Furthermore, the numerical model has a complete control of processes, and artificial management is often possible to help with understanding the phenomena. For example, a specific reaction in the anode can be turned on or off and the rate can be adjusted to investigate the role of the reaction for fuel cell performance.

Although simulation gives qualitative guidance to experiment, it depends on the availability of experimental data and the correct formulation of the physical and chemical processes. Therefore, modeling and experimental study of SCFC need to work in a loop for a faster convergence on the optimal design and the acceleration of the design cycle.

6.2 Future work

Based on the discussion in this thesis and conclusions above, the following areas can be suggested for future study:

First, the experiment-validated model should be used to study broader and more advanced mechanistic issues of SCFC systems and possibly other types of fuel cells. The simulation of a two-layer anode with different catalyst metals is one example. For SCFC systems in particular, the sensitivity analysis of (fuel cell power to) materials' properties is also important but has not been systematically studied. Further investigation into such areas will lead to deeper understandings and more insights for the improvement of fuel cell performance.

Second, simulation of electrochemistry can be improved by modeling the charge transfer reactions at triple-phase boundaries in the bulk of the porous electrodes rather than just at the electrode-electrolyte interfaces. It has been pointed out in this thesis that the latter could be an oversimplification for thin electrodes. Models of electrochemistry on the micro-particle level being developed in the group can be incorporated with this model.

Third, for the study of more realistic SOFC systems the model needs to adopt the heterogeneous catalytic reaction mechanism of higher hydrocarbons and possibly gas-phase chemistry. This study uses methane as the fuel for simplicity, but literature shows more interest in higher hydrocarbons ranging from C_3 to C_8, which have a less stable structure than methane and thus a lower operating temperature. The cost for simulating SOFC systems with higher hydrocarbon fuels is the dramatic increase in the number of species and reactions, and possibly the numerical stiffness introduced by the gas-phase reactions. Therefore, more efficient computation (e.g., parallel computing) might be needed.

Fourth, geometric capability needs to be enhanced. Besides the stacked MEA that the model simulates, there are two other important geometries that the model has not been able to. One is the tubular fuel cells. For simulation of a single tubular cell, a 2D model is sufficient, and it only requires the reformulation of the governing equations in the cylindrical coordinate. However, for the simulation of a fuel cell stack, the model needs to be upgraded to 3D. The other geometry is the strip configuration of SCFC, in which the two electrodes are on the same side of the fuel cell. An upgrade in the electrolyte module is needed to resolve the electrical potential distribution in the electrolyte, and an upgrade of the flow model to 3D is needed to resolve the transport of gas phases in the flow channel. These upgrades will also benefit the simulation of other fuel cells. For example, the resolution of potential distribution in the electrolyte is helpful to simulate the temperature distribution within the MEA of the solid acid fuel cell, and the 3D model will prove useful when the 3D effects in a fuel cell system are important (such as when flow speed is low in a SCFC system). These upgrades will also result in a dramatic increase in the computation cost. Correspondingly, approaches such as parallel computing and faster solvers for matrix equations should be adopted.

Appendix A

The Integrated Micro-Power Generator

Compared with conventional dual-chamber SOFCs, single-chamber SOFCs have some unique advantages that make them particularly attractive for some applications—notably for micro-scale or portable power generation, an area in which the conventional SOFC technology is very difficult to apply. While the power density and efficiency are typically lower, SCFCs do not require seals, and allow a very simple gas manifold design. This, in turn, leads to fabrication simplifications and improvement of resistance to both mechanical shocks (due to vibration, collision etc) and thermal shocks (due to rapid changes in temperature), thereby enabling rapid start up and shut down. In addition, the temperature-rise effect in the SCFC anode makes it possible for micro-SCFC systems to be thermally self-sustaining [81], such that no external heat source is required for fuel cell operation. The mechanical and thermal characteristics of SCFC make it very suitable for portable-power generation applications.

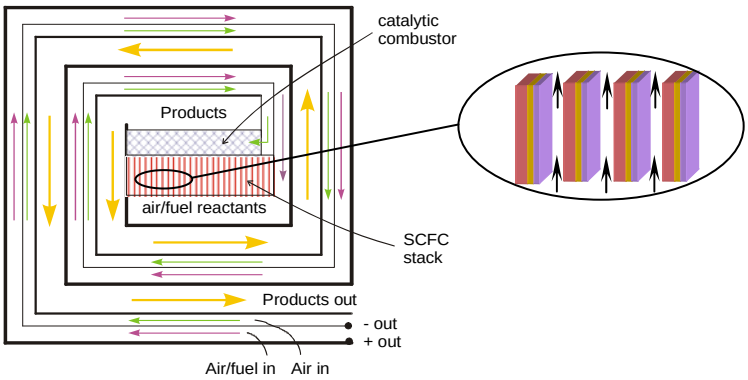

Figure A-1. The Integrated Micropower Generator (IMG)

On the other hand, although present-day lithium batteries can satisfy the power needs of portable electronics, their power densities, particularly when operated at the discharge rates required to obtain these power densities, are unacceptably low, permitting battery-powered microdevices to be operated only for extremely limited periods of time. In contrast to batteries, which have energy densities of approximately 160 Wh/kg (350 Wh/l), liquid hydrocarbon fuels carry exceptionally high energy densities: 10 – 15k Wh/kg or 7 – 10k Wh/l. Thus, technologies which take advantage of the inherently high energy densities of such fuels are ideal for micropower generation.

For these reasons, a joint project was funded by DARPA to design an integrated micro-power generator (IMG) based on the SCFC technology. As shown in Fig. A-1, the IMG involves an SCFC stack at the center, surrounded by the so-called Swiss-roll heat exchanger [93]. The fuel cell is used in stacks in order to improve the utilization efficiency of the fuel and increase the total power output. The mixture of fuel and air comes in from one channel of the heat exchanger, and the fuel cell stack generates power as the mixture flows past them, with the exhaust gas burned by a catalytic afterburner to reduce emission to the ambient and maintain the temperature of the whole device. In addition to being a gas conduit, the major functionality of the heat exchanger is to minimize the heat loss of the device to the environment, a critical issue for small-scale power generators because the heat loss rate to the environment increases as the characteristic length of the generator decreases. This is achieved by making the walls with polished titanium plates to reflect the thermal radiation back,

and heat up the incoming cold gas mixture with the hot outgoing exhaust. The metal wall of the heat exchanger also conducts the electrical current to the external load circuit.

Appendix B

Comparison of Mass Fluxes Due to Mass Diffusion and Thermal Diffusion

In equation (2.22), the diffusive mass flux $\underline{j}_k$ involves two terms: the mass diffusion flux

$$\underline{j}_{k,m} = -\rho D_{k,m} \nabla Y_k \tag{B.1}$$

and the thermal diffusion flux

$$\underline{j}_{k,t} = -(1/T) D_k^T \nabla T \ . \tag{B.2}$$

A comparison between these two terms is necessary to simplify $\underline{j}_k$ in order to eventually simplify both the energy equation (2.9) and the species mass conservation equation (2.10).

For the geometries shown in Fig. 2-1, it is found both experimentally and numerically that the component of the gradient terms ∇Y_k (equation B.1) and ∇T (equation B.2) perpendicular to the fuel cell is much higher than the component in the parallel direction due to reactions in the fuel cell. So a quantitative comparison between the two fluxes can be simplified as the comparison between the maximum norms of the two fluxes. The maximum norm of a vector $\underline{x}$ with n components $x_1, \cdots, x_n$ is defined as

$$\| x \|_\infty = \max(|x_1|, \cdots, |x_n|) \ . \tag{B.3}$$

The comparison of the two fluxes is quantified by the ratio of the maximum norms

$$r_k = \frac{\|j_{k,m}\|_\infty}{\|j_{k,t}\|_\infty} = \frac{D_k^T}{T}\left|\frac{\partial T}{\partial y}\right| \Big/ \left(\rho D_{km}\left|\frac{\partial Y_k}{\partial y}\right|\right) \approx \left|\frac{D_k^T}{T\rho D_{k,m}}\frac{\Delta T}{\Delta Y_k}\right| . \qquad \text{(B.4)}$$

The mass diffusion coefficient $D_{k,m}$ and thermal diffusion coefficient D_k^T are calculated by Cantera [68] with a python script (listed at the end of this appendix). Since the order of magnitude of the ratio is more important than the specific numerical value, $\Delta Y_k = 1$ can be used as a good approximation in (B.4). The temperature T and temperature difference ΔT are taken to be 750°C and 100°C, respectively, which are typical values for SCFC systems in experimental literature [10]. The numerical solution of the gas molar concentration in the flow channel is used for an accurate calculation of the ratio defined in (B.4). Four locations—including the inlet, outlet, anode-gas interface, and cathode-interface—are selected. The ratio is calculated for carrier gases He and N_2, respectively. The gas flow rates at the channel inlet are CH_4:O_2:N_2 = 87:80:320 sccm.

Table B-1. Comparison of $D_{k,m}$ and D_k^T at the gas channel inlet (N_2)

	Conc. (mol/m^3)	$D_{k,m}$ (m^2/sec)	D_k^T (kg/m/sec)	r_k
CH_4	2.12780	2.18E-04	-1.12E-09	1.89E-06
H_2	0	7.71E-04	-1.05E-06	5.04E-04
CO	0	1.99E-04	1.44E-07	2.67E-04
O_2	1.95660	2.03E-04	4.13E-22	7.50E-19
CO_2	0	1.59E-04	5.25E-07	1.22E-03
H_2O	0	2.61E-04	-2.92E-07	4.13E-04
N_2	7.82638	1.81E-04	6.79E-07	1.38E-03

Table B-2. Comparison of $D_{k,m}$ and D_k^T at the gas channel outlet (N_2)

	Conc. (mol/m^3)	$D_{k,m}$ (m^2/sec)	D_k^T (kg/m/sec)	r_k
CH_4	1.61132	2.18E-04	-1.11E-09	1.88E-06
H_2	0.367249	7.71E-04	-1.05E-06	5.03E-04
CO	0.0123147	1.99E-04	1.44E-07	2.67E-04
O_2	1.15316	2.03E-04	-1.38E-22	2.50E-19

CO_2	0.471521	1.59E-04	5.26E-07	1.22E-03
H_2O	0.589854	2.61E-04	-2.92E-07	4.13E-04
N_2	7.70562	1.81E-04	6.76E-07	1.37E-03

Table B-3. Comparison of $D_{k,m}$ and D_k^T at the anode-gas interface (N_2)

	Conc. (mol/m^3)	$D_{k,m}$ (m^2/sec)	D_k^T (kg/m/sec)	r_k
CH_4	0.432097	2.00E-04	-5.07E-11	8.16E-08
H_2	0.805734	6.86E-04	-4.99E-07	2.34E-04
CO	0.0412202	1.82E-04	1.60E-08	2.83E-05
O_2	0.184511	1.85E-04	0.00E+00	0.00E+00
CO_2	1.82900	1.40E-04	1.04E-06	2.39E-03
H_2O	1.64991	2.42E-04	-5.90E-07	7.86E-04
N_2	6.96856	1.83E-04	3.27E-08	5.77E-05

Table B-4. Comparison of $D_{k,m}$ and D_k^T at the cathode-gas interface (N_2)

	Conc. (mol/m^3)	$D_{k,m}$ (m^2/sec)	D_k^T (kg/m/sec)	r_k
CH_4	2.24992	2.29E-04	-4.43E-08	7.71E-05
H_2	0.0458024	8.20E-04	-1.38E-06	6.70E-04
CO	0.000456491	2.06E-04	2.91E-07	5.62E-04
O_2	1.03415	2.13E-04	1.80E-22	3.38E-19
CO_2	0.0155407	1.71E-04	3.97E-08	9.27E-05
H_2O	0.104844	2.71E-04	-1.84E-08	2.71E-05
N_2	8.46032	1.68E-04	1.11E-06	2.64E-03

Similarly, the comparison can be performed with He being the carrier gas. The flow rates are the same. The results are shown in the following four tables.

Table B-5. Comparison of $D_{k,m}$ and D_k^T at the gas channel inlet (He)

	Conc. (mol/m^3)	$D_{k,m}$ (m^2/sec)	D_k^T (kg/m/sec)	r_k
CH_4	2.12758	3.81E-04	2.69E-09	6.44E-06
H_2	0	1.16E-03	-1.52E-06	1.19E-03
CO	0	3.25E-04	2.87E-06	8.03E-03
O_2	1.95640	3.80E-04	-1.06E-21	2.53E-18
CO_2	0	2.76E-04	2.51E-06	8.29E-03
H_2O	0	4.61E-04	8.44E-07	1.67E-03
He	7.82397	1.30E-03	-4.71E-06	3.29E-03

Table B-6. Comparison of $D_{k,m}$ and D_k^T at the gas channel outlet (He)

	Conc. (mol/m^3)	$D_{k,m}$ (m^2/sec)	D_k^T (kg/m/sec)	r_k
CH_4	1.44637	3.81E-04	2.68E-09	6.39E-06
H_2	0.454488	1.16E-03	-1.51E-06	1.19E-03
CO	0.0189840	3.25E-04	2.88E-06	8.07E-03

O_2	0.886499	3.80E-04	-4.75E-21	1.14E-17
CO_2	0.622273	2.76E-04	2.52E-06	8.31E-03
H_2O	0.790069	4.62E-04	8.39E-07	1.65E-03
He	7.69236	1.30E-03	-4.73E-06	3.30E-03

Table B-7. Comparison of $D_{k,m}$ and D_k^T at the anode-gas interface (He)

	Conc. (mol/m^3)	$D_{k,m}$ (m^2/sec)	D_k^T (kg/m/sec)	r_k
CH_4	0.451057	3.14E-04	3.85E-11	7.60E-08
H_2	1.08166	9.76E-04	-8.69E-07	5.53E-04
CO	0.0537532	2.90E-04	1.00E-06	2.15E-03
O_2	0.156023	3.05E-04	8.52E-22	1.73E-18
CO_2	2.08069	1.98E-04	3.82E-06	1.19E-02
H_2O	1.94948	3.85E-04	5.77E-07	9.31E-04
He	6.13837	1.11E-03	-4.53E-06	2.54E-03

Table B-8. Comparison of $D_{k,m}$ and D_k^T at the cathode-gas interface (He)

	Conc. (mol/m^3)	$D_{k,m}$ (m^2/sec)	D_k^T (kg/m/sec)	r_k
CH_4	2.12702	4.22E-04	1.41E-07	3.93E-04
H_2	0.0811603	1.28E-03	-1.89E-06	1.73E-03
CO	0.00156389	2.90E-04	5.42E-06	2.19E-02
O_2	0.943687	4.28E-04	1.27E-21	3.48E-18
CO_2	0.0447237	3.48E-04	3.15E-07	1.06E-03
H_2O	0.233070	5.29E-04	1.23E-07	2.72E-04
He	8.47981	1.32E-03	-4.11E-06	3.64E-03

Based on the calculations, it can be concluded that under typical operating conditions of SCFC systems, the thermal diffusion flux is at least two orders of magnitude smaller than the mass diffusion flux, and so dropping this term will not introduce significant numerical error.

The python script for the calculations of diffusion coefficients is as follows:

```
from Cantera import *

T0 = 750.0+273.15 # operating temperature
dT = 100 #temperature difference
g = IdealGasMix('acgas_he.cti') #create gas mixture
nm = g.speciesNames()
```

```
fn = []
X = []
inpdir='inp\\'
outdir='out\\'
fn[0]='inlet'
fn[1]='aboveMEA'
fn[2]='belowMEA'
fn[3]='outlet'
ext1='.txt'
ext2='.csv'
for i in range(len(fn)):
    f = file(inpdir+fn[i]+ext1,'r')
    X[i] = f.readline()
    f.close()

for i in range(len(X)):
    f = file(inpdir+fn[i]+ext1,'r')
    X[i] = f.readline()
    f.close()
    # END of the input section

    # Process the inlet
    print 'Processing '+fn[i]+ext2
    g.set(T = T0, P = OneAtm, X = X[i])
    g.equilibrate('TP')

    rho = g.density()
    massDiff=g.mixDiffCoeffs() # mass diffusion coefficients
    thmlDiff = g.thermalDiffCoeffs() # thermal diffusion coefficients
    ratio = abs(dT*thmlDiff/massDiff/T0/rho)


    f = file(outdir+fn[i]+ext2, 'w') # open for 'w'riting
    f.write(fn[i]+' composition (mol/m3):\n')
    f.write(X[i]+'\n\n')
    f.write('Mass diffusion coefficients:\n')
    for j in range(len(ratio)):
        line = nm[j]+ ',' + `massDiff[j]` + '\n'
        f.write(line)
    f.write('Thermal diffusion coefficients:\n')
    for j in range(len(ratio)):
        line = nm[j]+ ',' + `thmlDiff[j]` + '\n'
        f.write(line)
    f.write('Ratio dT*DkT/T/Dkm/rho:\n')
```

```
for j in range(len(ratio)):
    line = nm[j]+ ',' + `ratio[j]` + '\n'
    f.write(line)
f.close()
```

Appendix C
Equation Discretization of the Channel Flow Model

Governing equations (2.26) through (2.30) can be discretized using the SIMPLEC [69] algorithm on the staggered grid in Fig. 2-3. A second-order finite-difference technique is employed to discretize the partial difference terms.

The continuity equation (2.26) is first discretized

$$\frac{\rho_{i,j}^{n+1}-\rho_{i,j}^{n}}{\Delta t}+\frac{\rho_{i+1/2,j}u_{i+1,j}-\rho_{i-1/2,j}u_{i,j}}{\Delta x_i}+\frac{\rho_{i,j+1/2}v_{i,j+1}-\rho_{i,j-1/2}v_{i,j}}{\Delta y_j}=0 \tag{C.1}$$

and this yields

$$\begin{aligned}&\frac{\Delta x_i\Delta y_j}{\Delta t}\left(\rho_{i,j}^{n+1}-\rho_{i,j}^{n}\right)+\Delta y_j\left(\rho_{i+1/2,j}u_{i+1,j}-\rho_{i-1/2,j}u_{i,j}\right)\\&\quad+\Delta x_i\left(\rho_{i,j+1/2}v_{i,j+1}-\rho_{i,j-1/2}v_{i,j}\right)=0\end{aligned} \tag{C.2}$$

Similarly, the discretized x-momentum equation is

$$\begin{aligned}&a_{i,j}^{u}u_{i,j}^{n+1}+\left(a_{i+1,j}^{u}u_{i+1,j}^{n+1}+a_{i-1,j}^{u}u_{i-1,j}^{n+1}+a_{i,j+1}^{u}u_{i,j+1}^{n+1}+a_{i,j-1}^{u}u_{i,j-1}^{n+1}\right)\\&=-\Delta y_j\left(p_{i,j}^{n+1}-p_{i-1,j}^{n+1}\right)+b_{i,j}^{u}\end{aligned} \tag{C.3}$$

where

$$\begin{aligned}a_{i,j}^{u}=&\frac{\Delta\overline{x}_i\Delta y_j}{\Delta t}\rho_{i-1/2,j}^{*}+\frac{\Delta y_j}{4}\left[\left(\rho_{i,j}^{*}-\rho_{i-1,j}^{*}\right)u_{i,j}^{*}+2\left(\rho_{i,j}^{*}u_{i+1,j}^{*}-\rho_{i-1,j}^{*}u_{i-1,j}^{*}\right)\right]\\&+\Delta\overline{x}_i\left(\frac{\rho_{i-1/2,j+1/2}v_{i-1/2,j+1}\Delta y_{j+1}}{\Delta y_j+\Delta y_{j+1}}-\frac{\rho_{i-1/2,j-1/2}v_{i-1/2,j}\Delta y_{j-1}}{\Delta y_j+\Delta y_{j-1}}\right)\\&+\frac{4\Delta y_j}{3}\left(\frac{\mathrm{Re}_{i,j}^{-1}}{\Delta x_i}+\frac{\mathrm{Re}_{i-1,j}^{-1}}{\Delta x_{i-1}}\right)+\Delta\overline{x}_i\left(\frac{\mathrm{Re}_{i-1/2,j+1/2}^{-1}}{\Delta\overline{y}_{j+1}}+\frac{\mathrm{Re}_{i-1/2,j-1/2}^{-1}}{\Delta\overline{y}_j}\right)\end{aligned},$$

$$a_{i+1,j}^{u}=\Delta y_j\left(\frac{\rho_{i,j}^{*}u_{i+1,j}^{*}}{4}-\frac{4}{3\,\mathrm{Re}_{i,j}\,\Delta x_i}\right),\ a_{i-1,j}^{u}=-\Delta y_j\left(\frac{\rho_{i-1,j}^{*}u_{i-1,j}^{*}}{4}+\frac{4}{3\,\mathrm{Re}_{i-1,j}\,\Delta x_{i-1}}\right),$$

$$a_{i,j+1}^{u}=\frac{1}{2}\frac{\Delta x_i+\Delta x_{i-1}}{\Delta y_j+\Delta y_{j+1}}\left(\Delta y_j\rho_{i-1/2,j+1/2}v_{i-1/2,j+1}-\frac{2}{\mathrm{Re}_{i-1/2,j+1/2}}\right),$$

$$a_{i,j-1}^{u}=-\frac{1}{2}\frac{\Delta x_i+\Delta x_{i-1}}{\Delta y_j+\Delta y_{j-1}}\left(\Delta y_j\rho_{i-1/2,j-1/2}v_{i-1/2,j}+\frac{2}{\mathrm{Re}_{i-1/2,j-1/2}}\right),$$

$$b_{i,j}^{u} = \frac{\Delta y_j}{2\Delta t}\left(\rho_{i,j}^{n}\Delta x_{i-1} + \rho_{i-1,j}^{n}\Delta x_i\right)u_{i,j}^{n} + \left(\frac{v_{i,j+1}^{n} - v_{i-1,j+1}^{n}}{\mathrm{Re}_{i-1/2,j+1/2}} - \frac{v_{i,j}^{n} - v_{i-1,j}^{n}}{\mathrm{Re}_{i-1/2,j-1/2}}\right) - \frac{2}{3}\left(\frac{v_{i,j+1}^{n} - v_{i,j}^{n}}{\mathrm{Re}_{i,j}} - \frac{v_{i-1,j+1}^{n} - v_{i-1,j}^{n}}{\mathrm{Re}_{i-1,j}}\right),$$

and the y-momentum equation is

$$\begin{aligned} &a_{i,j}^{v}v_{i,j}^{n+1} + a_{i+1,j}^{v}v_{i+1,j}^{n+1} + a_{i,j-1}^{v}v_{i,j-1}^{n+1} + a_{i,j+1}^{v}v_{i,j+1}^{n+1} + a_{i-1,j}^{v}v_{i-1,j}^{n+1} \\ &= -\Delta x_i\left(p_{i,j} - p_{i,j-1}\right) + b_{i,j}^{v} \end{aligned} \tag{C.4}$$

where

$$\begin{aligned} a_{i,j}^{v} &= \frac{\Delta x_i \Delta\overline{y}_j}{\Delta t}\rho_{i,j-1/2}^{*} + \Delta\overline{y}_j\left(\frac{\rho_{i+1/2,j-1/2}^{*}u_{i+1,j-1/2}^{*}\Delta x_{i+1}}{\Delta x_i + \Delta x_{i+1}} - \frac{\rho_{i-1/2,j-1/2}^{*}u_{i,j-1/2}^{*}\Delta x_{i-1}}{\Delta x_i + \Delta x_{i-1}}\right) \\ &\quad + \frac{\Delta x_i}{4}\left[\left(\rho_{i,j}^{*} - \rho_{i,j-1}^{*}\right)v_{i,j}^{*} + 2\left(\rho_{i,j}^{*}v_{i,j+1}^{*} - \rho_{i,j-1}^{*}v_{i,j-1}^{*}\right)\right] \\ &\quad + \Delta\overline{y}_j\left(\frac{\mathrm{Re}_{i+1/2,j-1/2}^{-1}}{\Delta\overline{x}_{i+1}} + \frac{\mathrm{Re}_{i-1/2,j-1/2}^{-1}}{\Delta\overline{x}_i}\right) + \frac{4\Delta x_i}{3}\left(\frac{\mathrm{Re}_{i,j}^{-1}}{\Delta y_j} + \frac{\mathrm{Re}_{i,j-1}^{-1}}{\Delta y_{j-1}}\right) \end{aligned},$$

$$a_{i+1,j}^{v} = \frac{1}{2}\frac{\Delta y_j + \Delta y_{j-1}}{\Delta x_i + \Delta x_{i+1}}\left(\Delta x_i\rho_{i+1/2,j-1/2}^{*}u_{i+1,j-1/2}^{*} - \frac{2}{\mathrm{Re}_{i+1/2,j-1/2}}\right),$$

$$a_{i-1,j}^{v} = -\frac{1}{2}\frac{\Delta y_j + \Delta y_{j-1}}{\Delta x_i + \Delta x_{i-1}}\left(\Delta x_i\rho_{i-1/2,j-1/2}^{*}u_{i,j-1/2}^{*} + \frac{2}{\mathrm{Re}_{i-1/2,j-1/2}}\right),$$

$$a_{i,j+1}^{v} = \Delta x_i\left(\frac{\rho_{i,j}^{*}v_{i,j+1}^{*}}{4} - \frac{4}{3\,\mathrm{Re}_{i,j}^{*}\,\Delta y_j}\right),\ a_{i,j-1}^{v} = -\Delta x_i\left(\frac{\rho_{i,j-1}^{*}v_{i,j-1}^{*}}{4} + \frac{4}{3\,\mathrm{Re}_{i,j-1}^{*}\,\Delta y_{j-1}}\right),$$

$$b_{i,j}^{v} = \frac{\Delta x_i \Delta\overline{y}_j}{\Delta t}\rho_{i,j-1/2}^{n}v_{i,j}^{n} + \left(\frac{u_{i+1,j}^{n} - u_{i+1,j-1}^{n}}{\mathrm{Re}_{i+1/2,j-1/2}^{n}} - \frac{u_{i,j}^{n} - u_{i,j-1}^{n}}{\mathrm{Re}_{i-1/2,j-1/2}^{n}}\right) - \frac{2}{3}\left(\frac{u_{i+1,j}^{n} - u_{i,j}^{n}}{\mathrm{Re}_{i,j}^{n}} - \frac{u_{i+1,j-1}^{n} - u_{i,j-1}^{n}}{\mathrm{Re}_{i,j-1}^{n}}\right)$$

where variables with a superscript "*" are the intermediate solutions, and the Reynolds number is calculated with the local dynamic viscosity calculated by Cantera[68]. The distances between the centers of two adjacent control volumes in the x and y directions are respectively defined as

$$\Delta\overline{x}_i = 0.5(\Delta x_i + \Delta x_{i-1}),\ \Delta\overline{y}_j = 0.5\left(\Delta y_j + \Delta y_{j-1}\right). \tag{C.5}$$

The pressure-correction equation for indirectly calculating the pressure variation in the flow field on the new time level is obtained by substituting the momentum

equations (C.3) and (C.4) into the continuity equation (C.1) [69], in which the pressure variation and the velocity components are all assumed to consist of an intermediate value (marked by "*") and a correction value (marked by "'")

$$p = p^* + p' \,,\; u = u^* + u' \,,\; v = v^* + v' \,. \tag{C.6}$$

The discretized pressure-correction equation has the same general form as the momentum equations, and is given by

$$a^p_{i,j} p'_{i,j} + a^p_{i+1,j} p'_{i+1,j} + a^p_{i-1,j} p'_{i-1,j} + a^p_{i,j+1} p'_{i,j+1} + a^p_{i,j-1} p'_{i,j-1} = b^p_{i,j} \tag{C.7}$$

where

$$a^p_{i+1,j} = \rho^*_{i+1/2,j} \Delta y_j c^u_{i+1,j} \,,\; a^p_{i-1,j} = \rho^*_{i-1/2,j} \Delta y_j c^u_{i,j} \,,$$

$$a^p_{i,j+1} = \rho^*_{i,j+1/2} \Delta x_i c^v_{i,j+1} \,,\; a^p_{i,j-1} = \rho_{i,j-1/2} \Delta x_i c^v_{i,j} \,,$$

$$a^p_{i,j} = -\left(a^p_{i+1,j} + a^p_{i-1,j} + a^p_{i,j+1} + a^p_{i,j-1} \right),$$

$$b^p_{i,j} = -\frac{\Delta x_i \Delta y_j}{\Delta t}\left(\rho^*_{i,j} - \rho^n_{i,j} \right) - \Delta y_j \left(\rho^*_{i+1/2,j} u^*_{i+1,j} - \rho^*_{i-1/2,j} u^*_{i,j} \right) - \Delta x_i \left(\rho^*_{i,j+1/2} v^*_{i,j+1} - \rho^*_{i,j-1/2} v^*_{i,j} \right) .$$

In the same way as the momentum equations, the energy equation is discretized into

$$a^t_{i,j} T^{n+1}_{i,j} + a^t_{i+1,j} T^{n+1}_{i+1,j} + a^t_{i-1,j} T^{n+1}_{i-1,j} + a^t_{i,j+1} T^{n+1}_{i,j+1} + a^t_{i,j-1} T^{n+1}_{i,j-1} = b^t_{i,j} \tag{C.8}$$

where

$$\begin{aligned} a^t_{i,j} = {} & \frac{\Delta x_i \Delta y_j}{\Delta t} \rho_{i,j} + \Delta y_j \left(\frac{\rho_{i+1/2,j} u_{i+1,j} \Delta x_{i+1}}{\Delta x_i + \Delta x_{i+1}} - \frac{\rho_{i-1/2,j} u_{i,j} \Delta x_{i-1}}{\Delta x_i + \Delta x_{i-1}} \right) \\ & + \Delta x_i \left(\frac{\rho_{i,j+1/2} v_{i,j+1} \Delta y_{j+1}}{\Delta y_j + \Delta y_{j+1}} - \frac{\rho_{i,j-1/2} v_{i,j} \Delta y_{j-1}}{\Delta y_j + \Delta y_{j-1}} \right) \\ & + \frac{2}{\mathrm{Re}_0 \, \mathrm{Pr}_0 \left(c_p \right)_{i,j}} \left[\Delta y_j \left(\frac{\lambda_{i+1/2,j}}{\Delta x_i + \Delta x_{i+1}} + \frac{\lambda_{i-1/2,j}}{\Delta x_i + \Delta x_{i-1}} \right) + \Delta x_i \left(\frac{\lambda_{i,j+1/2}}{\Delta y_j + \Delta y_{j+1}} + \frac{\lambda_{i,j-1/2}}{\Delta y_j + \Delta y_{j-1}} \right) \right] \\ & - \frac{\rho_{i,j} \Delta x_i \Delta y_j}{2 \mathrm{Re}_0 \, \mathrm{Sc}_0 \left(c_p \right)_{i,j}} \left[\frac{Sx_{i,j}}{\Delta x_i} \left(\frac{\Delta x_{i+1}}{\Delta \overline{x}_{i+1}} - \frac{\Delta x_{i-1}}{\Delta \overline{x}_i} \right) + \frac{Sy_{i,j}}{\Delta y_j} \left(\frac{\Delta y_{j+1}}{\Delta \overline{y}_{j+1}} - \frac{\Delta y_{j-1}}{\Delta \overline{y}_j} \right) \right] \end{aligned}$$

$$a^t_{i+1,j} = \frac{\Delta x_i \Delta y_j}{2 \Delta \overline{x}_{i+1}} \rho_{i+1/2,j} u_{i+1,j} - \frac{\lambda_{i+1/2,j} \Delta y_j}{\mathrm{Re}_0 \, \mathrm{Pr}_0 \left(c_p \right)_{i,j} \Delta \overline{x}_{i+1}} - \frac{\rho_{i,j} \Delta x_i \Delta y_j Sx_{i,j}}{2 \mathrm{Re}_0 \, \mathrm{Sc}_0 \left(c_p \right)_{i,j} \Delta \overline{x}_{i+1}} \,,$$

$$a^t_{i-1,j} = -\frac{\Delta x_i \Delta y_j}{2 \Delta \overline{x}_i} \rho_{i-1/2,j} u_{i,j} - \frac{\lambda_{i-1/2,j} \Delta y_j}{\mathrm{Re}_0 \, \mathrm{Pr}_0 \left(c_p \right)_{i,j} \Delta \overline{x}_i} + \frac{\rho_{i,j} \Delta x_i \Delta y_j Sx_{i,j}}{2 \mathrm{Re}_0 \, \mathrm{Sc}_0 \left(c_p \right)_{i,j} \Delta \overline{x}_i} \,,$$

$$a^t_{i,j+1} = \frac{\Delta x_i \Delta y_j}{2\Delta \overline{y}_{j+1}} \rho_{i,j+1/2} v_{i,j+1} - \frac{\lambda_{i,j+1/2} \Delta x_i}{\mathrm{Re}_0 \, \mathrm{Pr}_0 \left(c_p \right)_{i,j} \Delta \overline{y}_{j+1}} - \frac{\rho_{i,j} \Delta x_i \Delta y_j Sy_{i,j}}{2 \, \mathrm{Re}_0 \, \mathrm{Sc}_0 \left(c_p \right)_{i,j} \Delta \overline{y}_{j+1}},$$

$$a^t_{i,j-1} = -\frac{\Delta x_i \Delta y_j}{2\Delta \overline{y}_j} \rho_{i,j-1/2} v_{i,j} - \frac{\lambda_{i,j-1/2} \Delta x_i}{\mathrm{Re}_0 \, \mathrm{Pr}_0 \left(c_p \right)_{i,j} \Delta \overline{y}_j} + \frac{\rho_{i,j} \Delta x_i \Delta y_j Sy_{i,j}}{2 \, \mathrm{Re}_0 \, \mathrm{Sc}_0 \left(c_p \right)_{i,j} \Delta \overline{y}_j},$$

$$b^t_{i,j} = \frac{\Delta x_i \Delta y_j}{\Delta t} \rho^n_{i,j} T^n_{i,j}, \; Sx_{i,j} = \sum_{k=1}^{K} c_{pk} D_{km} \left(Y_k \right)_x, \; Sy_{i,j} = \sum_{k=1}^{K} c_{pk} D_{km} \left(Y_k \right)_y .$$

and the discretized species mass-conservation equation is

$$a^Y_{i,j} Y^{n+1}_{i,j} + a^Y_{i+1,j} Y^{n+1}_{i+1,j} + a^Y_{i-1,j} Y^{n+1}_{i-1,j} + a^Y_{i,j+1} Y^{n+1}_{i,j+1} + a^Y_{i,j-1} Y^{n+1}_{i,j-1} = b^Y_{i,j} \tag{C.9}$$

where

$$\begin{aligned} a^Y_{i,j} = {} & \frac{\Delta x_i \Delta y_j}{\Delta t} \rho_{i,j} + \frac{1}{2} \Delta y_j \left(\rho_{i+1/2,j} u_{i+1,j} \frac{\Delta x_{i+1}}{\Delta \overline{x}_{i+1}} - \rho_{i-1/2,j} u_{i,j} \frac{\Delta x_{i-1}}{\Delta \overline{x}_i} \right) \\ & + \frac{1}{2} \Delta x_i \left(\rho_{i,j+1/2} v_{i,j+1} \frac{\Delta y_{j+1}}{\Delta \overline{y}_{j+1}} - \rho_{i,j-1/2} v_{i,j} \frac{\Delta y_{j-1}}{\Delta \overline{y}_j} \right) \\ & + \Delta y_j \left(\frac{\left(\rho D_{km} \right)_{i+1/2,j}}{\mathrm{Re}_0 \, \mathrm{Sc}_0 \, \Delta \overline{x}_{i+1}} + \frac{\left(\rho D_{km} \right)_{i-1/2,j}}{\mathrm{Re}_0 \, \mathrm{Sc}_0 \, \Delta \overline{x}_i} \right) + \Delta x_i \left(\frac{\left(\rho D_{km} \right)_{i,j+1/2}}{\mathrm{Re}_0 \, \mathrm{Sc}_0 \, \Delta \overline{y}_{j+1}} + \frac{\left(\rho D_{km} \right)_{i,j-1/2}}{\mathrm{Re}_0 \, \mathrm{Sc}_0 \, \Delta \overline{y}_j} \right) \end{aligned},$$

$$a^Y_{i+1,j} = \frac{\Delta x_i \Delta y_j}{2\Delta \overline{x}_{i+1}} \rho_{i+1/2,j} u_{i+1,j} - \frac{\left(\rho D_{km} \right)_{i+1/2,j} \Delta y_j}{\mathrm{Re}_0 \, \mathrm{Sc}_0 \, \Delta \overline{x}_{i+1}},$$

$$a^Y_{i-1,j} = -\frac{\Delta x_i \Delta y_j}{2\Delta \overline{x}_i} \rho_{i-1/2,j} u_{i,j} - \frac{\left(\rho D_{km} \right)_{i-1/2,j} \Delta y_j}{\mathrm{Re}_0 \, \mathrm{Sc}_0 \, \Delta \overline{x}_i},$$

$$a^Y_{i,j+1} = \frac{\Delta x_i \Delta y_j}{2\Delta \overline{y}_{j+1}} \rho_{i,j+1/2} v_{i,j+1} - \frac{\left(\rho D_{km} \right)_{i,j+1/2} \Delta x_i}{\mathrm{Re}_0 \, \mathrm{Sc}_0 \, \Delta \overline{y}_{j+1}},$$

$$a^Y_{i,j-1} = -\frac{\Delta x_i \Delta y_j}{2\Delta \overline{y}_j} \rho_{i,j-1/2} v_{i,j} - \frac{\left(\rho D_{km} \right)_{i,j-1/2} \Delta x_i}{\mathrm{Re}_0 \, \mathrm{Sc}_0 \, \Delta \overline{y}_j},$$

$$b^Y_{i,j} = \frac{\Delta x_i \Delta y_j}{\Delta t} \rho^n_{i,j} Y^n_{i,j} .$$

Bibliography

1. J. B. Young, *Thermofluid modeling of fuel cells*, Annual Review of Fluid Mechanics, **39**, 193 (2007).
2. S. C. Singhal, *Science and Technology of solid-oxide fuel cells*, Mrs Bulletin, **25**, 16 (2000).
3. R. J. Kee, H. Y. Zhu, and D. G. Goodwin, *Solid-oxide fuel cells with hydrocarbon fuels,* Proceedings of the Combustion Institute, **30**, 2379 (2005).
4. A. Weber, B. Sauer, A. C. Muller, D. Herbstritt, and E. Ivers-Tiffee, *Oxidation of H-2, CO and methane in SOFCs with Ni/YSZ-cermet anodes,* Solid State Ionics, **152**, 543 (2002).
5. S. C. Singhal, *Advances in solid oxide fuel cell technology*, Solid State Ionics, **135**, 305 (2000).
6. Y. Hao and D. G. Goodwin, *Numerical modeling of single-chamber SOFCs with hydrocarbon fuels,* Journal of the Electrochemical Society, **154**, B207 (2007).
7. I. Riess, P. J. Vanderput, and J. Schoonman, *Solid oxide fuel-cells operating on uniform mixtures of fuel and air,* Solid State Ionics, **82**, 1 (1995).
8. T. Suzuki, P. Jasinski, V. Petrovsky, H. U. Anderson, and F. Dogan, *Performance of a porous electrolyte in single-chamber SOFCs,* Journal of the Electrochemical Society, **152**, A527 (2005).
9. M. Yano, A. Tomita, M. Sano, and T. Hibino, *Recent advances in single-chamber solid oxide fuel cells: A review,* Solid State Ionics, **177**, 3351 (2007).

10. Y. Hao, Z. P. Shao, J. Mederos, W. Lai, D. G. Goodwin, and S. M. Haile, *Recent advances in single-chamber fuel-cells: Experiment and modeling,* Solid State Ionics, **177**, 2013 (2006).
11. T. Hibino, S. Q. Wang, S. Kakimoto, and M. Sano, *One-chamber solid oxide fuel cell constructed from a YSZ electrolyte with a Ni anode and LSM cathode,* Solid State Ionics, **127**, 89 (2000).
12. T. Hibino, S. Q. Wang, S. Kakimoto, and M. Sano, *Single chamber solid oxide fuel cell constructed from an yttria-stabilized zirconia electrolyte,* Electrochemical and Solid State Letters, **2**, 317 (1999).
13. T. Hibino and H. Iwahara, *Simplification of solid oxide fuel-cell system using partial oxidation of methane,* Chemistry Letters, 1131 (1993).
14. T. Hibino, H. Tsunekawa, S. Tanimoto, and M. Sano, *Improvement of a single-chamber solid-oxide fuel cell and evaluation of new cell designs,* Journal of the Electrochemical Society, **147**, 1338 (2000).
15. T. Hibino, K. Ushiki, and Y. Kuwahara, *New concept for simplifying SOFC system,* Solid State Ionics, **91**, 69 (1996).
16. T. Hibino, Y. Kuwahara, and S. Wang, *Effect of electrode and electrolyte modification on the performance of one-chamber solid oxide fuel cell,* Journal of the Electrochemical Society, **146**, 2821 (1999).
17. T. Hibino, A. Hashimoto, T. Inoue, J. Tokuno, S. Yoshida, and M. Sano, *A low-operating-temperature solid oxide fuel cell in hydrocarbon-air mixtures,* Science, **288**, 2031 (2000).

18. T. Hibino, A. Hashimoto, M. Yano, M. Suzuki, S. Yoshida, and M. Sano, *High performance anodes for SOFCs operating in methane-air mixture at reduced temperatures,* Journal of the Electrochemical Society, **149**, A133 (2002).

19. T. Hibino, A. Hashimoto, T. Inoue, J. Tokuno, S. Yoshida, and M. Sano, *A solid oxide fuel cell using an exothermic reaction as the heat source,* Journal of the Electrochemical Society, **148**, A544 (2001).

20. Z. P. Shao and S. M. Haile, *A high-performance cathode for the next generation of solid-oxide fuel cells,* Nature, **431**, 170 (2004).

21. Z. P. Shao, C. Kwak, and S. M. Haile, *Anode-supported thin-film fuel cells operated in a single chamber configuration 2T-I-12,* Solid State Ionics, **175**, 39 (2004).

22. Z. P. Shao, J. Mederos, W. C. Chueh and S. M. Haile, *High power-density single-chamber fuel cells operated on methane*, Journal of Power Sources, **162**, 589 (2006).

23. I. C. Stefan, C. P. Jacobson, S. J. Visco, and L. C. De Jonghe, *Single chamber fuel cells: Flow geometry, rate, and composition considerations,* Electrochemical and Solid State Letters, **7**, A198 (2004).

24. T. Suzuki, P. Jasinski, V. Petrovsky, H. U. Anderson, and F. Dogan, *Anode supported single chamber solid oxide fuel cell in CH4-air mixture,* Journal of the Electrochemical Society, **151**, A1473 (2004).

25. T. Suzuki, P. Jasinski, H. U. Anderson, and F. Dogan, *Role of composite cathodes in single chamber SOFC,* Journal of the Electrochemical Society, **151**, A1678 (2004).

26. T. Suzuki, P. Jasinski, H. U. Anderson, and F. Dogan, *Single chamber electrolyte supported SOFC module,* Electrochemical and Solid State Letters, **7**, A391 (2004).

27. T. W. Napporn, X. Jacques-Bedard, F. Morin, and M. Meunier, *Operating conditions of a single-chamber SOFC,* Journal of the Electrochemical Society, **151**, A2088 (2004).

28. T. W. Napporn, F. Morin, and M. Meunier, *Evaluation of the actual working temperature of a single-chamber SOFC,* Electrochemical and Solid State Letters, **7**, A60 (2004).

29. H. Y. Zhu and R. J. Kee, Journal of Power Sources, *Thermodynamics of SOFC efficiency and fuel utilization as functions of fuel mixtures and operating conditions,* **161**, 957 (2006).

30. C. Stiller, B. Thorud, S. Seljebo, O. Mathisen, H. Karoliussen, and O. Bolland, *Finite-volume modeling and hybrid-cycle performance of planar and tubular solid oxide fuel cells,* Journal of Power Sources, **141**, 227 (2005).

31. P. W. Li and K. Suzuki, *Numerical modeling and performance study of a tubular SOFC,* Journal of the Electrochemical Society, **151**, A548 (2004).

32. A. M. Svensson and K. Nisancioglu, *Current distribution at porous electrode-solid oxide electrolyte interface,* Journal of the Electrochemical Society, **145**, 3130 (1998).

33. E. Achenbach, *3-Dimensional and time-dependent simulation of a planar solid oxide fuel-cell stack,* Journal of Power Sources, **49**, 333 (1994).

34. W. G. Bessler, *A new computational approach for SOFC impedance from detailed electrochemical reaction-diffusion models,* Solid State Ionics, **176**, 997 (2005).

35. S. Campanari and P. Iora, *Definition and sensitivity analysis of a finite volume SOFC model for a tubular cell geometry,* Journal of Power Sources, **132**, 113 (2004).

36. J. L. Yuan and B. Sunden, *Analysis of intermediate temperature solid oxide fuel cell transport processes and performances,* Journal of Heat Transfer-Transactions of the ASME, **127**, 1380 (2005).

37. H. Y. Zhu and R. J. Kee, *A general mathematical model for analyzing the performance of fuel-cell membrane-electrode assemblies,* Journal of Power Sources, **117**, 61 (2003).

38. J. H. Nam and D. H. Jeon, *A comprehensive micro-scale model for transport and reaction in intermediate temperature solid oxide fuel cells,* Electrochimica Acta, **51**, 3446 (2006).

39. M. M. Hussain, X. Li, and I. Dincer, *Mathematical modeling of planar solid oxide fuel cells,* Journal of Power Sources, **161**, 1012 (2006).

40. E. S. Putna, J. Stubenrauch, J. M. Vohs, and R. J. Gorte, *Ceria-based anodes for the direct oxidation of methane in solid oxide fuel cells,* Langmuir, **11**, 4832 (1995).

41. M. Gödickemeier, K. Sasaki, L. J. Gauckler, and I. Riess, *Electrochemical characteristics of cathodes in solid oxide fuel cells based on ceria electrolytes,* Journal of the Electrochemical Society, **144**, 1635 (1997).

42. K. P. Recknagle, R. E. Williford, L. A. Chick, D. R. Rector, and M. A. Khaleel, *Three-dimensional thermo-fluid electrochemical modeling of planar SOFC stacks,* Journal of Power Sources, **113**, 109 (2003).

43. N. F. Bessette, W. J. Wepfer, and J. Winnick, *A mathematical-model of a solid oxide fuel-cell,* Journal of the Electrochemical Society, **142**, 3792 (1995).

44. Z. T. Xia, S. H. Chan, and K. A. Khor, *An improved anode micro model of SOFC,* Electrochemical and Solid State Letters, **7**, A63 (2004).

45. R. Bove and S. Ubertini, *Modeling solid oxide fuel cell operation: Approaches, techniques and results,* Journal of Power Sources, **159**, 543 (2006).

46. B. A. Haberman and J. B. Young, *Three-dimensional simulation of chemically reacting gas flows in the porous support structure of an integrated-planar solid oxide fuel cell,* International Journal of Heat and Mass Transfer, **47**, 3617 (2004).

47. Y. T. Qi, B. Huang, and J. L. Luo, *Dynamic modeling of a finite volume of solid oxide fuel cell: The effect of transport dynamics,* Chemical Engineering Science, **61**, 6057 (2006).

48. P. Aguiar, C. S. Adjiman, and N. P. Brandon, *Anode-supported intermediate temperature direct internal reforming solid oxide fuel cell. I: model-based steady-state performance,* Journal of Power Sources, **138**, 120 (2004).

49. P. Mandin, C. Bernay, S. Tran-Dac, A. Broto, D. Abes, and M. Cassir, *SOFC modeling and numerical simulation of performances,* Fuel Cells, **6**, 71 (2006).

50. V. M. Janardhanan and O. Deutschmann, *CFD analysis of a solid oxide fuel cell with internal reforming: Coupled interactions of transport, heterogeneous catalysis and electrochemical processes,* Journal of Power Sources, **162**, 1192 (2006).

51. C. Y. Chung, Y. C. Chung, J. Kim, J. Lee, and H. W. Lee, *Numerical modeling of micro single-chamber ceria-based SOFC,* Journal of Electroceramics, **17**, 959 (2006).

52. H. Yakabe, T. Ogiwara, M. Hishinuma, and I. Yasuda, *3-D model calculation for planar SOFC,* Journal of Power Sources, **102**, 144 (2001).

53. L. Ma, D. B. Ingham, M. Pourkashanian, and E. Carcadea, *Review of the computational fluid dynamics modeling of fuel cells,* Journal of Fuel Cell Science and Technology, **2**, 246 (2005).

54. K. M. Walters, A. M. Dean, H. Y. Zhu, and R. J. Kee, *Homogeneous kinetics and equilibrium predictions of coking propensity in the anode channels of direct oxidation solid-oxide fuel cells using dry natural gas,* Journal of Power Sources, **123**, 182 (2003).

55. J. W. Kim, A. V. Virkar, K. Z. Fung, K. Mehta, and S. C. Singhal, *Polarization effects in intermediate temperature, anode-supported solid oxide fuel cells,* Journal of the Electrochemical Society, **146**, 69 (1999).

56. H. Y. Zhu, R. J. Kee, V. M. Janardhanan, O. Deutschmann, and D. G. Goodwin, *Modeling elementary heterogeneous chemistry and electrochemistry in solid-oxide fuel cells,* Journal of the Electrochemical Society, **152**, A2427 (2005).

57. E. A. Mason and A. P. Malinauskas, *Gas Transport in Porous Media: the Dusty-Gas Model,* American Elsevier, New York (1983).

58. D. Arnost and P. Schneider, *Dynamic transport of multicomponent mixtures of gases in porous solids,* Chemical Engineering Journal and the Biochemical Engineering Journal, **57**, 91 (1995).

59. P. W. Li and M. K. Chyu, *Simulation of the chemical/electrochemical reactions and heat/mass transfer for a tubular SOFC in a stack*, Journal of Power Sources, **124**, 487 (2003).

60. O. Deutschmann and L. D. Schmidt, *Modeling the partial oxidation of methane in a short-contact-time reactor*, AIChE J., **44**, 2465 (1998).

61. E. S. Hecht, G. K. Gupta, H. Y. Zhu, A. M. Dean, R. J. Kee, L. Maier and O. Deutschmann, *Methane reforming kinetics within a Ni–YSZ SOFC anode support*, Applied Catalysis a-General, **295**, 40 (2005).

62. C. Y. Chung and Y. C. Chung, *Performance characteristics of micro single-chamber solid oxide fuel cell: Computational analysis,* Journal of Power Sources, **154**, 35 (2006).

63. S. J. Ahn, Y. B. Kim, J. Moon, J. H. Lee, and J. Kim, *Co-planar type single chamber solid oxide fuel cell with micro-patterned electrodes,* Journal of Electroceramics, **17**, 689 (2006).

64. S. J. Ahn, J. H. Lee, J. Kim, and J. Moon, *Single-chamber solid oxide fuel cell with micropatterned interdigitated electrodes,* Electrochemical and Solid State Letters, **9**, A228 (2006).

65. G. K. Gupta, E. S. Hecht, H. Y. Zhu, A. M. Dean, and R. J. Kee, *Gas-phase reactions of methane and natural-gas with air and steam in non-catalytic regions of a solid-oxide fuel cell,* Journal of Power Sources, **156**, 434 (2006).

66. R. J. Kee, M. E. Coltrin, and P. Glarborg, *Chemically Reacting Flow: Theory and Practice,* John Wiley & Sons, Inc., Hoboken (2003).

67. H. N. Najm, P. S. Wyckoff, and O. M. Knio, *A semi-implicit numerical scheme for reacting flow I. Stiff chemistry,* Journal of Computational Physics, **143**, 381 (1998).

68. D. G. Goodwin, *Chemical Vapor Deposition XVI and EUROCVD 14*, Electrochemical Society, p. 155 (2003).

69. S. V. Patankar, *Numerical Heat Transfer and Fluid Flow,* Hemisphere Publishing Corporation (1980).

70. V. A. O. Anjorin and I. E. Barton, *Removal of temporal and under-relaxation terms from the pressure-correction equation of the SIMPLE algorithm*, International Journal of Fluid Dynamics, **5**, 59 (2001).

71. T. Thampan, S. Malhotra, H. Tang, and R. Datta, *Modeling of conductive transport in proton-exchange membranes for fuel cells*, Journal of the Electrochemical Society, **147**, 3242 (2000).

72. *CRC Handbook of Solid State Electrochemistry*, CRC Press, Boca Raton (1997).

73. I. Riess, *Mixed ionic-electronic conductors—material properties and applications*, Solid State Ionics, **157**, 1 (2003).

74. T. Hibino, A. Hashimoto, T. Inoue, J. Tokuno, S. Yoshida, and M. Sano, *Single-chamber solid oxide fuel cells at intermediate temperatures with various hydrocarbon-air mixtures,* Journal of the Electrochemical Society, **147**, 2888 (2000).

75. I. Riess, *Current voltage relation and charge-distribution in mixed ionic electronic solid conductors*, Journal of Physics and Chemistry of Solids, **47**, 129 (1986).

76. I. Riess, M. Gödickemeier, and L. J. Gauckler, *Characterization of solid oxide fuel cells based on solid electrolytes or mixed ionic electronic conductors*, Solid State Ionics, **90**, 91 (1996).

77. M. Gödickemeier and L. J. Gauckler, *Engineering of solid oxide fuel cells with ceria-based electrolytes*, Journal of the Electrochemical Society, **145**, 414 (1998).

78. W. Lai and S. M. Haile, *Impedance spectroscopy as a tool for chemical and electrochemical analysis of mixed conductors: A case study of ceria,* Journal of the American Ceramic Society, **88**, 2979 (2005).

79. Z. P. Shao, private communication.

80. A. J. Bard and L. R. Faulkner, *Electrochemical Methods: Fundamentals and Applications,* John Wiley & Sons, Inc., New York (2000).

81. Z. P. Shao, S. M. Haile, J. Ahn, P. D. Ronney, Z. L. Zhan, and S. A. Barnett, *A thermally self-sustained micro solid-oxide fuel-cell stack with high power density,* Nature, **435**, 795 (2005).

82. Y. Matsuzaki and I. Yasuda, *Relationship between the steady-state polarization of the SOFC air electrode, La0.6Sr0.4MnO3+delta/YSZ, and its complex impedance measured at the equilibrium potential,* Solid State Ionics, **126**, 307 (1999).

83. Z. L. Zhan and S. A. Barnett, *An octane-fueled solid oxide fuel cell,* Science, **308**, 844 (2005).

84. S. M. Haile, D. A. Boysen, C. R. I. Chisholm, and R. B. Merle, *Solid acids as fuel cell electrolytes,* Nature, **410**, 910 (2001).

85. S. M. Haile, C. R. I. Chisholm, K. Sasaki, D. A. Boysen, and T. Uda, *Solid acid proton conductors: from laboratory curiosities to fuel cell electrolytes,* Faraday Discussions, **134**, 17 (2007).

86. A. Atkinson, S. Barnett, R. J. Gorte, J. T. S. Irvine, A. J. McEvoy, M. Mogensen, S. C. Singhal, and J. Vohs, *Advanced anodes for high-temperature fuel cells,* Nature Materials, **3**, 17 (2004).

87. W. Z. Zhu and S. C. Deevi, *A review on the status of anode materials for solid oxide fuel cells,* Materials Science and Engineering a-Structural Materials Properties Microstructure and Processing, **362**, 228 (2003).

88. T. Ishihara and Y. Takita, *Partial oxidation of methane into syngas with oxygen permeating ceramic membrane reactors,* Catalysis Surveys from Japan, **4**, 125 (2000).

89. X. Jacques-Bedard, T. W. Napporn, R. Roberge, and M. Meunier, *Performance and ageing of an anode-supported SOFC operated in single-chamber conditions,* Journal of Power Sources, **153**, 108 (2006).

90. E. P. Murray, S. J. Harris, J. Liu, and S. A. Barnett, *Direct solid oxide fuel cell operation using isooctane,* Electrochemical and Solid State Letters, **9**, A292 (2006).

91. A. M. DeGroote and G. F. Froment, *Simulation of the catalytic partial oxidation of methane to synthesis gas,* Applied Catalysis a-General, **138**, 245 (1996).

92. A. V. Virkar, J. Chen, C. W. Tanner, and J. W. Kim, *The role of electrode microstructure on activation and concentration polarizations in solid oxide fuel cells,* Solid State Ionics, **131**, 189 (2000).

93. J. M. Ahn, C. Eastwood, L. Sitzki, and P. D. Ronney, *Gas-phase and catalytic combustion in heat-recirculating burners*, Proceedings of the Combustion Institute, **30**, 2463 (2005).